UC Santa Barbara

UC Santa Barbara Electronic Theses and Dissertations

Title

Clocks, Qubits, and Searches for New Physics

Permalink

https://escholarship.org/uc/item/4kj855nz

Author

Holliman, Craig

Publication Date

2022

Peer reviewed|Thesis/dissertation

eScholarship.org Powered by the California Digital Library
University of California

UNIVERSITY OF CALIFORNIA

Santa Barbara

Clocks, Qubits, and Searches for New Physics

A dissertation submitted in partial satisfaction of the
requirements for the degree Doctor of Philosophy
in Physics

by

Craig Allen Holliman

Committee in charge:

Professor Andrew Jayich, Chair
Professor David Patterson
Professor Matthew Fisher

December 2022

The Dissertation of Craig Allen Holliman is approved.

David Patterson

Matthew Fisher

Andrew Jayich, Committee Chair

October 2022

Clocks, Qubits, and Searches for New Physics

Copyright © 2022

by

Craig Allen Holliman

To my wife, Mayuko
いつもありがとう

Acknowledgements

Thank you to my parents for the countless hours spent teaching me math, instilling in me a work ethic, and helping me become a person that could work amicably with others. Thank you to my friends for all the late night gaming sessions during the pandemic. They kept me going during hard times. Thank you to my wife for her endless support and patience. Four and a half years was a long time for such a long distance ($\sim 9,000$ km) relationship, particularly with a pandemic sandwiched in the middle. You were a huge source of motivation for me to get results in the lab. I'm excited to start our life together.

Thank you to all of the undergraduates for the support and contributions to experiments over the years. I am often stunned at the genuine passion for fundamental physics that you all possess. I was fortunate to work closely with Asad (the Sand Bandit) and Max during my early time in the lab, and later with Chaoshen and Sam. Good luck with graduate applications! You two will do great.

Thank you to the younger graduate students, Haoran, Spencer, and Sean. You all joined the group at a challenging time, but have already built two ion traps in the last year alone. I'm excited to see your future results as the traps start taking data. Don't be afraid to start getting more involved with the structural coding decisions! This will become important as the experiments get more difficult to write. Thank you to our new postdoc Roy for catching many grammatical errors in this thesis and for his undeniable skill on the basketball court.

Thank you Mingyu for all the memorable experiences and "best day evers". You've been a member of the group since the first day I joined the lab, and your extensive knowledge of atomic physics, attention to detail, and willingness to absolutely slam me in pull requests helped make me a better physicist. I'll cherish the long nights we spent searching for a radium ion signal and the excitement we felt when we finally succeeded. I'm looking forward to seeing where you end up after graduating.

To my advisor, Andrew — thank you for everything. You taught me how to best approach a problem and to always tackle the long lead-time items first. I believe that the countless hours you spent thinking about coding and organization was one of the main reasons the lab quickly achieved results. You kept me motivated throughout my Ph.D., especially during the pandemic, and your support helped me push through to the end. I'm looking forward to discussing physics and getting beers with you in the future.

Curriculum Vitæ

Craig Allen Holliman

Education

2022	Ph.D. in Physics (Expected), University of California, Santa Barbara
2021	M.A. in Physics, University of California, Santa Barbara
2017	B.A. in Physics, Mathematics, Bates College

Publications

Three-level ion optical clocks, C. A. Holliman, M. Fan, and A. M. Jayich. *In preparation.*

Measurement of the Ra^+ $7p^2P_{3/2}$ state lifetime, M. Fan, C. A. Holliman, A. Contractor, C. Zhang, S. Gebretsadken, and A. M. Jayich. *Physical Review A* **105**, 042801 (2022).

Radium Ion Optical Clock, C. A. Holliman, M. Fan, A. Contractor, S. M. Brewer, and A. M. Jayich. *Physical Review Letters* **128**, 033202 (2022).

Optical Mass Spectrometry of Cold $RaOH^+$ and $RaOCH_3^+$, M. Fan, C. A. Holliman, X. Shi, H. Zhang, M. W. Straus, X. Li, S. W. Buechele, and A. M. Jayich. *Physical Review Letters* **126**, 023002 (2021).

Direct measurement of the $7s^2S_{1/2} \rightarrow 7p^2P_{3/2}$ transition frequency in $^{226}Ra^+$, C. A. Holliman, M. Fan, A. Contractor, M. W. Straus, and A. M. Jayich. *Physical Review A* **102**, 042822 (2020).

Measurements of electric quadrupole transition frequencies in $^{226}Ra^+$, C. A. Holliman, M. Fan, and A. M. Jayich. *Physical Review A* **102**, 062512 (2019).

Measurement of the $7p^2P_{3/2}$ state branching fractions in Ra^+, M. Fan, C. A. Holliman, S. G. Porsev, M. S. Safronova, and A. M. Jayich. *Physical Review A* **100**, 062504 (2019).

Laser Cooling of Radium Ions, M. Fan, C. A. Holliman, A. L. Wang, and A. M. Jayich. *Physical Review Letters* **122**, 223001 (2019).

Abstract

Clocks, Qubits, and Searches for New Physics

by

Craig Allen Holliman

Trapped and laser cooled ions provide a robust platform for atomic frequency standards and quantum information architectures. Optical atomic clocks are now the most precise instruments ever realized. They have the potential to discover new physics beyond the standard model, including searches for ultralight scalar dark matter, the time variation of fundamental constants, and violations of Einstein's equivalent principle. The radium ion is a promising high-performance clock candidate, and its clock transitions have the largest positive enhancement factors to potential time variation of the fine structure constant. In this thesis we describe the first laser cooling and trapping of radium ions, measurements of fundamental atomic properties, and the development of a $^{226}Ra^{+}$ ion optical clock. We also discuss ongoing efforts towards the realization of $^{87}Sr^{+}$ and $^{225}Ra^{+}$ ion optical clocks. These species are suited for compact, transportable systems because of their magnetic-field-insensitive clock transitions and easily accessible wavelengths. Finally, we provide plans for work with $^{87}Sr^{+}$ and $^{225}Ra^{+}$ qubits.

Contents

Chapter 1

Introduction

The second is defined as the unperturbed ground-state hyperfine transition frequency (9,192,631,770 Hz) of cesium-133. Atoms have one important feature that makes them the ideal system for precision timekeeping and navigation: they are identical regardless of space and time. Accordingly, an atomic clock anywhere in the world will "tick" at the same frequency if environmental perturbations and relativistic effects are accounted for in the system. Atomic clocks are the enabling technology for global navigation satellite systems because of their extraordinary precision and robustness that allows them to measure the time delay between clocks on Earth and clocks in satellite orbit.

Optical atomic clocks, which are based on narrow-linewidth optical transitions, are the most precise instruments ever created [1]. These systems have set constraints on sources of new physics [2], and are promising for improved global positioning system and the redefinition of the second. In our group, we work with strontium and radium ions, which are promising for transportable optical clocks that can operate outside of the laboratory environment. An enabling feature for transportable optical clocks with these species is the integrated photonics compatible wavelengths. A radium ion clock is also promising for improving constraints on the time variation of the fine structure constant

because of its sensitive clock transition. Many of the same features that make these trapped ion systems appealing for a transportable optical clock also make them suitable for a qubit [3], which could be used for quantum computing.

Figure 1.1: The world's first trapped and laser cooled radium ion.

To me, two of the most exciting applications with ions are the development of trapped ion quantum computers and transportable optical clocks. It is satisfying to work on instruments that are not only sensitive enough to be used to constrain new physics, but also robust enough to have practical applications. A recently launched space-based trapped ion clock has already demonstrated performance that exceeds all other systems in space [4]. These systems can be developed at a small fraction of a percent compared to high-energy collaborations, and can be worked on in tabletop experiments operated by small teams. It is only a matter of time before a transportable optical clock, based on neutral atoms or trapped ions, rockets off to space, and I look forward to the navigational advances and new tests of general relativity that will follow.

1.1 Dissertation Overview

This thesis is divided into 14 chapters and 1 appendix. Chapter 2 provides an overview of three important aspects of working with ions: ion trapping, laser cooling, and ultra-high vacuum systems. Chapter 3 describes some appealing feature of alkaline-earth ions, and introduces the ion species used in this thesis. Chapter 4 covers the different atomic sources used in the experiment. Chapter 5 introduces the ion trap and other in-vacuum instruments. Chapter 6 then introduces experimental control devices that are outside of

the vacuum system. Chapter 7 details the first laser cooling and trapping of radium ions, and Chapter 8 the measurement of several fundamental radium ion atomic properties. Chapter 9 provides an introduction to the applications of atomic clocks, leading up to Chapter 10 and Chapter 11, which describe our work towards radium and strontium ion optical clocks. Chapter 12 proposes a new type of three-level optical clock operation that could be helpful to the development of transportable optical clocks. Chapter 13 provides an overview of how radium clocks could help improve constraints on new physics. Chapter 14 summarizes the operation and benefits of new qubits based on strontium and radium ions.

1.2 Permissions and Attributions

1. Some of the content of Chapter 7 is a result of a collaboration with Mingyu Fan, Anna Wang, and Andrew Jayich, and has previously appeared in *Physical Review Letters* [5]. It is reproduced here with the permission of Physical Review.

2. Some of the content of Chapter 8 is result of a collaboration with Mingyu Fan and Andrew Jayich, and has previously appeared in *Physical Review A* [6]. It is reproduced here with the permission of Physical Review.

3. Some of the content of Chapter 10 is result of a collaboration with Mingyu Fan, Asad Contractor, Samuel Brewer, and Andrew Jayich, and has previously appeared in *Physical Review Letters* [7]. It is reproduced here with the permission of Physical Review.

4. The content of Chapter 12 is a result of an ongoing collaboration with Mingyu Fan and Andrew Jayich.

Chapter 2

Background

This chapter describes three important aspects of work with ions: ion trapping, laser cooling, and ultra-high vacuum systems.

2.1 Ion Trapping

The derivations in this section follow those of [8, 9]. Linear Paul traps use static and oscillating radio frequency (rf) electric fields to confine ions [10]. The oscillating potential $V_0 + V_{\rm rf}\cos(\Omega t)$ is applied across a diagonal pair of radial electrodes and the static dc voltage, $V_{\rm dc}$, is applied to the endcap electrodes, see Fig. 2.1. The electric field near the center of the trap is approximately

$$\mathbf{E}(x,y,z,t) = -(V_0 + V_{\rm rf}\cos\Omega t)\left(\frac{x^2-y^2}{r_0^2}\right) - \frac{\kappa V_{\rm dc}}{z_0^2}\left[2z^2 - x^2 + y^2\right], \qquad (2.1)$$

where r_0 is the distance of the radial rod surface to the trap center, κ is a geometric factor that depends on the trap's geometry, and z_0 the distance from the axial trap center to the endcap electrodes. Because ions are charged they interact with the electric

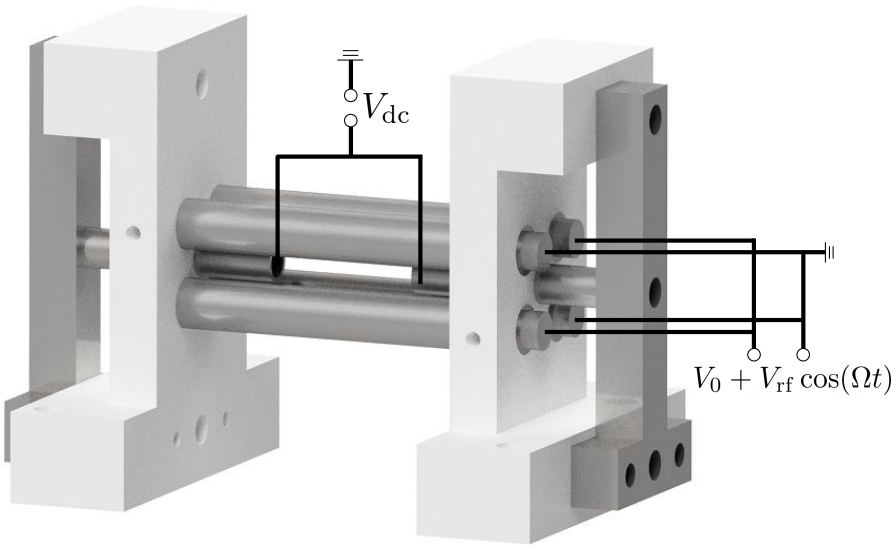

Figure 2.1: The linear Paul trap used throughout this thesis. Characteristic dimensions are $r_0 = 3$ mm and $z_0 = 7.5$ mm. An oscillating voltage, $V_0 + V_{\mathrm{rf}} \cos(\Omega t)$, is applied across a diagonal pair of radial electrodes. A static dc voltage, V_{dc}, is applied to the endcap electrodes.

field according to $\mathbf{F} = q\mathbf{E}/m$, where q is the charge of the ion and m is the mass of the ion. This interaction results in equations of motion of the form

$$\ddot{u}_i + [a_i + 2q_i \cos(\Omega t)]\frac{\Omega^2}{4} u_i = 0 \tag{2.2}$$

where $\mathbf{u} = u_x\hat{x} + u_y\hat{y} + u_z\hat{z}$ is the position of the ion with the origin defined as the trap center, and the Mathieu parameters a_i and q_i are

$$\begin{aligned} a_x &= a_y = -\frac{4q\kappa V_{\mathrm{dc}}}{m z_0^2 \Omega^2} \\ a_z &= \frac{8e\kappa V_{\mathrm{dc}}}{m z_0^2 \Omega^2} \\ q_x &= -q_y = \frac{2qV_{\mathrm{rf}}}{m r_0^2 \Omega^2} \\ q_z &= 0. \end{aligned} \tag{2.3}$$

The Mathieu stability parameters are

$$\begin{aligned} a &= \frac{4eV_0}{mr_0^2\Omega^2} \\ q &= -\frac{2eV_{\mathrm{rf}}}{mr_0^2\Omega^2}, \end{aligned} \tag{2.4}$$

where an ion will be stable in the trapping region if

$$\beta = \sqrt{a + \frac{q^2}{2}}. \tag{2.5}$$

The stable trapping region defined by a and q is shown in Fig. 2.2. To lowest order in

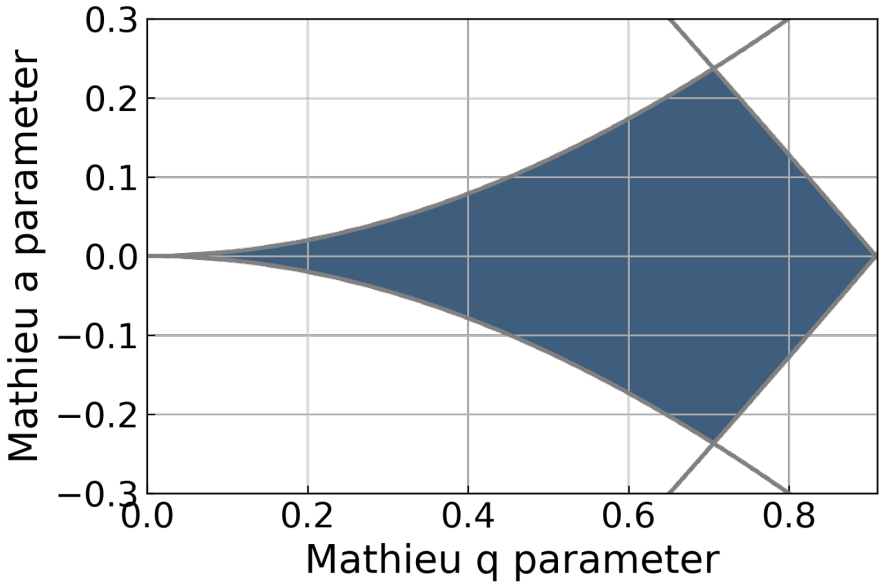

Figure 2.2: Stable trapping region (blue, shaded) for the Mathieu a and q stability parameters.

a_i and q_i, the solution to equation 2.2 is

$$u_i(t) \simeq \left[u_{1i}\cos\left(\omega_i t + \varphi_{Si}\right)\right]\left[1 + \frac{q_i}{2}\cos\left(\Omega t\right)\right], \tag{2.6}$$

where φ_{Si} is a phase determined by the initial conditions of the ion's position and velocity and ω_i is the secular frequency with amplitude u_{1i}. The secular frequency is

$$\omega_i \simeq \frac{\Omega}{2}\sqrt{\frac{q_i^2}{2} + a_i}. \tag{2.7}$$

In comparison, the axial secular frequency

$$\omega_z = \sqrt{\frac{2e\kappa V_{\mathrm{ec}}}{mz_0^2}}, \tag{2.8}$$

does not depend on the trap's rf frequency. The second term of equation 2.6 adds additional "micromotion" to the ion, which is driven at the trap rf frequency. Micromotion can alter the transition line shape, generate second-order Doppler shifts, and limit the trap lifetime in the absence of Doppler cooling [8]. Micromotion in an ion trap is minimized when the ion is equidistant from the trap rods.

2.2 Laser Cooling

Near-resonant driving of the $S_{1/2} \rightarrow P_{1/2}$ transition is used to reduce the kinetic energy of the ion in a process known as Doppler cooling. Because the ion is moving in a harmonic potential in the ion trap it will see the addressing frequency as blue detuned when it is moving towards the incident beam and red shifted when it is moving away from the incident beam. By red detuning the laser frequency that is driving the $S_{1/2} \rightarrow P_{1/2}$ transition, the ion is more likely to absorb a photon when it is moving towards the incident beam than when it is moving away from the incident beam. When the ion absorbs a photon it receives a "kick" in the direction opposite to its motion, slowing the ion in the trap. As another graduate student in the group once said, "it's like when you are swinging on a swing and a fan is only blowing when you are moving towards

it." By orienting the Doppler cooling beam at 45° with respect to all three trap axes we can effectively cool the ion's motion in all directions. The Doppler cooling limit T_{D} associated with this process is

$$T_{\mathrm{D}} = \frac{\hbar\Gamma}{2k_B} \tag{2.9}$$

where Γ is the linewidth of the Doppler cooling transition. At the Doppler cooling limit the mean phonon occupancy is

$$\bar{n}_{\mathrm{D}} = \frac{\Gamma}{2\omega_{\mathrm{s}}} \tag{2.10}$$

where ω_{s} is the secular frequency. During Doppler cooling the population can decay to the metastable $D_{3/2}$ state and an additional laser driving the $D_{3/2} \rightarrow P_{1/2}$ transition is needed to repump the population. Driving stimulated Raman transitions with the $S_{1/2} \rightarrow P_{1/2}$ and $D_{3/2} \rightarrow P_{1/2}$ transitions will keep the population in the $S_{1/2}$ and $D_{3/2}$ states. To avoid this phenomenon also known as coherent population trapping, we blue detune the laser frequency that is driving the $D_{3/2} \rightarrow P_{1/2}$ transition, and apply a small magnetic field at the ion of typically a few Gauss [11]. For a more complete derivation and explanation of Doppler cooling see [12] or *Atomic Physics* by Christopher J. Foot [13].

2.3 Ultra-high Vacuum Systems

For any ion trap, ultra high vacuum (UHV) pressure is needed for work with the ions. Background gas collisions between a trapped ion and neutral atoms or molecules increases the energy of the ion and can lead to decoherence or even cause the ion to be ejected from the trap. Depending on the atom or molecule collisions could cause a chemical reaction leading to the formation of a molecular ion, which would only be favorable if work with molecular ions was intended. For these reasons, a low background

gas pressure to decrease the collision rate is needed for work with ions. A combination of a turbomolecular pump, titanium sublimation pump, ion pump, and a high temperature bakeout are typically used to make the vacuum chamber pressure over a trillion times lower than that of the atmospheric pressure, at which the collision rate is $\ll 1$ Hz. We describe some of the instruments and techniques used in this thesis in more detail in section 5.3.

Chapter 3

Strontium and Radium

This chapter provides an overview of strontium and radium, two alkaline-earth elements used in this thesis.

3.1 Alkaline-earth Elements

Alkaline-earth elements, see Fig 3.1, are readily used in atomic physics, both in neutral atom and ion trapping experiments. When ionized, alkaline-earth elements have a simple level structure that makes them amenable to direct laser cooling, see Fig. 3.2 and Fig. 3.6. Barium and magnesium ions were first laser cooled and trapped nearly half a century ago [14, 15]. Since then, the other alkaline-earth elements have joined the ranks, with the radium ion being the most recent to be laser cooled just three years ago [5]. Alkaline-earth ions including Ca^+, Sr^+, Ba^+, and Ra^+ are particularly favorable for quantum information science due to their wavelengths that are suitable for integrated photonics and their long-lived metastable state lifetimes [3]. Several efforts seek to leverage these diode-friendly wavelengths to realize transportable optical clocks with Ca^+ [16] and Sr^+ [17]. With the exception of radium, which has no stable isotopes, the alkaline-earth

elements tend to have several stable isotopes that can have their clock transition measured to high precision. Isotope shift spectroscopy can then be used to constrain sources of new physics [18, 19].

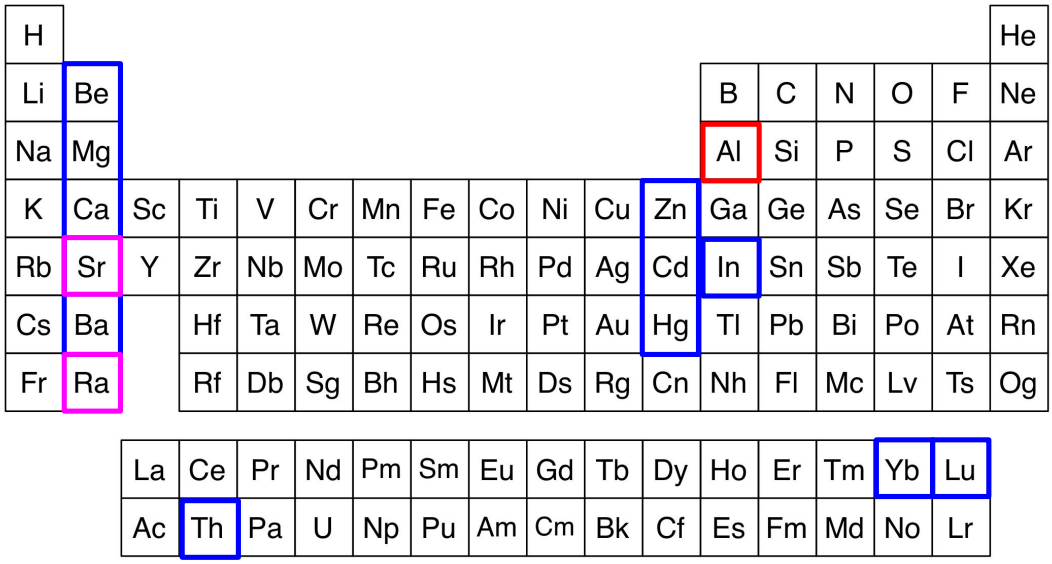

Figure 3.1: Periodic table of elements. Species that have been directly laser cooled are boxed in blue, and species that have been sympathetically cooled are boxed in red. Species used in our lab, strontium and radium, are boxed in purple.

3.2 Strontium

There are four naturally occurring isotopes of strontium that are suitable for work in an ion trap, see Table 3.1. Of these, three of the isotopes ^{84,86,88}Sr have nuclear spin

Table 3.1: Naturally occurring isotopes of strontium.

Isotope	Abundance	Nuclear Spin
84	0.5%	0
86	10.0%	0
87	7.0%	9/2
88	82.5%	0

$I = 0$, and the fourth ^{87}Sr has nuclear spin $I = 9/2$. In our group, we primarily work with

$^{87}Sr^{+}$ and $^{88}Sr^{+}$. We describe these isotopes in more detail in the following subsections.

3.2.1 $^{88}Sr^{+}$

Strontium-88 is the most abundant isotope of strontium. Most notably, the $^{88}Sr^{+}$ ion has been used to realize a high-precision optical clock [20] and a dual-species two-qubit gate with Ca^{+} [21]. Future efforts seek to leverage the ion's integrated-photonic compatible wavelengths, see Fig. 3.2, to realize a compact transportable optical clock [17, 22]. In a $^{88}Sr^{+}$ clock, the transition closest to the ultraviolet (UV) is the Doppler cooling transition at 422 nm, which is suitable for integrated photonic waveguides [23].

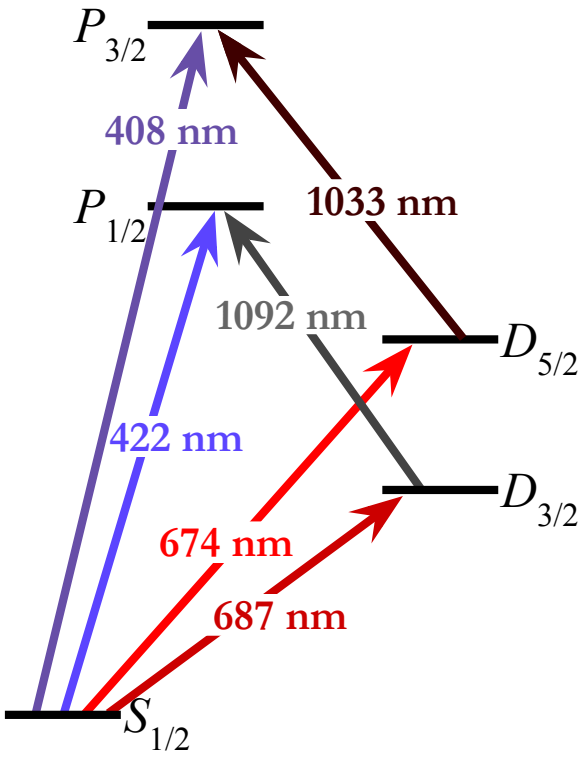

Figure 3.2: Low-lying energy structure of Sr^{+}.

In our lab we trap $^{88}Sr^{+}$ ions, see Fig. 3.3, to calibrate ion traps, ensure all electronic systems are working, and verify that all fiber ports and imaging systems are aligned. The

ion also serves as a useful testbed for experiments with radium ions, where many fundamental properties had never been measured experimentally. The strontium-88 source, which we describe in more detail in Section 4.1.1, is also used to produce strontium-87 atoms.

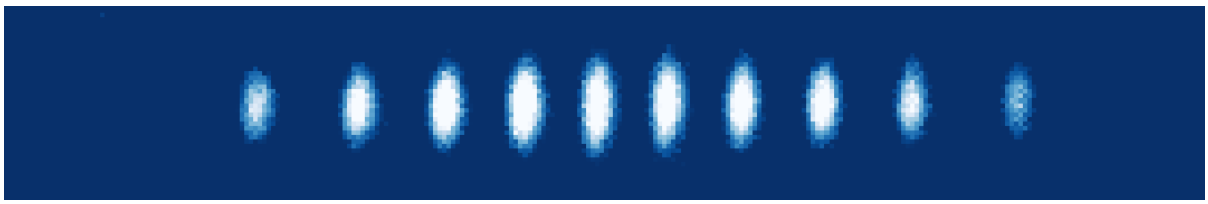

Figure 3.3: Ten trapped and laser cooled $^{88}Sr^{+}$ ions.

3.2.2 $^{87}Sr^{+}$

The $^{87}Sr^{+}$ ion has a high nuclear spin, $I = 9/2$, compared to most ion species used in existing experiments with trapped ions. The high nuclear spin gives rise to several hyperfine levels in the $D_{3/2}$ and $D_{5/2}$ metastable states, see Fig. 3.4. This rich structure creates several interesting clock transitions between the $S_{1/2}$ and $D_{5/2}$ clock state, some of which are desirable for their magnetic field insensitivity, and some which are promising for minimizing other systematics such as the electric quadrupole shift. We discuss our work towards a $^{87}Sr^{+}$ ion clock in Chapter 11, and plans for a $^{87}Sr^{+}$ qubit in Chapter 14. Existing measurements of hyperfine constants are summarized in Table 3.2.

Table 3.2: Summary of $^{87}Sr^{+}$ hyperfine constants (MHz).

State	A	B
$S_{1/2}$	-1000.47367(11) [24]	-
$P_{1/2}$	-175.12 [25]	-
$P_{3/2}$	-36.0 [26]	88.5 [26]
$D_{3/2}$	-45.60 [27]	41.04 [27]
$D_{5/2}$	2.1743(14) [28]	49.11(6) [28]

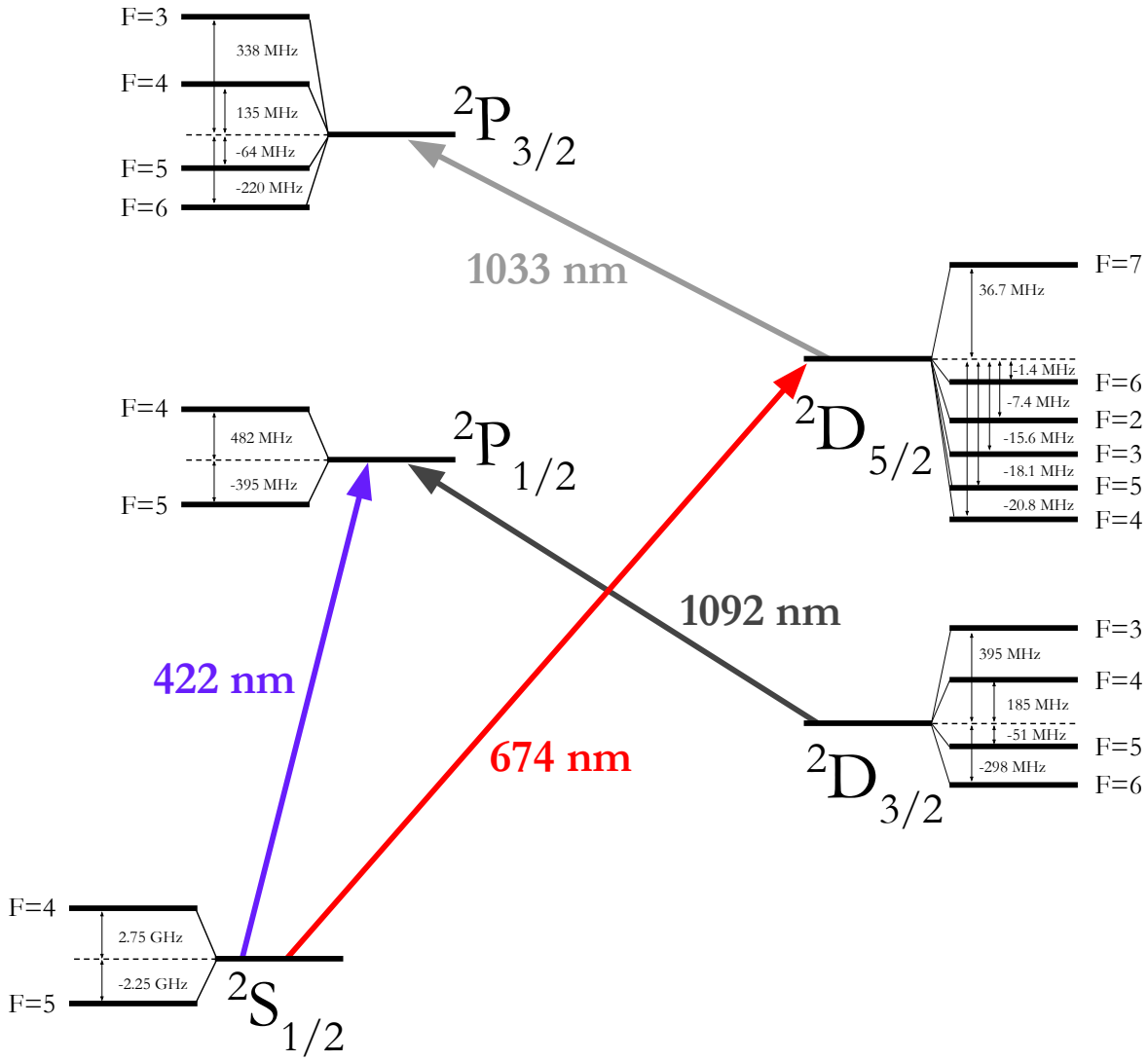

Figure 3.4: Low-lying energy structure of $^{87}Sr^+$ showing the transitions needed for optical clock operation.

3.3 Radium

Radium is the heaviest alkaline-earth element. There are no stable isotopes of radium, but several isotopes have half-lives that are longer than a few days, and are suitable for work in a closed system ion trap, without the need to break vacuum, see Table 3.3. The

radium nucleus has an octupole deformation that enhances its sensitivity to CP violating physics [29, 5], and makes the atom appealing for work with molecular ions, where the large internal electric field serves as a further enhancement to sources of new physics [30, 31]. The radium ion is also appealing as a high-performance optical clock [32, 7]. Similar to the strontium ion, the radium ion has transition wavelengths that are suited for integrated photonics, see Fig. 8.1. Radium is famously radioactive, which makes an ion trap well-suited for measurements because only a trace quantity of the element is required in the vacuum chamber for long-term work [33, 5]. Alternatively, nuclear facilities with online sources can be used for work with short-lived radium isotopes [34]. In our group, we currently work with $^{226}Ra^{+}$, and are moving towards work with $^{225}Ra^{+}$. We describe these isotopes in more detail in the following subsections.

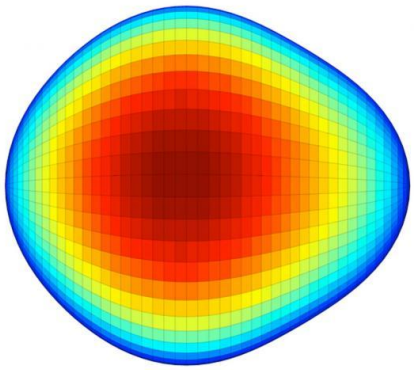

Figure 3.5: Radium's pear-shaped octupole deformed nucleus enhances its sensitivity to sources of new physics.

Table 3.3: Radium isotopes with half-lives that are longer than one day.

Isotope	Half-life	Nuclear Spin	Parent	Parent's Half-life
223	11.4 d	3/2	Actinium-227	21.8 y
224	3.6 d	0	Thorium-228	1.9 y
225	14.9 d	1/2	Thorium-229	7900 y
226	1600 y	0	-	-
228	5.8 y	0	Thorium-232	10^{10} y

3.3.1 $^{226}Ra^{+}$

Radium-226 is the longest-lived radium isotope with a half-life of 1600 years. The long half-life enables direct work with the radioisotope in a sealed vacuum system [5]. We detail the atomic source in more detail in Section 4.2. The nuclear spin $I = 0$ of $^{226}Ra^{+}$ provided a simple energy structure for the first laser cooling and trapping of the ion, which we describe in detail in Chapter 7. The $^{226}Ra^{+}$ ion was also used for measurements of several fundamental atomic properties and an optical clock, which we describe in Chapter 8 and Chapter 10.

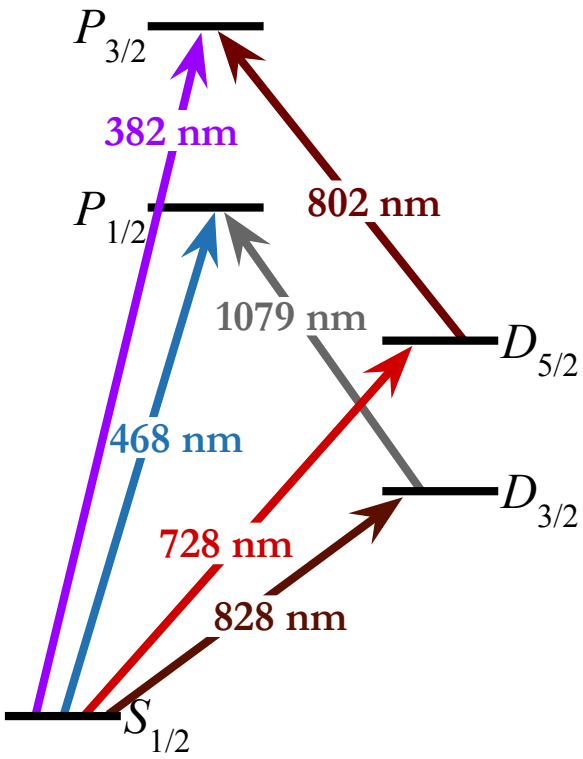

Figure 3.6: Low-lying energy structure of Ra^{+}.

3.3.2 $^{225}Ra^{+}$

The $^{225}Ra^{+}$ ion has nuclear spin $I = 1/2$ and a 14.9 day half-life. The relatively short lifetime of radium-225 means that while the isotope can be worked with directly in a sealed system, it would be better to generate atoms from the decays of the parent isotope thorium-229 [33]. Current efforts towards the generation of radium-225 atoms are described in Section 4.1. Plans for a $^{225}Ra^{+}$ ion optical clock are described in Section 10.3, and plans for a $^{225}Ra^{+}$ qubit in Section 14.3.3. The energy structure and needed transitions for a $^{225}Ra^{+}$ ion optical clock are shown in Fig. 3.7. Hyperfine constants of the $S_{1/2}$, $P_{1/2}$, and $P_{3/2}$ states have been experimentally measured, see Table 3.4, and theoretical calculations exist for the $D_{3/2}$ and $D_{5/2}$ metastable states.

Table 3.4: Summary of $^{225}Ra^{+}$ hyperfine constants (MHz).

State	A	B
$S_{1/2}$	-27731(13) [35]	-
$P_{1/2}$	-5446(7) [36]	-
$P_{3/2}$	-466.4(4.6) [35]	-
$D_{3/2}$	-626.13 [37]	-
$D_{5/2}$	194.15 [37]	-

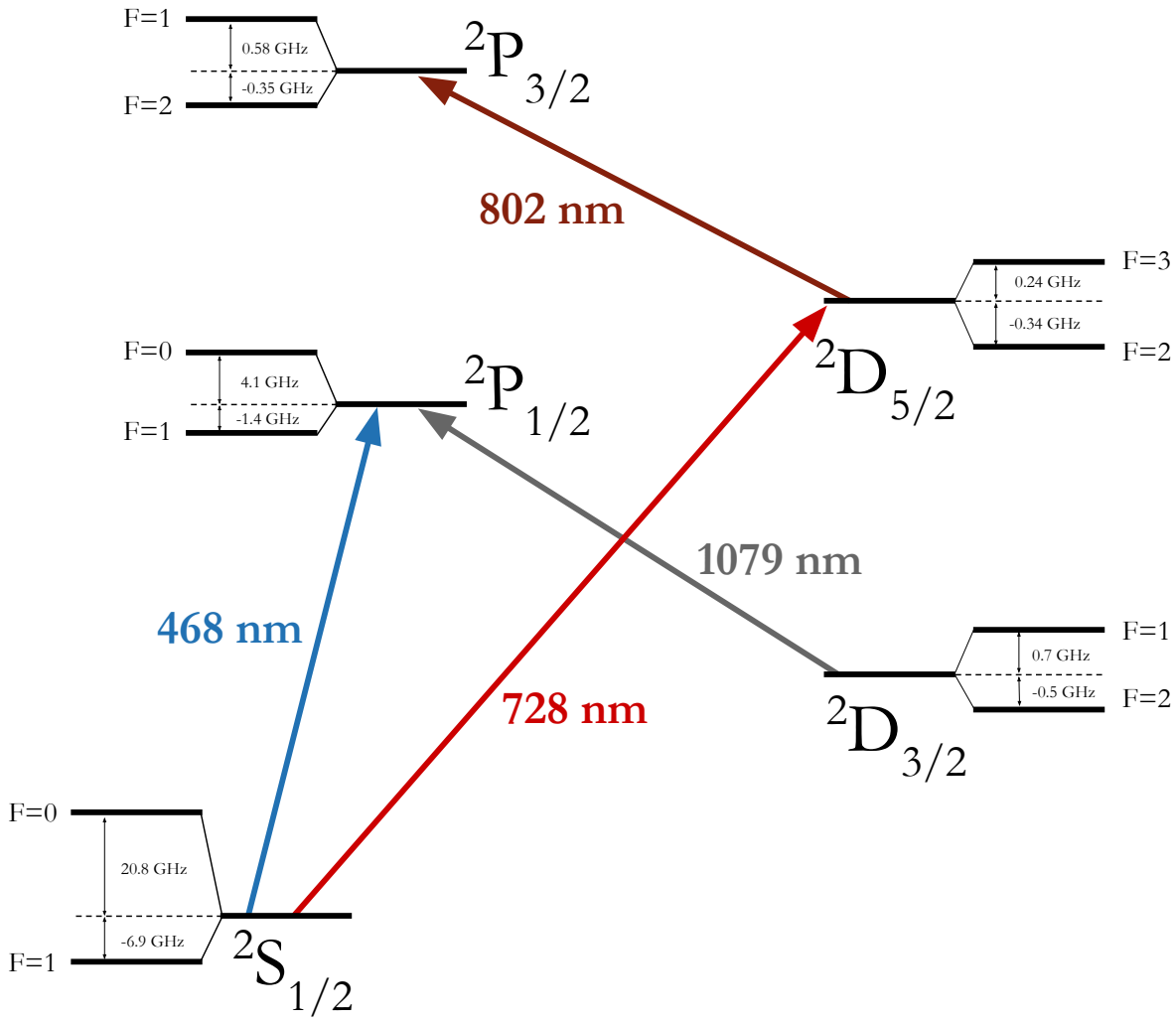

Figure 3.7: Low-lying energy structure of $^{225}Ra^{+}$ showing the transitions needed for optical clock operation.

Chapter 4

Atomic Sources for Ion Trapping

Reliable offline atomic sources are needed for long-term work with an element in a closed vacuum system. This chapter describes the methods we used to load strontium and radium ions into our linear Paul trap.

4.1 Atomic Ovens

Atomic ovens are a reliable method of generating neutral atoms that can be ionized to load the ion trap using two-step photoionization [38]. We describe two types of atomic ovens, an effusive oven that is suited for strontium or radium atoms, and an orthotropic oven design that we are working on for radium atom generation. We also provide an overview of photoionization of neutral atoms.

4.1.1 Effusive Oven

Our group uses two different kinds of effusive ovens, the first a homemade oven, see Fig. 4.1, and the second a 3D-printed oven that can be custom designed, see Fig. 4.2. The 3D-printed oven is described in detail with part files available on GitHub.

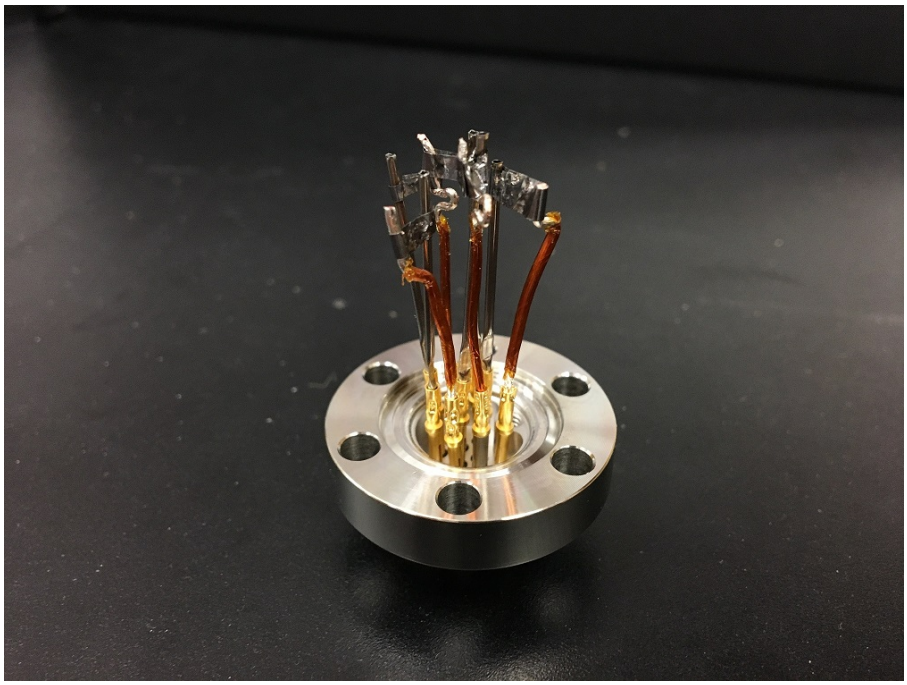

Figure 4.1: Effusive oven made using stainless steel tubes and mounted on a 1.33" CF flange. Cooper wires and stainless steel tubes can be seen crimped to the gold female contacts. Four ovens are connected to their own ground for operation. Tantalum foil is spot welded around the stainless steel oven and the copper ground connection.

We use the following parts for our homemade oven:

1. Stainless steel tubes (McMaster-Carr 89935K69)
2. 1.33" CF flange with c-type feedthrough and cable (Accu-Glass 100000)
3. Female contacts (Accu-Glass 110908)
4. Kapton insulated solid core copper wire (Accu-Glass)
5. Tantalum foil

The stainless steel tubes are cut to a length that is suitably close to the ion trap. We typically cut them to be $\sim$ 25 mm long. The kapton insulated wire is cut to the same length and stripped on both ends. The stainless steel tube and the kapton wire are

placed in female contacts and crimped to secure them in place. They are then mounted on the CF flange. The tantalum foil is cut into a thin strip such that it can be folded around the stainless steel tube and the kapton wire. The foil is spot welded in place to provide a suitable resistance for operation. We typically aim for a resistance of 1Ω. This results in a fully built oven that is ready for atomic effusion. We usually make four ovens on a nine-pin flange to serve as backup ovens. Next, strontium is added to the ovens in a glove box that is circulating argon to keep the strontium from oxidizing during the transfer process. With the strontium loaded in the four ovens, the entire assembly is mounted to the vacuum chamber. We begin pumping on the chamber immediately after mounting the flange to preserve as much of the element as possible.

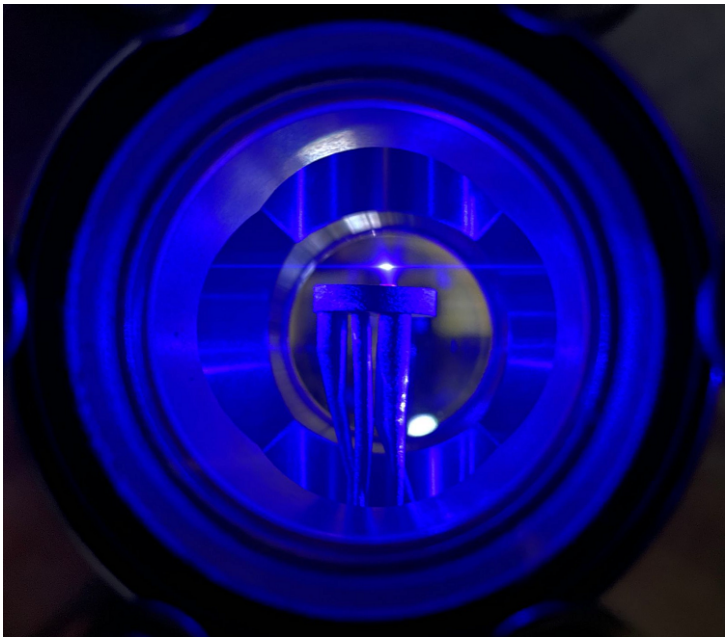

Figure 4.2: 3D-printed titanium oven being tested a in a vacuum cube. Neutral strontium fluorescence at 461 nm can be observed as a brightly glowing dot directly above the oven aperture, and a thin line that traces the path of the laser beam.

While we have primarily shifted to using the 3D-printed oven due to the flexibility in design and the ease of construction, the homemade ovens do have the advantage of being extremely cheap and easy to modify on the spot.

4.1.2 Orthotropic Oven

The first orthotropic oven was designed for work with short-lived ($\sim$ 5 min) isotopes of francium [39]. Because of radioactivity, only a small quantity of francium's parent isotope actinium could be contained in the oven at a given time. As such, maximizing the oven yield by minimizing the atomic beam divergence out of the oven was desired. An orthotropic oven accomplishes this by using surface ionization of the metals inside the oven. The concept is based on the Saha-Langmuir equation that gives the ratio of the released ions to atoms from the surface of the material

$$\frac{n_+}{n_0} = \frac{\omega_+}{\omega_0} e^{\frac{\epsilon(E_{\rm wf} - E_{\rm ip})}{kT}} \tag{4.1}$$

where $\frac{\omega_+}{\omega_0}$ is the ratio of statistical weights, ϵ is the electron charge, $E_{\rm wf}$ is the surface work function, and $E_{\rm ip}$ is the ionization potential of the atom [40]. The ratio $\frac{n_+}{n_0}$ will depend on the work function $E_{\rm wf}$ of the metal surface and the ionization potential $E_{\rm ip}$ of the atom. When $E_{\rm ip} < E_{\rm wf}$ most of the evaporated atoms are emitted as ions, and when $E_{\rm ip} > E_{\rm wf}$ most of the evaporated ions are neutralized. Thus, by using electroplated Pt ($E_{\rm wf} = 5.6$) and Y ($E_{\rm wf} = 3.1$) with a positive and negative bias applied, a very tight orthotropic source can be created as ions from the oven surface will be attracted to the neutralizer, but only atoms that have a line-of-sight out of the oven will leave, see Fig. 4.3. Commonly used metals and their work functions are shown in Table 4.1.

Table 4.1: Possible material for an orthotropic oven.

Element	Melting Point (°C)	Work Function E_{wf} (eV)
Yttrium (Y)	1526	3.1
Tantalum (Ta)	3017	4.1
Stainless Steel	1400	4.4
Nickel (Ni)	1455	5.0
Gold (Au)	1060	5.1
Platinum (Pt)	1768	5.6

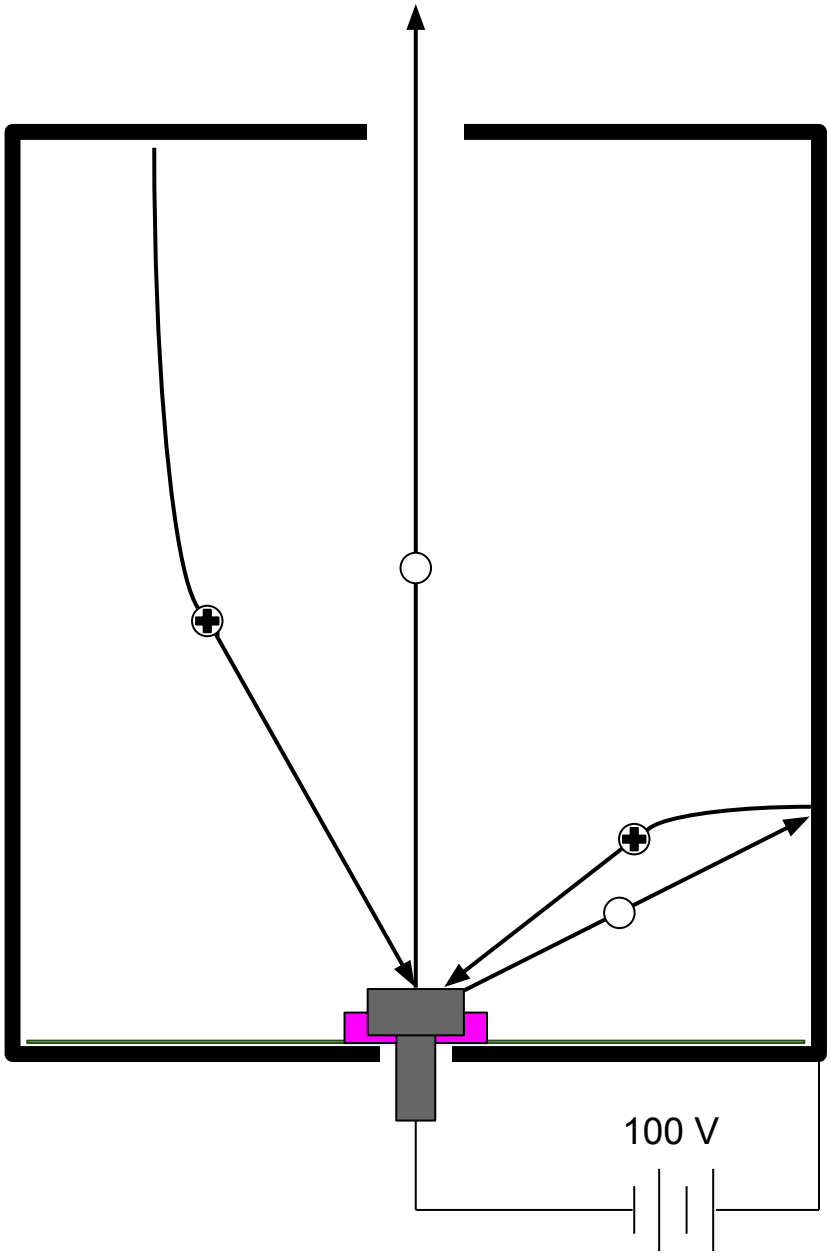

Figure 4.3: Diagram of orthotropic oven operation. Atoms that are evaporated from the walls of the oven are statistically likely to come off as ions and be attracted to the negatively biased neutralizer (gray) at the base of the oven. When heated off the neutralizer the ions will become neutralized and atoms will have a chance to exit the oven through a small aperture at the top. Otherwise the atoms will strike the wall of the oven and the process will repeat.

For work with radium, the neutralizer can be made out of stainless steel due to the high ionization energy of radium compared to francium, see Table 4.2. To continuously populate our orthotropic oven we use thorium which alpha decays to radium, see Fig 4.4. For testing of our orthotropic oven we use thorium-228 because it is less expensive than thorium-229, which is desirable for medical applications [41].

Table 4.2: Candidates for an orthotropic oven.

Element	Melting Point (°C)	Ionization Energy E_{ip} (eV)
Francium	650	4.0
Barium	730	5.2
Radium	700	5.3
Strontium	777	5.7
Calcium	842	6.1
Thorium	1750	6.1

Our current orthotropic oven design is shown in Fig. 4.5. We place a nickel foil that has dried thorium chloride at the bottom of the stainless steel crucible. Macor is used as an insulator for the neutralizer connection and for the tantalum wire which serves as the heating element. The inside of the crucible is lined with 0.0005" thick Pt foil from ESPI metals. The crucible is surrounded with gold plated copper for heating efficiency. The entire assembly fits inside a 3.38 CF nipple.

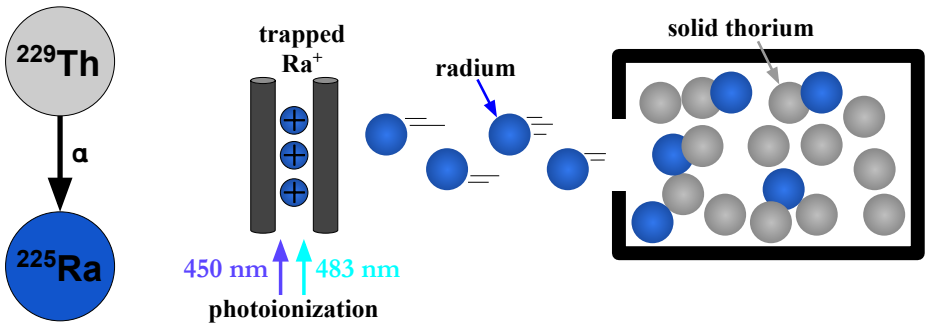

Figure 4.4: Loading of Ra^+ from a thorium oven. Thorium decays to radium via alpha decay and embeds in the walls of the oven. When heated, the radium atoms will diffuse from the oven walls and be photoionized by light at 450 and 483 nm.

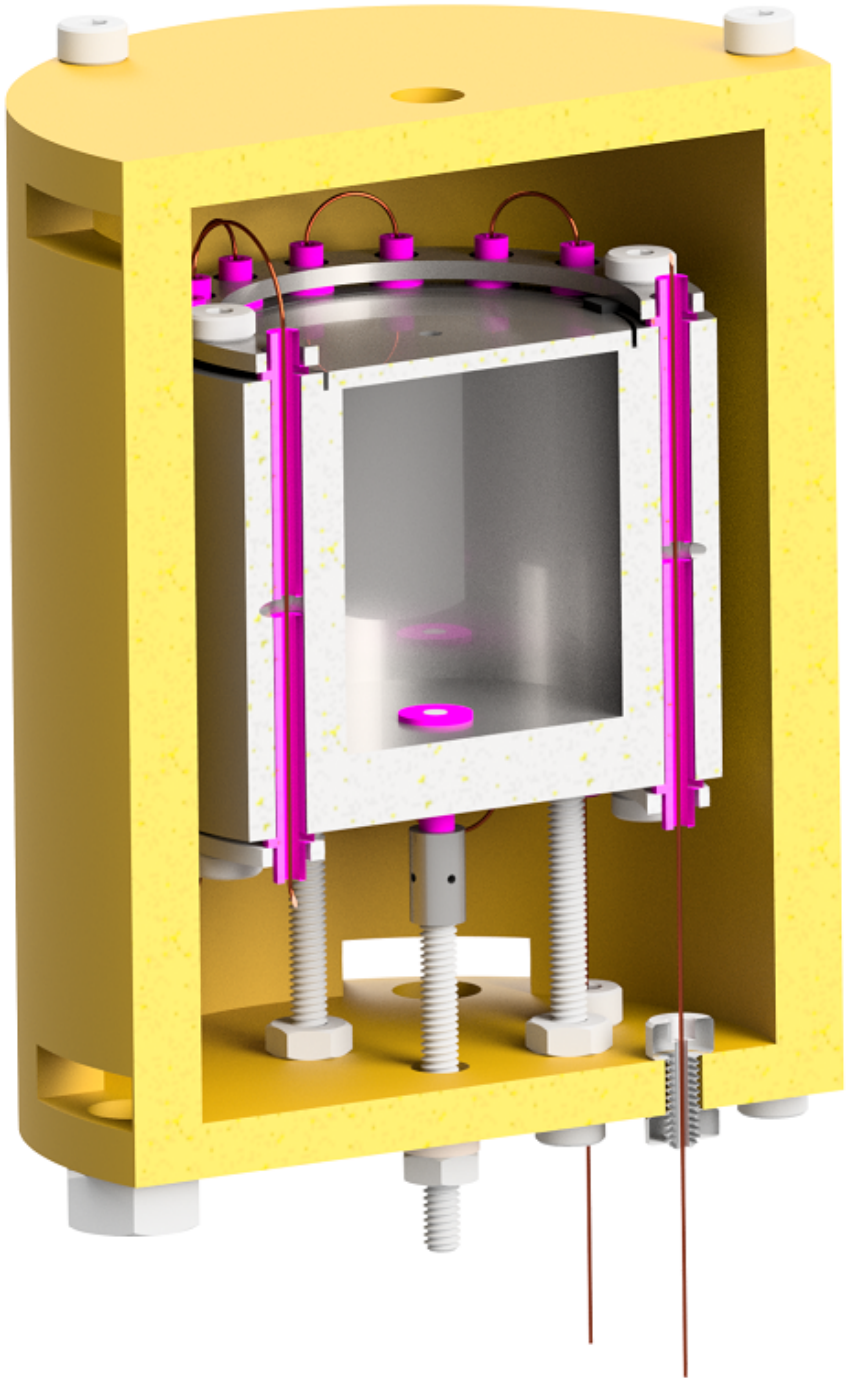

Figure 4.5: Render of the orthotropic oven. Platinum coated stainless steel parts (silver), macor insulators (pink), and tantalum wire (copper) are shown.

To evaluate the performance of the orthotropic oven we look for fluorescence by driving the neutral radium $^1S_0 \rightarrow {}^1P_1$ transition with 483 nm light. The frequency of the 483 nm light is tuned to resonance by referencing a nearby Te_2 absorption line [42], and existing absolute frequency measurements and isotope shifts [36, 33]. We also detect emitted gammas at a window opposite to the oven. The gamma spectrometer (Ludlum Model 732) channels are calibrated to the thorium-228 and radium-226 sources in our lab. The oven is heated to $\sim$ 1000 C, and runs for 60 minutes. We do not detect any fluorescence, but we do see a small increase in the gammas near the radium and lead peak, see Fig. 4.6. Unfortunately, the resolution of the device is not enough to individually distinguish between the two peaks. Ongoing efforts seek to better understand the chemistry behind the thorium sample preparation to improve the yield from the oven.

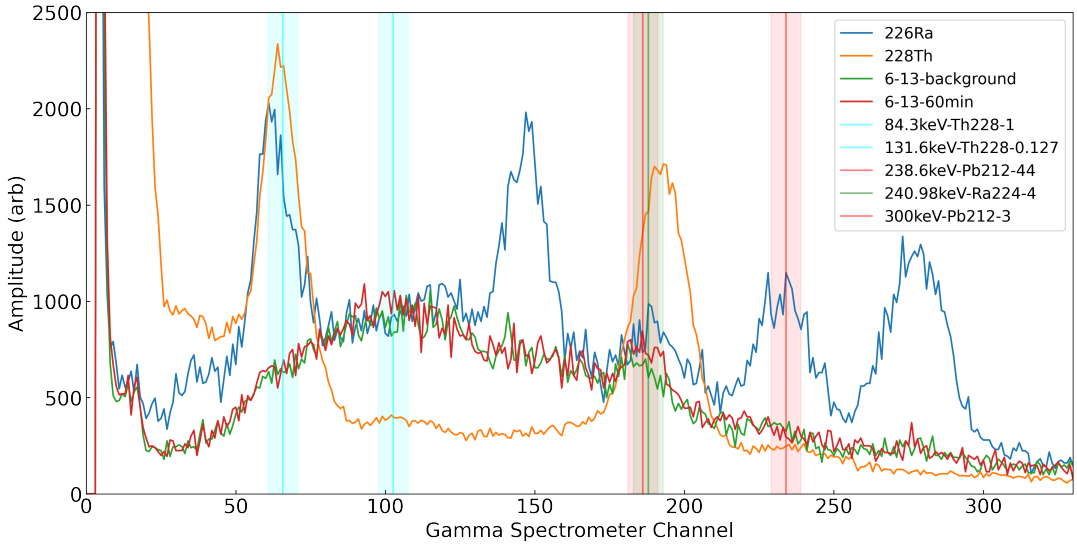

Figure 4.6: Gamma spectroscopy of the orthotropic oven. The Ludlum Model 732 gamma spectrometer was calibrated using an existing ^{226}Ra source. Vertical lines show the characteristic gammas emitted from the thorium-228 decay chain. The green trace show the background of the gamma spectrometer placed approximately one meter from the orthotropic oven. After one hour a small increase in the counts near the radium 240.98 keV line is observed, but due to sensitivity of the device it is not possible to distinguish the counts from the lead-212 238.6 keV line.

4.1.3 Photoionization

With neutral atoms produced, and their flux oriented into the trap it is then possible to load the ion trap by ionizing the atoms with resonant laser light. Two-step photoionization is commonly used to efficiently load specific isotopes of alkaline-earth elements [38]. The photoionization wavelengths for strontium and radium are shown in Fig. 4.7. The $^1S_0 \rightarrow {}^1P_1$ transition is sensitive to its frequency, while the light driving the population to the continuum can generally be free running with nm-level insensitivity for the frequency. Neutral atom fluorescence from driving the $^1S_0 \rightarrow {}^1P_1$ transition is shown in Fig. 4.2.

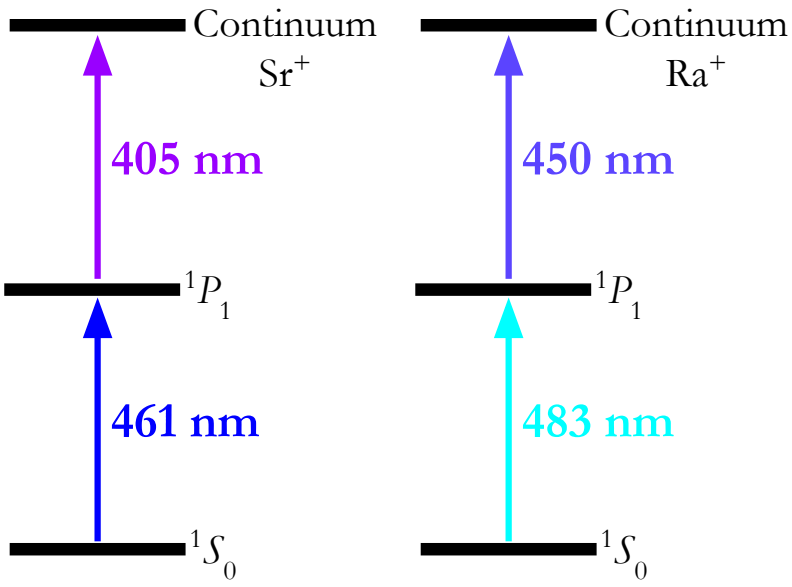

Figure 4.7: Two-step photoionization of strontium and radium.

4.2 Laser Ablation

Laser ablation of a target with a high-energy pulse can be used to directly load ions into a trap [43, 44], and is particularly useful for work with a trace quantity of an isotope,

such as barium-133 [45]. Because the half-life of radium-226 is 1600 years, see Table 3.3, it is possible to work with the radioisotope directly in the vacuum system without relying on decays from a parent isotope. Our radium-226 sample was purchased from Eckert & Ziegler who provided 10 μCi of radium-226 dissolved into 5 mL of 0.1M HCl, and shipped to us in a sealed ampule, see Fig. 4.8.

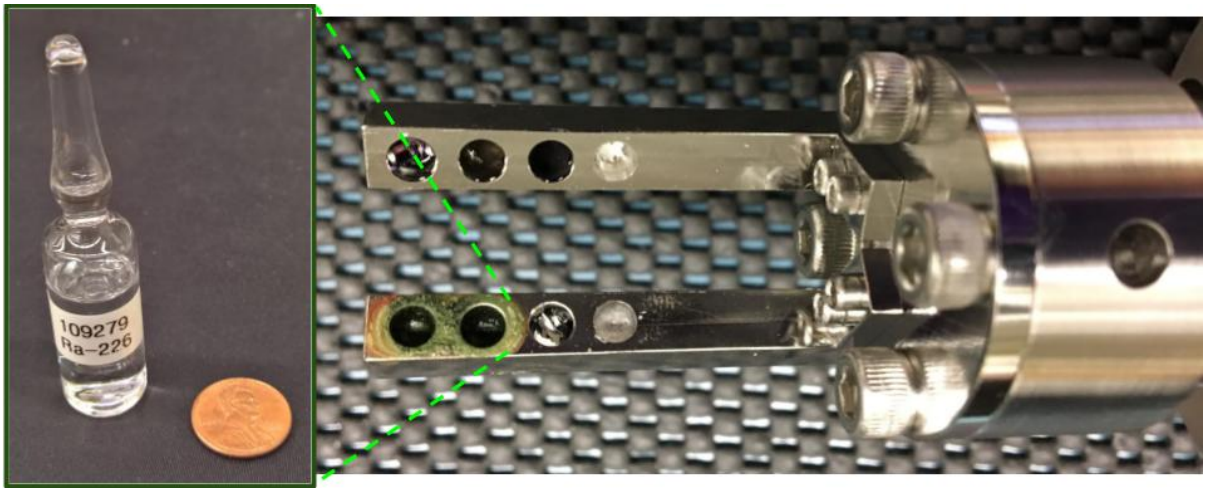

Figure 4.8: 10 μg (10 μCi) are contained in a solution of hydrochloric acid (left). This solution is dried into a target holder (right) that is attached to a heavy duty linear push-pull feedthrough.

To transfer the activity a stainless steel target holder, see Fig. A.1, is placed on a heated hot plate that was covered with aluminum foil. The one point cut ampule is opened and clamped securely in a vertical position to avoid spilling the activity. Using a 0.5 mL volume syringe the activity is transferred slowly into the two front bowls of the target holder. We let the solution dry fully before transferring more activity from the ampule. Two graduate students working in shifts transferred the activity from the ampule to the target holder in less than 6 hours. The target holder was then wrapped in a sealed plastic bag and taken to the vacuum chamber where it is mounted onto a stainless steel adapter plate, see Fig. A.1, and screwed into a linear motion feedthrough (Heavy Duty Linear Push Pull Feed Through, 2.75" CF Flange), see Fig. 4.8. The entire

assembly is then mounted to the vacuum chamber, see Fig. 5.4.

All work for transferring the activity to the stainless steel target holder was done in a fume hood wrapped with aluminum foil. The two graduate students who transferred the activity wore gloves, lab coats, safety glasses, and RAD-60R dosimeters for the duration of the process. After completion a Ludlum Model 3 general purpose survey meter was used to verify that there was no residual activity in the work space.

Chapter 5

The Enterprise Ion Trap

This chapter describe the "Enterprise" linear Paul trap used in our experiment and the associated vacuum system and internal components.

5.1 Ion Trap

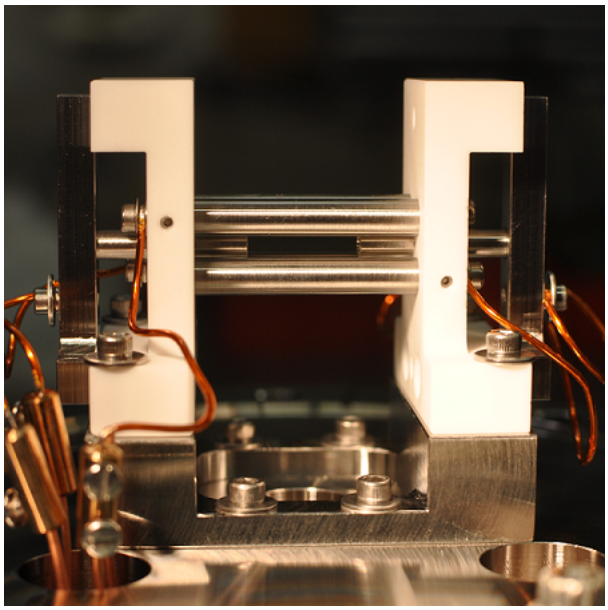

Figure 5.1: Picture of the Enterprise ion trap. Characteristics dimensions are $r_0 = 3$ mm and $z_0 = 7.5$ mm.

The Enterprise trap is a non-segmented linear Paul trap. Stainless steel rods 5 mm in diameter are placed into macor supporting pieces that are held in place with a stainless steel mounting plate, see Fig. 5.1. The rods were electropolished prior to use.

5.2 Trap Stability

As discussed in Chapter 2, the Mathieu stability parameters from equation 2.4 determine if an ion can stably trapped. The Enterprise trap is a relatively large trap with characteristics dimensions are $r_0 = 3$ mm and $z_0 = 7.5$ mm. This is advantageous when trying to work with two different species because for a fixed rf drive frequency there is a considerably wide range of voltages where the two ions can be trapped simultaneously, see Fig. 5.2.

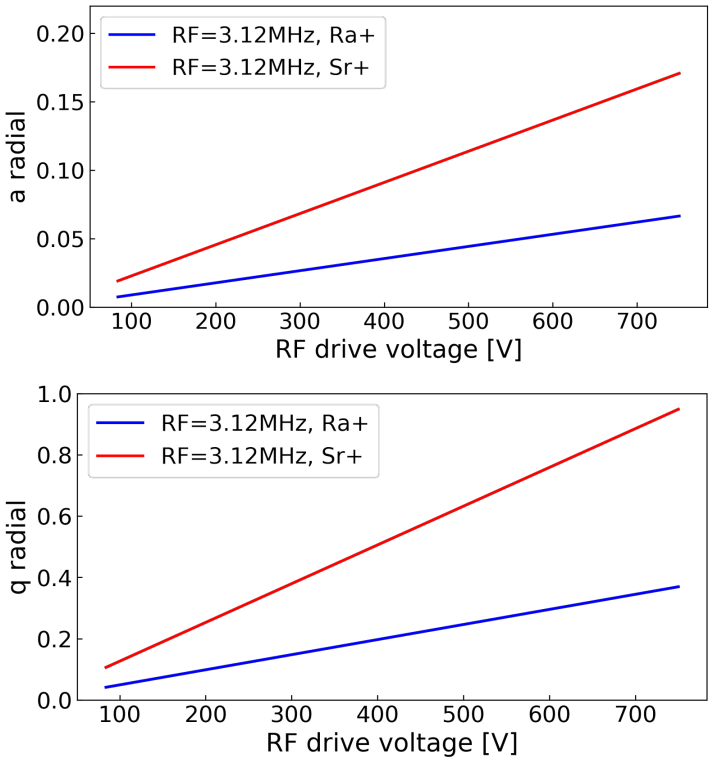

Figure 5.2: Mathieu a and q parameters for Sr^+ and Ra^+ at a fixed trap drive frequency (3.12 MHz).

5.3 Vacuum

To obtain low vacuum pressure in the system we do the following:

1. All stainless steel parts are sonicated three times, once in a Simple Green bath, once in an acetone bath, and once in a methanol bath. The parts are then rinsed with deionized water and dried with nitrogen. They are then wrapped in UHV vacuum foil until the system is ready for construction.

2. The vacuum system is constructed while wearing hair nets, gloves, and arm sleeves.

3. The system is baked out at a temperature of $\sim$ 200 C in a large oven (LAC2 - Despatch) that can fit the breadboard the system is mounted on.

4. During the bake the system is pumped down with a turbo molecular pump (HiPace - Pfeiffer Vacuum). The partial pressures are monitored with a residual gas analyzer (XT100M) throughout the bakeout.

5. After a few weeks when the partial pressures are not improving any further we turn on the ion pump (VacIon Plus 20 - Starcell), close the valve to the turbo pump, and begin ramping down the oven temperature.

6. Once the system is back in the lab we run the titanium sublimation pump (TSP-275-003 - Duniway) for approximately one minute.

7. The pressure in the vacuum system is measured with an ion gauge (XGS-600 - Varian). After following the steps above we observe pressures in the low e-10 mbar range a few days later.

5.4 Time-of-flight Mass Spectrometery

For initial, non-optical detection of radium ion loaded by ablation, see Chapter 4, a time-of-flight mass spectrometer (TOFMS) was constructed following the design at UCLA [46]. By applying a high voltage on the two rods farther away from the TOFMS, see Fig. 5.3, and dropping the voltage on the two rf rods closer to the TOFMS, the ions are ejected in the direction of the TOFMS. A skimmer at the front of the TOFMS prevents ions with large ejection angle from entering the TOFMS to maintain the mass resolution of the instrument. After the skimmer, two sets of Einzel lens focus the ions towards the end of the TOFMS where a channel electron multiplier (CEM) detects the signal. We used the Channeltron Mass Spectrometer Detector CEM 5901 MAGNUM COA SL from Photonis in our TOFMS. All other parts follow the design in [46]. The loading of radium ions and the TOFMS calibration with co-trapped strontium and radium ions are described in more detail in Chapter 7.

Figure 5.3: Render of the TOFMS and the Enterprise linear ion trap.

5.5 Atomic Sources

Atomic sources for strontium and radium were used in this thesis. For strontium, a homemade oven following the design presented in Chapter 4 was built. The oven is mounted on a 1.33 CF flange and attached to the octagon directly below the ion trap. The 461 nm fluorescence from driving the ${}^1S_0 \rightarrow {}^1P_1$ transition with a high current (~ 5 A) can be clearly observed in Fig. 5.4.

For radium, a dried radium chloride solution following the procedure in Chapter 4 was used. The laser ablation target holder and mount designs are shown in Appendix A. The linear motion feedthrough can be seen on the left side of Fig. 5.4. The length of the target mounts were chosen such that beams aligned radially would not clip on the linear motion feedthrough even if adjusted for ablation of the farthest bowl. Additional elements besides the $RaCl_2$ sample were prepared in other bowls, though they were not used in this thesis.

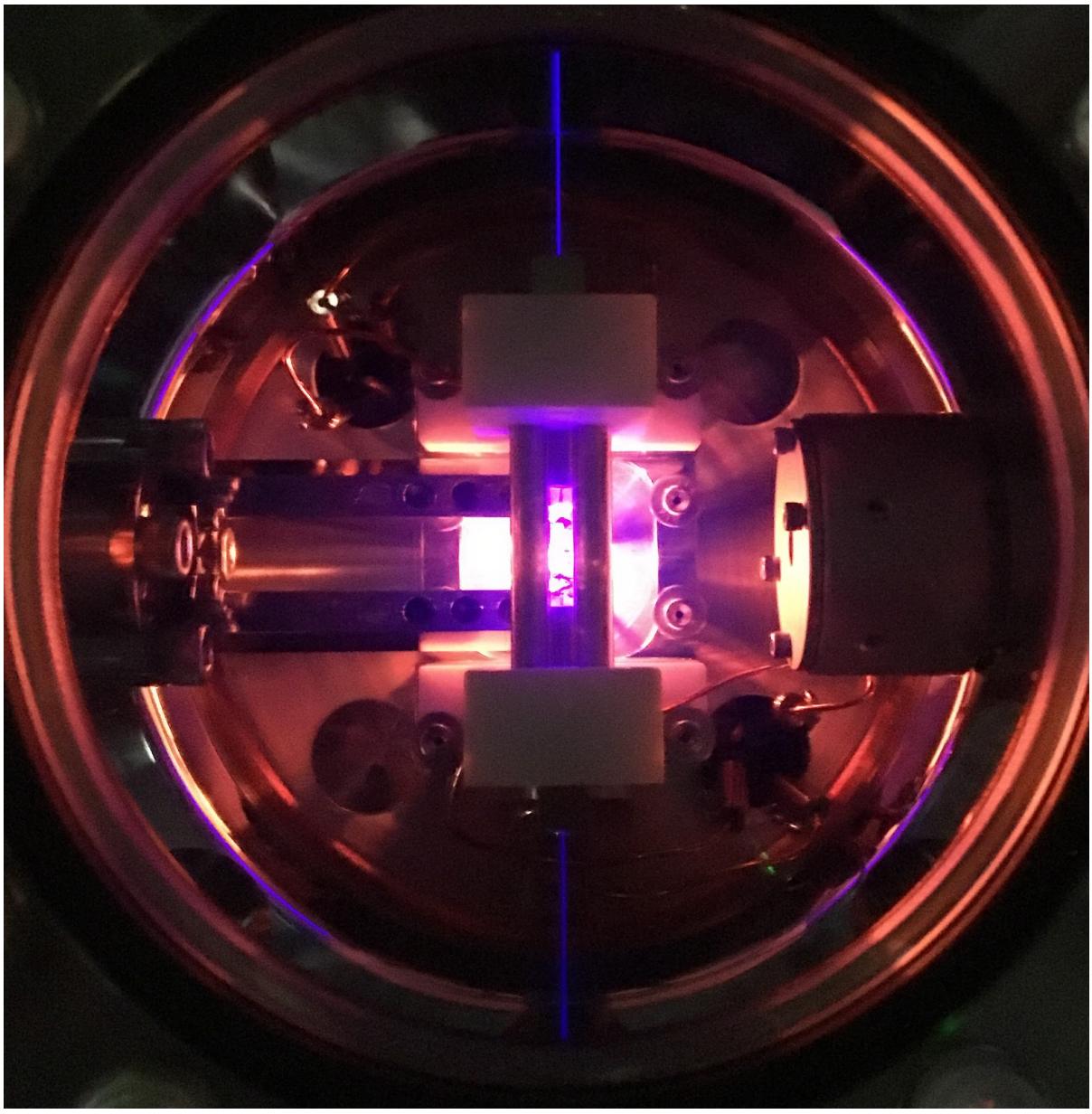

Figure 5.4: Picture of the Enterprise ion trap with atomic sources. The ablation target (left) and oven (center, glowing), and TOFMS (right) are shown. Strontium atom fluorescence (blue) can be observed.

Chapter 6

Experimental Control

This chapter highlights several key pieces of experimental control that exist outside of the vacuum system.

6.1 Lasers

Lasers are an essential component of an ion trapping experiment. Work with two different ion species requires several lasers, but because the strontium and radium ion wavelengths are all far from the UV they can be accessed with direct diode lasers. We list out the strontium and radium ion laser sources in the following subsections.

6.1.1 Sr^+

1. 422 nm: A Moglabs (diode: NDVA416T, BA5949-2) Littrow laser is used to drive the $S_{1/2} \rightarrow P_{1/2}$ Doppler cooling transition.

2. 1092 nm: A Photodigm distributed Bragg reflector laser is used to drive the $D_{3/2} \rightarrow P_{1/2}$ repump transition.

3. 674 nm: A Moglabs (diode: RWE870, AH-59404) and Toptica DL PRO (diode: LD-0670-0035-AR-6) extended cavity diode laser are used to drive the $S_{1/2} \rightarrow D_{5/2}$ clock/qubit transition.

4. 1033 nm: A Moglabs (diode: RWE1060, EG-07331) cateye laser is used to drive the $D_{5/2} \rightarrow P_{3/2}$ cleanout transition.

5. 405 nm: A D405-120 diode is mounted to a 5.6 mm TEC TO-Can Arroyo Instruments laser mount to excited neutral strontium to the continuum.

6. 461 nm: A Moglabs (diode: NDB4916T, BA6541-03) cateye laser is used to drive the ${}^1S_0 \rightarrow {}^1P_1$ transition in neutral strontium.

6.1.2 Ra^+

1. 468 nm: A Moglabs (diode: 468LD100) Littrow laser is used to drive the $S_{1/2} \rightarrow P_{1/2}$ Doppler cooling transition.

2. 1079 nm: A Photodigm distributed Bragg reflector laser is used to drive the $D_{3/2} \rightarrow P_{1/2}$ repump transition.

3. 728 nm: A Moglabs (diode: RWE-0740) cateye laser is used to drive the $S_{1/2} \rightarrow D_{5/2}$ clock/qubit transition.

4. 802 nm: A homebuilt (diode: EYP-RWE-0810-03010-1300-SOT02-0000) external cavity diode laser is used to drive the $D_{5/2} \rightarrow P_{3/2}$ cleanout transition.

5. 532 nm: A Continuum Minilite is used for laser ablation of the $RaCl_2$ target. Though the Q switched laser can operate at other wavelengths (1064, 355, and 266 nm), 532 nm light is used to make alignment process easier. The Minilite can output a ≈ 32 mJ pulse at max power.

6. 450 nm: A PLT5450B diode is mounted to a 5.6 mm TEC TO-Can Arroyo Instruments laser mount to excited neutral radium to the continuum.

7. 483 nm: A Moglabs (diode: 488lD200) Littrow laser is used to drive the $^1S_0 \rightarrow ^1 P_1$ transition in neutral radium.

6.2 Laser Frequency Modulation

Laser frequency modulation is a critical part of any experiment, not only for shifting the frequency of light addressing the ion, but also for stabilizing laser frequencies to optical cavities. Acousto-optic modulators (AOMs) diffract and shift the frequency of light using sound waves, while electro-optic modulators (EOMs) use electric fields to generate frequency sidebands. AOMs also enable fast shuttering of the light amplitude at the ion. Light that addresses transitions is first double-passed through an AOM so that the increased diffraction angle does not alter the fiber coupling efficiency to the trap [47]. We typically use AOMs that are optimized for high-bandwidth efficiency. This eliminates the need to calibrate the AOM driving power across a wide range of frequencies. For light addressing the ion that requires large frequency shifts a fiber EOM is used. For the clock laser cavity a Thorlabs free-space EOM is used to generate sidebands. For other low finesse cavities we use a homemade EOM design, the instructions for which can be found on GitHub.

6.3 Optical Cavities and Laser Locks

Optical cavities, which consist of two high-reflectivity mirrors attached to either end of a material that has a low thermal coefficient of expansion, are an essential part of precision measurement experiments. In combination with the Pound-Drever-Hall (PDH)

lock [48] optical cavities enable frequency stabilization of a laser. This is accomplished by locking to the derivative of the reflected intensity of the cavity, which will be asymmetric around the cavity resonance. These resonances will be spaced depending on the free spectral range of the cavity $c/2L$ where c is the speed of light and L is the length of the cavity. Cavities used in our experiments are 10 cm long which provides a 1.5 GHz spacing between modes.

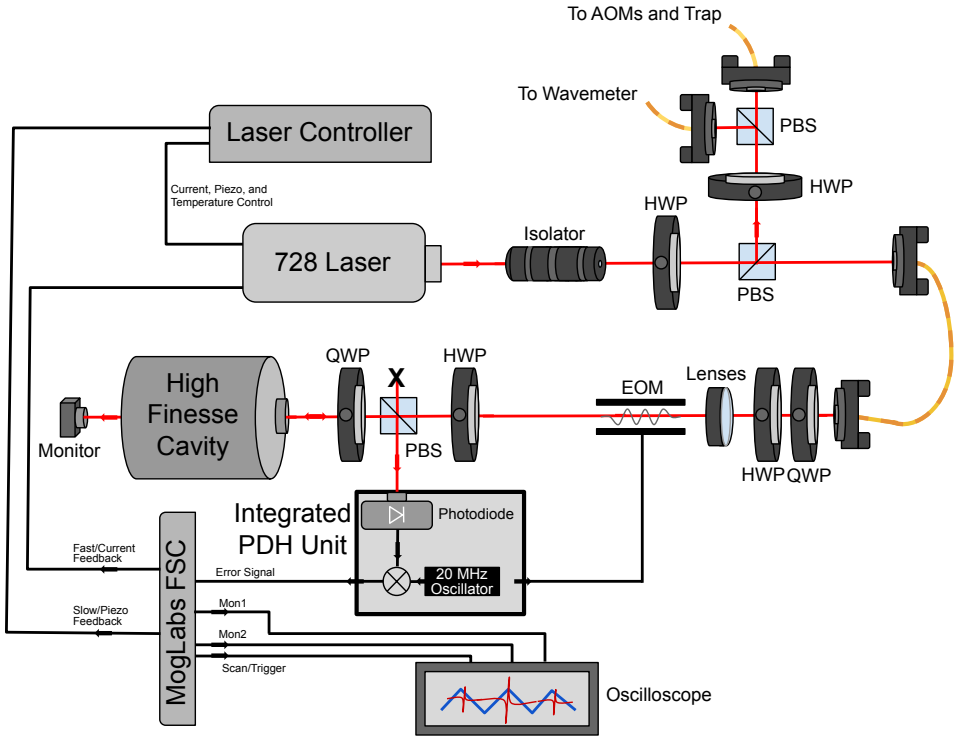

Figure 6.1: Diagram of the 728 nm laser and locking electronics.

For clock laser locks we use high-finesse ultra-low expansion glass cavities from Stable Laser Systems that have a quoted finesse of 100,000-200,000. The integrated PDH detector is also from Stable Laser Systems (PDH-100-SE), and is used to produce an error signal that is sent to the laser and laser controller, see Fig. 6.1. The integrated PDH unit drives the EOM that produces sidebands for laser locking. Polarization optics are placed before the EOM to minimize residual amplitude modulation that leads to noise

and instability in the lock. The error signal generated from the unit is sent to a Moglabs fast servo controller where the locking parameters can be controlled. Feedback is then sent to the laser head and laser controller. A camera on the back of the cavity is used for initial alignment and observation of the optical mode.

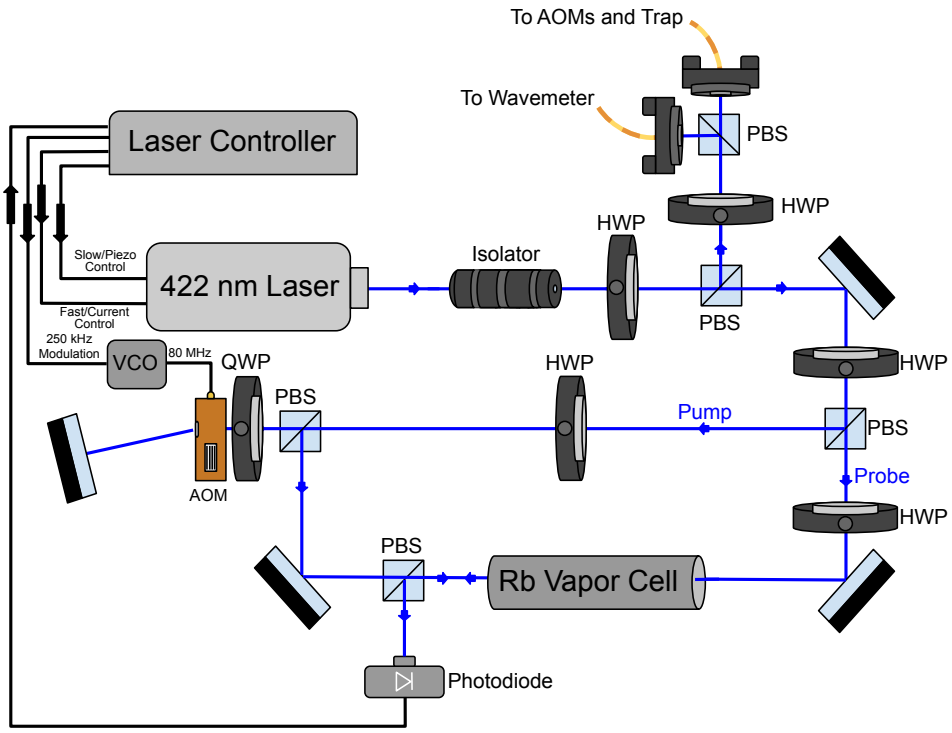

Figure 6.2: Diagram of the 422 nm laser and rubidium saturated absorption lock.

For locking lasers that drive dipole transitions our group uses two different "quad" cavities that each have four bores drilled into the glass. The first is homemade and follows the Innsbruck design [49]. The second is a commercial system from Stable Laser Systems. Both quad cavities have piezoelectric rings on all four sets of cavity mirrors. These rings enable the cavity length to be adjusted such that the locking frequency can be optimized for a minimal amount of AOMs to address the ions. The locking setup for these lasers is similar to that of the 674 nm and 728 nm radium and strontium clock lasers with the exception that an integrated PDH unit is not used and homemade EOMs

replace the Thorlabs free-space EOM.

The strontium Doppler cooling laser at 422 nm can be stabilized to a heated rubidium vapor cell, see Fig. 6.2. Rubidium has several transitions that are fortuitously near the $S_{1/2} \rightarrow P_{1/2}$ transition in Sr^+. We lock to the rubidium $5s^2S_{1/2}(F'' = 2) \rightarrow 6p^2P_{1/2}(F'' = 2, 3)$ transition by means of saturated absorption spectroscopy, where the frequency detuned "pump" and "probe" beams are counter propagated in the cell to produce a lockable signal [50].

6.4 RF Drive and DC Voltage Control

For the initial trapping and laser cooling of radium ions we used the UCLA MOTion electronics system [51]. This fully integrated system was designed for the precision timing and control needed for work with the TOFMS described in Chapter 5. After the initial trapping of radium ions which is describe in Chapter 7 we switched to a design that used a single rf drive input to better minimize the phase mismatch between the rf rods. We continued using one of the rf drive units and the dc voltage controllers from the MOTion electronics system due to their exceptionally low noise. An Eagle schematic of our trap drive unit that we switched to is shown in Fig. 6.3, and a picture of the assembled unit is shown in Fig. 6.4. For the resonator toroid an iron core (T200-2) is wrapped with 22 awg motor wire. For the endcap voltage control supply an iseg (SHQ 222M) power supply is used.

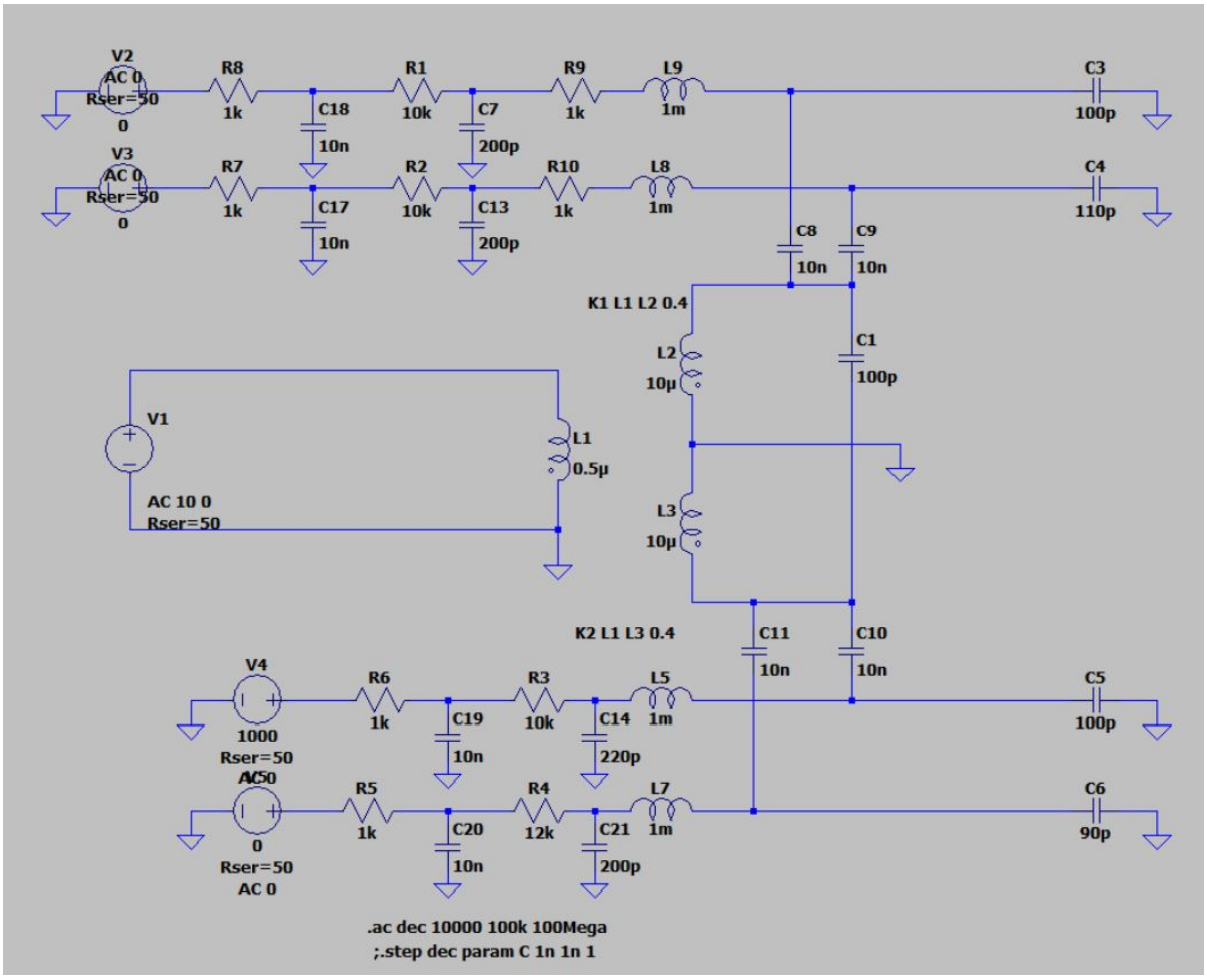

Figure 6.3: Eagle schematic of the printed circuit board for the Enterprise trap drive unit.

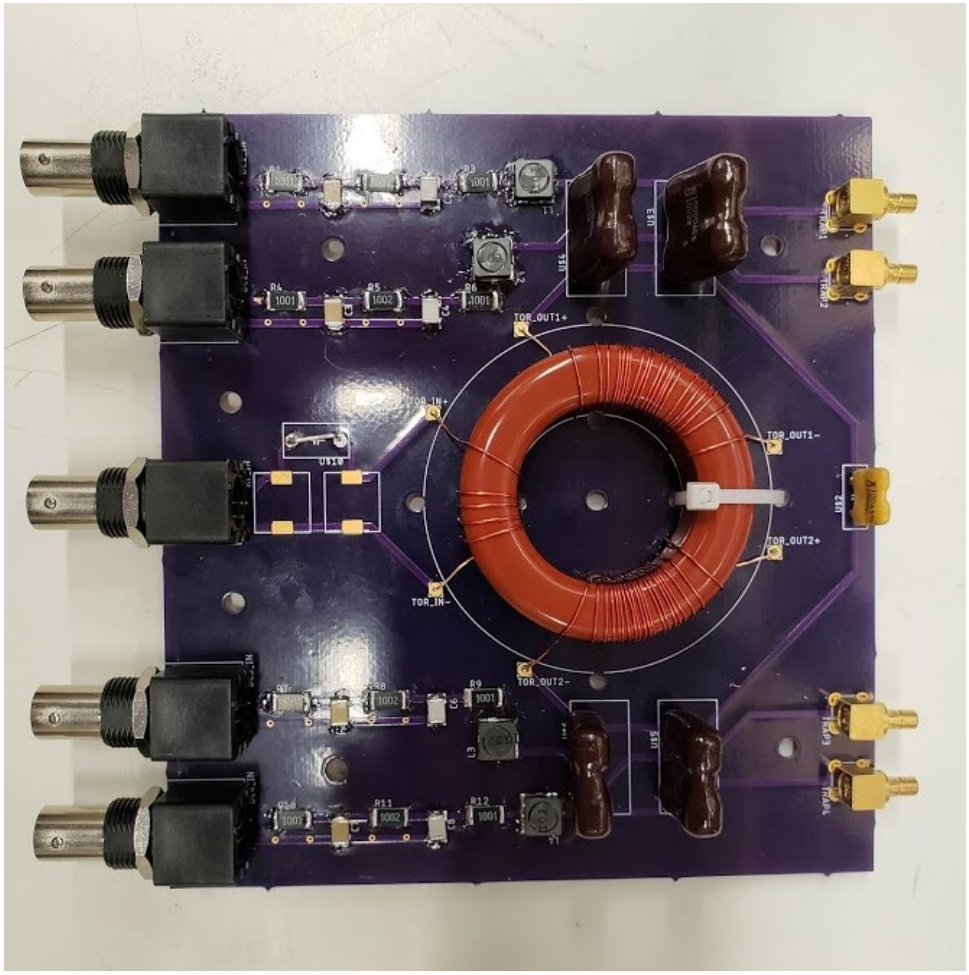

Figure 6.4: Picture of the assembled and soldered Enterprise trap drive unit.

6.5 Imaging

The imaging system, which consists of the objective lens system, camera, and photomultiplier tube, collects and counts photons scattered from the ion. We describe these components in the following subsections.

6.5.1 Objective

The objective lens system design first originated at the Universität Bonn [52], and was later used by several AMO group [53, 54, 55, 56]. The systems uses four lenses: a positive meniscus lens (LE1418-A - Thorlabs), a plano-convex lens (LA1979-A - Thorlabs), a bi-convex lens (LB1199-A - Thorlabs), and a plano-concave lens (KPC070AR.14 - Newport), where the parts listed in parenthesis are the parts picked specifically for our system. The four lens design provides an inexpensive alternative to a commercial system. Our system is optimized to collect 422 nm and 468 nm photons with a working distance of ~ 60 mm and a field of view of ~ 500 μm. We find the numerical aperture to be ~ 0.3. Semrock single-band bandpass filters are interchangeably used when working with strontium and radium ions to minimize background counts from the system.

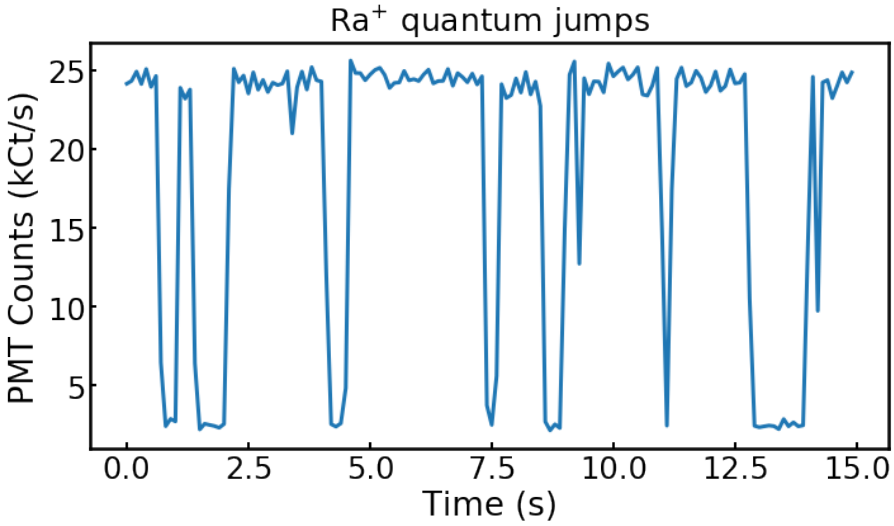

Figure 6.5: PMT counts from a single $^{226}Ra^{+}$ ion. When the 728 nm light is on resonance with the $S_{1/2} \rightarrow D_{5/2}$ transition a quantum jump will occur. This cause sharp drops and rises in the total PMT counts.

6.5.2 Photomultiplier Tube

A photomultiplier tube is a device that converts light into an electrical signal by making use of the photoelectric effect. They are particularly suited for applications that require high response speeds and sensitivity, such as work with single ions. We use the Hamamatsu PMT H10682-210, which has an output pulse width of 10 ns and average dark count rate of 50 Hz. We calculate a collection efficiency, the average percent of scattered photons from the ion that are collected with the PMT, of 0.28%. A sample of PMT counts is shown in Fig. 6.5, where high counts $\sim$ 25 kCt/s indicate the ion is being laser cooled, and low counts $\sim$ 2 kCt/s indicate that we have driven a quantum jump with clock laser and the valence electron is in the $D_{5/2}$ metastable state.

6.5.3 Camera

We use an Andor iXon Ultra 897 electron multiplying CCD camera for imaging strontium and radium ions. The camera is very helpful for initial alignment of the imaging and laser systems when the PMT counts have not yet been optimized. A composite image of co-trapped strontium and radium ions taken on the iXon Ultra are shown in Fig. 6.6. We have also found the Thorlabs Quantalux camera to be reasonably sufficient for imaging single ions after the laser alignment and PMT counts have been optimized.

6.6 Measurement System

Photon counts collected from the PMT are sent to an integrated direct digital synthesizer and field programmable gate array control and measurements system that coverts the 10 ns PMT pulses to time-tagged photons. [57]. This system also manages the experimental sequences for measurements with the ion, controlling the AOM driving frequencies

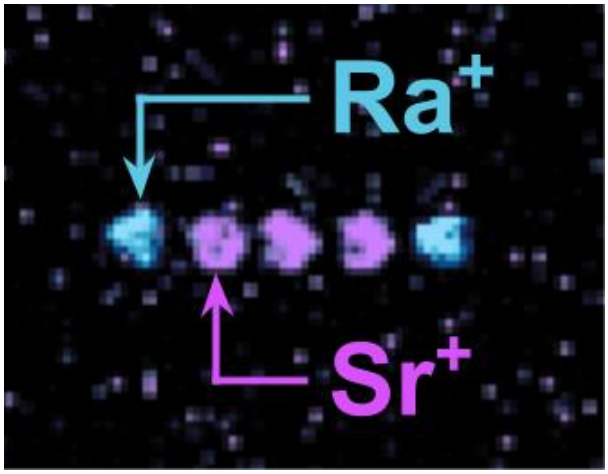

Figure 6.6: A composite image of co-trapped Sr^+ (3 ions, purple) and Ra^+ (2 ions, teal).

and amplitude for all lasers. Transistor-transistor logic channels are used to control the ablation laser and the mechanical shutters that block the light used for photoionization.

6.7 Magnetic Field

To prevent coherent dark states [11], a number of connected NdFeB ring magnets (1"OD x 1.2"ID x 1/4", grade N52) are used to produce a magnetic field at the ion. These magnets are held in a lens tube and mounted onto a Thorlabs dovetail optical rail for easy adjustment of the magnetic field. We typically place the ring magnets at a distance that will produce a magnetic field of 3-6 G at the ion.

Chapter 7

Laser Cooling and Trapping of Radium Ions

This chapter includes the contents of our work, *Laser Cooling of Radium Ions* [5], and additional information on calibration of the time-of-flight mass spectrometer that was instrumental in obtaining the first radium ion signal.

7.1 Laser Cooling of Radium Ions

The unstable radium nucleus is appealing for probing new physics due to its high mass, octupole deformation and energy level structure. Ion traps, with long hold times and low particle numbers, are excellent for work with radioactive species, such as radium and radium-based molecular ions, where low activity, and hence low total numbers, is desirable. We address the challenges associated with the lack of stable isotopes in a tabletop experiment with a low-activity (~ 10 μCi) source where we laser-cool trapped radium ions. With a laser-cooled radium ion we measured the $7p\ ^2P^o_{1/2}$ state's branching fractions to the ground state, $7s\ ^2S_{1/2}$, and a metastable excited state, $6d\ ^2D_{3/2}$, to be

$p = 0.9104(7)$ and $0.0896(7)$, respectively [5]. With a nearby tellurium reference line we measured the $7s\ ^2S_{1/2} \rightarrow 7p\ ^2P^o_{1/2}$ transition frequency, 640.096 63(6) THz [5].

Radium, the heaviest alkaline earth element, has no stable isotopes. Singly ionized radium's simple electronic structure is amenable to optical pumping and laser cooling with wavelengths far from the challenging UV of most alkaline earth type ions. Radium's heavy nucleus, atomic number $Z = 88$, is well suited to searches for new physics, where sensitivity to symmetry breaking forces scales as $\propto Z^3$ [58, 59]. Certain radium isotopes, such as radium-225, have additional nuclear structure enhancements to CP (charge-parity) violating new physics [60, 61]. Setting limits to sources of CP violation will help us understand the baryon asymmetry in the observed Universe [62].

Pioneering work with trapped HfF^+ molecular ions has made significant progress in constraining leptonic CP violation, and has rigorously studied potential systematic effects for future experiments [63]. A complementary hadronic CP violation experiment with radioactive molecular ions $RaOH^+$ or $RaCOH_3^+$ [30] is an intriguing possibility, where the low densities and long hold times of ion traps are well matched to working with radioactive isotopes, because low total activity is desirable. The radium-225 nucleus ($I = 1/2$) has octupole deformed parity doublets that enhance sensitivity to CP violating forces by a factor of 100-1000 compared to the current touchstone atomic system, ^{199}Hg [64, 29, 65]. A radium-based molecular ion, such as $^{225}RaOH^+$, has an additional sensitivity advantage because of the molecule's closely spaced, opposite parity electronic states in addition to the enhancements from the closely spaced, opposite parity radium nuclear states. Trapped and laser-cooled radium ions could be the starting point for generating such radium-based molecular ions, where optical pumping Ra^+ may provide control of chemical reactions to produce $RaOH^+$, as seen in other alkaline earth ions Ca^+ and Be^+ [66, 67].

For quantum simulation with trapped ions, qubit states protected from environmental noise with long lifetimes are favorable. A spin-1/2 nucleus with a single electron atom,

such as in $^{171}Yb^{+}$, $^{133}Ba^{+}$ [45], or $^{225}Ra^{+}$, provides such levels that are first-order insensitive to magnetic fields. The qubit state is typically read out through optical cycling, with readout fidelity limited by the $P_{1/2}$ state's hyperfine splitting (2.1 GHz in $^{171}Yb^{+}$). Though a massive nucleus is at odds with high secular frequencies, it is desirable for its large hyperfine interactions, as off-resonant pumping during qubit readout decreases quadratically with hyperfine splitting. The $P_{1/2}$ hyperfine splitting of $^{225}Ra^{+}$ is 5.4 GHz [36], which suppresses the qubit readout error by a factor of ~ 8 compared to $^{171}Yb^{+}$ [68]. Radium also has favorable transitions where abundant optical power and photonic technology are available, see Fig. 7.1 (b). The radium ion supports optical qubits on the $S_{1/2} \rightarrow D_{5/2}$ transition. The $D_{5/2}$ state of $^{225}Ra^{+}$, like the ground state, has 2 hyperfine "clock" states, which, when combined with the ground state qubit levels, offers the possibility to simulate spin-1 or spin-3/2 physics with four magnetic field insensitive states [69].

In this work we trap and laser cool $^{226}Ra^{+}$ ($I = 0$) to form Coulomb crystals, as seen in Fig. 7.1 (a). We used the crystallized radium ions to measure the $7p\ ^2P^o_{1/2}$ state's branching fractions to the $7s\ ^2S_{1/2}$ and $6d\ ^2D_{3/2}$ states, a necessary measurement to determine dipole matrix elements for the respective transitions. Our measurement at 2 digits of precision is sufficient to support optical pumping or basic simulations with optical Bloch equations, but we extended the measurement to higher precision to support PNC measurements in Ra^{+} at the 0.8% level [70, 71]. We also measure the $7s\ ^2S_{1/2} \rightarrow 7p\ ^2P^o_{1/2}$ transition frequency with respect to a Te_2 molecular absorption line, which establishes a convenient frequency reference for the radium-226 ion's most important transition [42].

In previous work at a nuclear facility singly ionized radium isotopes 209 through 214 were produced and trapped [72, 73]. We apply a different technique to trap radium-226. The radium is ionized and loaded into the trap by ablation with a 532 nm $\sim$ 10 mJ pulse from a Nd:YAG laser with 0.5(1) mm $1/e$ intensity diameter. The ion trap's rf

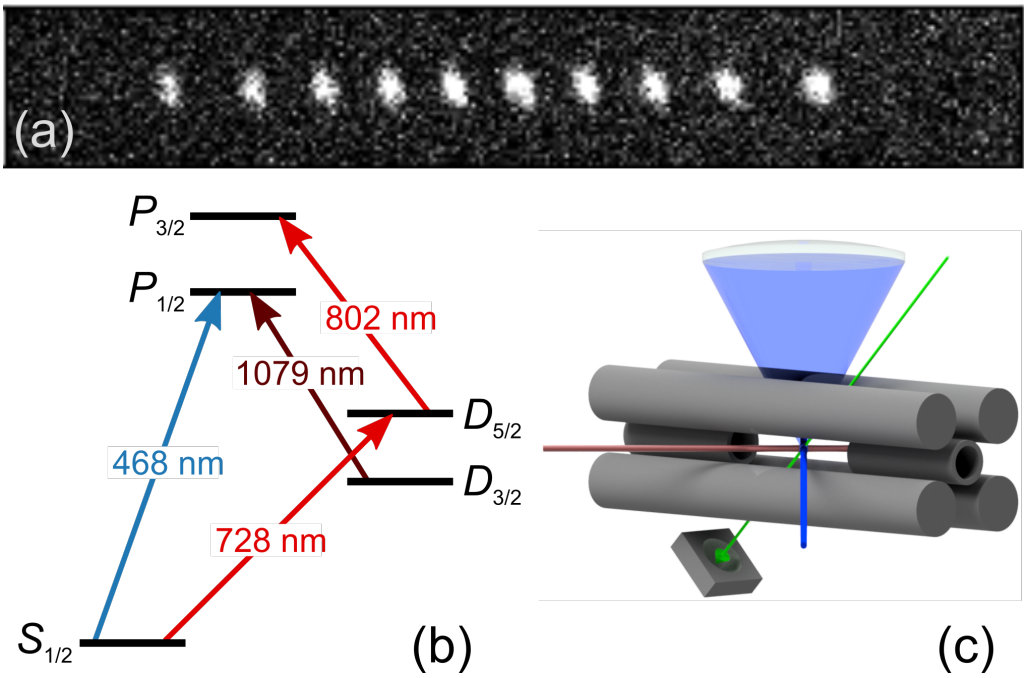

Figure 7.1: A Coulomb crystal of 10 trapped radium-226 ions (a) that were loaded into the trap via laser ablation and laser cooled with a combination of 468 nm and 1079 nm radiation. The relevant level structure of Ra^+ for the laser cooling and measurements done in this work [5] are shown in (b), in addition to the transitions necessary for controlling the ion via the narrow $^2S_{1/2} \rightarrow {}^2D_{5/2}$ quadrupole transition at 728 nm and the $^2D_{5/2} \rightarrow {}^2P^o_{3/2}$ dipole transition at 802 nm. In (c) the ion trap is depicted with the radium ablation target and the ablation laser (green), the 468 nm cooling light (blue), and the 1079 nm repump light (red). The diagonal rf electrodes are separated by 6 mm and the end cap electrodes by 15 mm. The rf trapping frequency is 2.1 MHz.

trapping voltage is switched on 20 μs after the ablation pulse to enhance radium ion loading efficiency [51]. The radium was received as $^{226}RaCl_2$ in 5 mL 0.1 M HCl solution with an activity of 10(2) μCi, which corresponds to $\sim 3 \times 10^{16}$ radium-226 atoms. We made a laser ablation target by drying the radium solution on a 316 stainless steel mount which was installed in the vacuum system on a translation stage to position the target $\sim$ 15 mm from the trap center, see Fig. 7.1 (c).

The radium ion fluoresces when near resonant light addresses the $S_{1/2} \rightarrow P_{1/2}$ transition at 468 nm and the $D_{3/2} \rightarrow P_{1/2}$ transition at 1079 nm, see Fig. 7.1 (b). The ion is

laser cooled when the 468 nm laser is red detuned from the $S_{1/2} \rightarrow P_{1/2}$ transition. Electronic branching from the $P_{1/2}$ state populates the $D_{3/2}$ state, which the 1079 nm light repumps back into the fluorescence cycle. To prevent coherent dark states a magnetic field of a few gauss is applied [11].

The signals for our measurements are the 468 nm photons spontaneously emitted by radium ions. These photons are focused onto a photomultipler tube (PMT), Hamamatsu H10682-210, whose output is sent to an integrated direct digital synthesizer and field-programmable gate array control and measurement system that can convert the PMT pulses to time-tagged photons [57]. The same system synchronously controls the measurement sequences by driving acousto-optic modulators (AOMs) which set the amplitude and frequency offsets for the 468 and 1079 nm lasers. The AOM extinction ratios are $\geq$ 60 dB. Measurement sequences, based on the techniques developed by Ramm *et al.* [74] and Pruttivarasin *et al.* [75], eliminate challenging systematics, such as AC Stark shifts, by addressing only one transition at a time.

The branching fraction measurement sequence is summarized in Fig. 7.2. Before each measurement, we Doppler cool the radium ion for 100 μs and then optically pump population into the $S_{1/2}$ state by applying 1079 nm light for 20 μs. After cooling and state preparation the electronic population is optically pumped to the $D_{3/2}$ state and collected 468 nm photons are time tagged, N_b^F. The background scattered 468 nm light is then measured, N_b^B, while the ion is shelved in the $D_{3/2}$ state. The population is then pumped back to the $S_{1/2}$ ground state with 1079 nm light, and if the single emitted 468 nm photon is collected it is time tagged, N_r^F, and a corresponding background, N_r^B, is recorded. We subtract the respective backgrounds to determine the number of collected photons emitted by the radium ion, N_b and N_r. From these counts we calculate the branching fraction to the ground state, $p = [N_b/(N_b + N_r)]$ [74]. The measurement is repeated 11.5×10^6 times in approximately one hour with a single radium ion. The raw

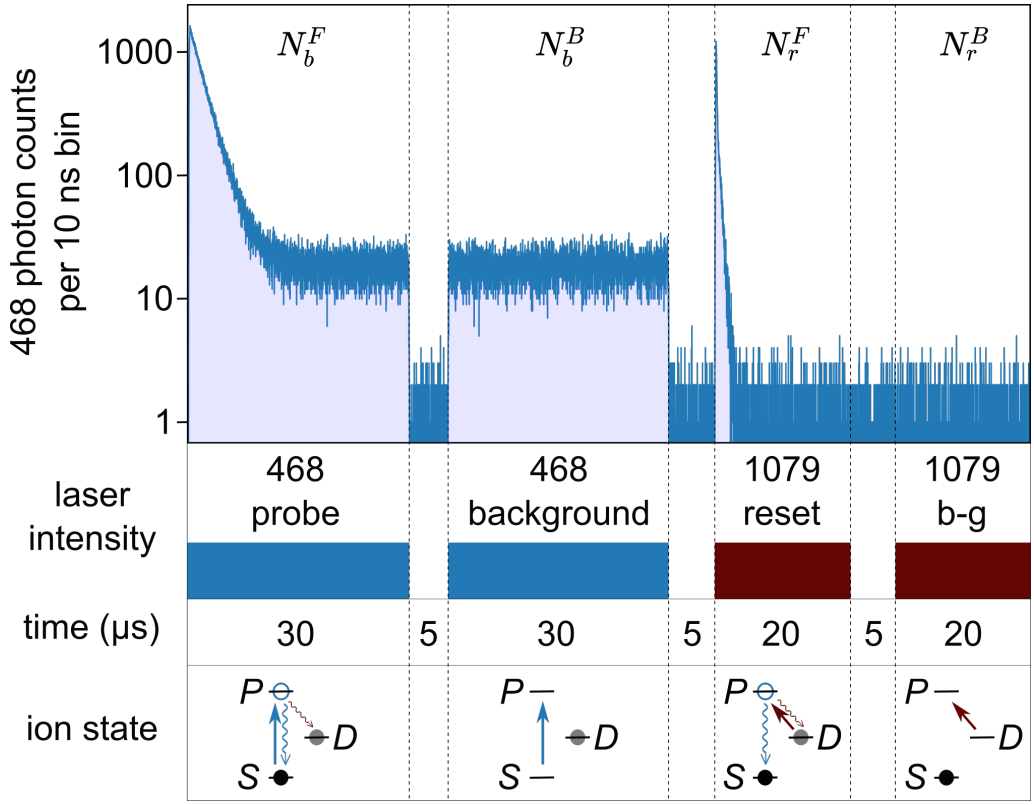

Figure 7.2: The total PMT counts during the $P_{1/2}$ branching fraction measurement are shown, along with the corresponding laser pulses and the measurement timing sequence. The bottom panel shows the electronic population, applied optical fields, and expected decays.

photon counting results are $N_b^F = 359\,583$, $N_b^B = 55\,297$, $N_r^F = 31\,386$, and $N_r^B = 1443$, which yields a statistical branching fraction of $p = 0.9104(5)$. The N_r counts are also used to measure the imaging system detection efficiency (0.26%).

The largest systematic uncertainty in the branching fraction measurement comes from residual birefringence of the imaging system and the Hanle effect. If the 468 and 1079 nm lasers are perfectly linearly polarized, the Hanle effect is not present, and an equal number of right- and left-handed circularly polarized photons will be collected [76]. However, if either laser beam has a circularly polarized component, then there will be an imbalance in the right- and left-handed circularly polarized photons collected. The imbalance will depend on the direction and magnitude of the applied magnetic field

which sets the quantization axis. Residual birefringence of the imaging system may result in different detection efficiencies for the two circular polarizations, which in turn will shift the branching fraction measurement. The applied magnetic field is parallel to the 1079 nm laser, and both 1079 and 468 nm lasers are linearly polarized to suppress the Hanle effect. We set a limit on the uncertainty due to residual birefringence and the Hanle effect by reversing the applied magnetic field. The field reversal will flip the imbalance between right- and left-handed circularly polarized photons collected [77], giving a different value for the branching fraction [74, 78]. The measured branching fraction with the field reversed, $p = 0.9107(5)$, agrees with the original field configuration. Therefore, uncertainty due to the combined effects of residual birefringence and the Hanle effect is at the level of the statistical uncertainty.

The systematic uncertainties and shifts due to other sources we considered are significantly less than those due to residual birefringence. For shifts due to collisions we considered worst case scenarios. For example, after shelving to the $D_{3/2}$ state, a collision could put the ion in an orbit that is dark to the 1079 nm pump pulse, and then a second collision could return the ion to the trap center where it emits a 468 nm photon during the 1079 nm background pulse. From our measurements we estimate the average collision rate to be less than 0.32 collision per second. PMT dead time (20 ns) results in both systematic error and shift. We evaluate systematic shifts due to the finite lifetime of the $D_{3/2}$ state, the finite measurement time, and the finite extinction ratio of the AOMs using optical Bloch equations that describe the three-level system [74]. To solve the Bloch equations we use Rabi frequencies determined from fitting the spontaneous decays in N_b^F and N_r^F, a theoretical $D_{3/2}$ state lifetime of 638(10) ms [79], and the $P_{1/2}$ branching fraction, $p = 0.9104$, from our statistical results. More details are included in the Supplemental Material [78].

The uncertainties and shifts for the branching fraction measurement are summarized

Table 7.1: Uncertainties and shifts for the $P_{1/2}$ branching measurement.

Source	Shift	Uncertainty
Statistical	...	5×10^{-4}
Birefringence	...	5×10^{-4}
Collisions	...	$< 4 \times 10^{-5}$
PMT dead time	3×10^{-6}	3×10^{-6}
$D_{3/2}$ state lifetime	2×10^{-7}	2×10^{-8}
Measurement time	5×10^{-9}	3×10^{-7}
AOM extinction ratio	...	5×10^{-7}
Total	3×10^{-6}	7×10^{-4}

in Table 7.1. When we add the uncertainties in quadrature the branching fraction to the ground state is $p = 0.9104(7)$, where systematic shifts do not contribute as their sum is far below the measurement uncertainty. The measurement verifies theoretical techniques applied to this multielectron system that previously gave the only knowledge of the branching fraction [79, 80, 81], see Fig. 7.3. The measurement can also be expressed as a ratio of the reduced dipole matrix elements between the $S_{1/2} \rightarrow P_{1/2}$ and $D_{3/2} \rightarrow P_{1/2}$ transitions, $m_{SP}/m_{PD} = 0.912(4)$.

The $S_{1/2} \rightarrow P_{1/2}$ transition of Ra^+ is crucial to laser cooling and state detection. We measure this transition's linewidth and center frequency with a linescan measurement [75]. From the linewidth we infer a lower limit on the $P_{1/2}$ state's lifetime of 7.3(1) ns, consistent with the theoretical value of 8.57(10) ns [80]. With tellurium vapor cell spectroscopy we determine the $^{226}Ra^+$ $7s\ ^2S_{1/2} \rightarrow 7p\ ^2P^o_{1/2}$ transition frequency to be 640.096 63(6) THz. Our measurement agrees with a transition frequency of 640.096 647(23) THz, which was inferred from a measurement of this transition in $^{214}Ra^+$ anchored to tellurium line 178 [73], and separate Ra^+ isotope shift measurements at the CERN ISOLDE facility [36].

For the Ra^+ linescan we trap and laser cool a chain of four radium ions. In the measurement sequence the ions are excited by a 468 nm laser probe pulse (2 μs), and then

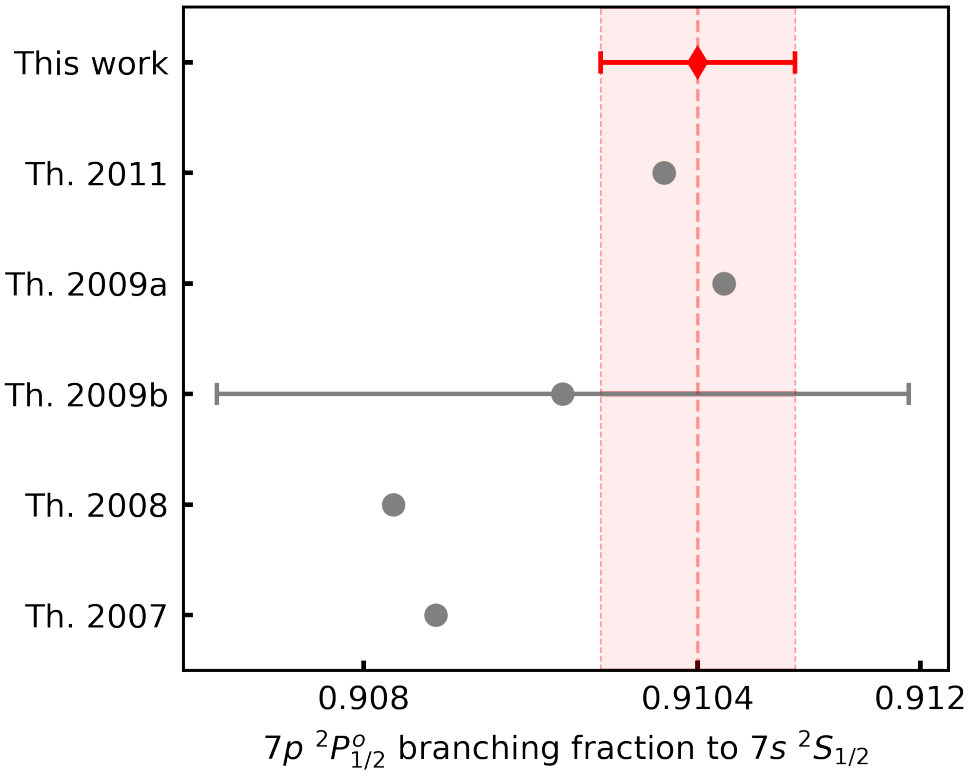

Figure 7.3: The measured branching fraction of the $^{226}Ra^+$ $P_{1/2}$ to the $S_{1/2}$ (diamond), $p = 0.9104(7)$, compared to previous theoretical values (circles) where error bars are included when uncertainty is available. The theoretical branching ratios are determined from reduced dipole matrix elements in the corresponding references: Th. 2011 [81], Th. 2009a [79], Th. 2009b [80], Th. 2008 [82], Th. 2007 [37] .

reset back to the ground state by a 1079 nm pulse (10 μs). The pulse sequence is repeated for different detunings, and before every ten sequences the ions are Doppler cooled for 500 μs and optically pumped to the electronic ground state. We run the pulse sequence 2×10^5 times at each of 56 detunings set by an AOM with randomized measurement ordering. The 468 nm laser is Pound-Drever-Hall locked to a Corning Ultra-Low Expansion (ULE) glass cavity sealed in a vacuum chamber with multiple layers of acoustic, seismic, and thermal isolation with active temperature stabilization [49]. In order to determine the transition frequency by a comparison with tellurium spectroscopy, the stabilized laser frequency during the measurement is recorded with a wave meter. The photon counts

for the measurement are plotted in Fig 7.4.

The nearest measured $^{130}Te_2$ line to the radium transition is line 176 at 640.098 99(5) THz [42]. We measure the line in a 10 cm long tellurium vapor cell at 550°C by scanning a laser while recording the absorption on a photodetector and the frequency with a wave meter (High Finesse WS-8), see Fig. 7.4 (b). The line center is determined with a Gaussian fit and is then compared to the recorded frequency of the radium linescan to determine its detuning, -2.36 GHz. The largest uncertainty in the frequency measurement is the 50 MHz uncertainty in the Te_2 line [42]. There is a 10 MHz uncertainty contribution due to the wavemeter, which is determined with multiple linescans of the radium ion's $S_{1/2} \rightarrow P_{1/2}$ transition, and an additional 10 MHz uncertainty in the measured Te_2 transition's center frequency.

We fit the photon counts of the Ra^+ linescan to a Lorentzian and get a linewidth of 21.7(4) MHz, see Fig. 7.4 (a). The largest broadening contribution is likely micromotion Doppler broadening [8], which we estimate broadens the line by ~ 2.1 MHz [78].

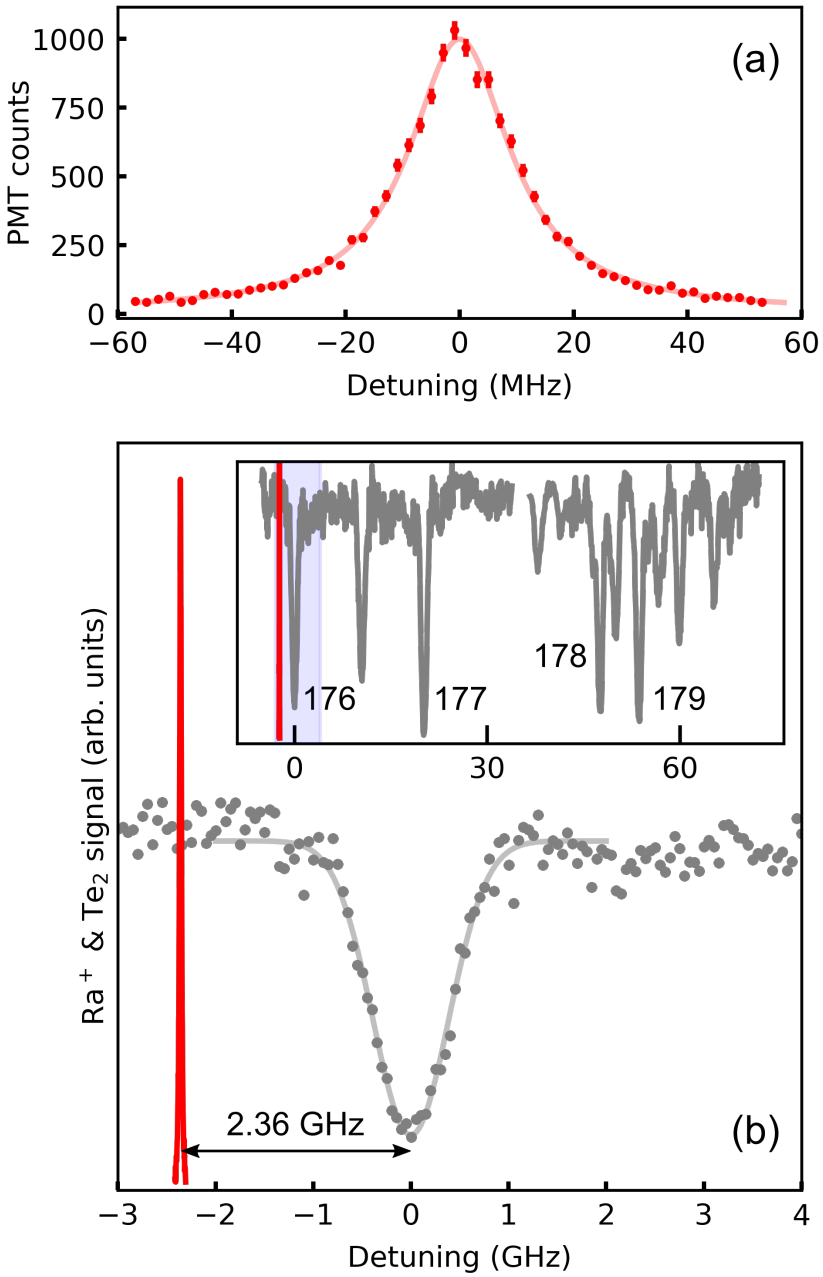

Figure 7.4: Collected photons from the Ra^+ linescan measurement with a Lorentzian fit (a). The tellurium absorption spectrum is plotted with the Ra^+ linescan (b), where the tellurium data (grey) and Ra^+ data (red) are scaled and offset to highlight the detuning between the transitions. The inset of (b) shows tellurium lines in the vicinity of the Ra^+ transition labelled with their atlas numbers, and the frequency span of the outset region highlighted in blue.

In this work we laser cooled trapped Ra^+, an element where the most stable isotope, radium-226, has a 1600 year half-life, in a tabletop experiment (< 4 L vacuum volume). Laser cooling the trapped radium ions helped keep the ions well localized in the trap for > 12 h at a time, enabling a precision measurement of the $P_{1/2}$ state's branching fraction.

This work opens the door to research with laser-cooled radium ions, including isotopes such as radium-225. The low charge-to-mass ratio of Ra^+ is well suited to sympathetic cooling of heavy atoms and large molecular ions. Cold Ra^+ could be used to make molecular ions such as $RaOH^+$, and to sympathetically cool their motion and control their internal states with quantum logic spectroscopy [83].

7.2 Time-of-flight Mass Spectrometer Calibration

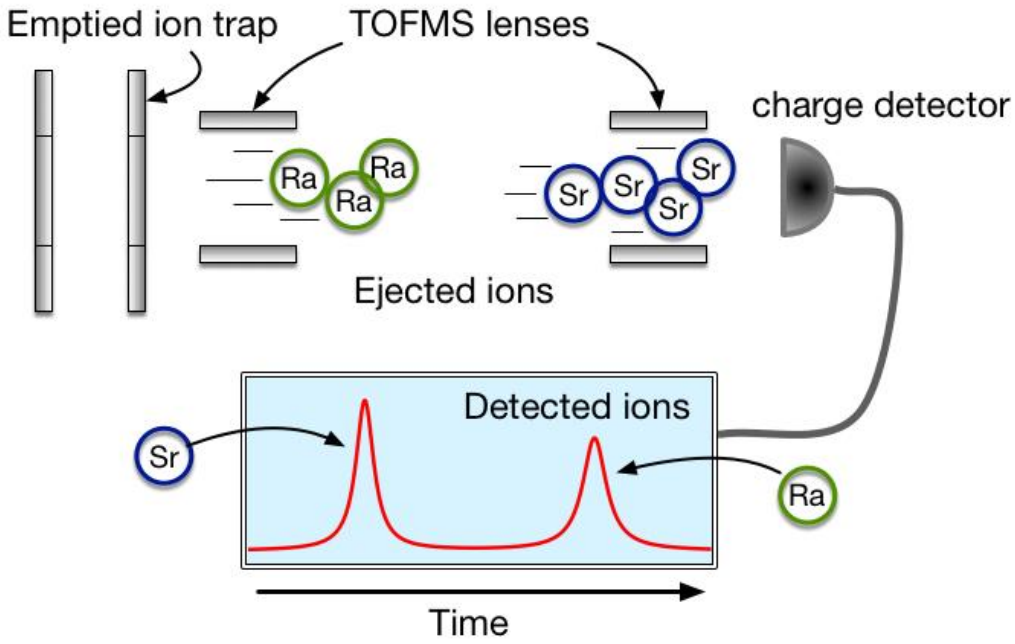

Figure 7.5: Ions are ejected from the ion trap by applying a high voltage on the rods further from the charge detector. TOFMS Einzel lenses focus the ions towards a charge detector. We can resolve a mass difference between different ions from the time delay between observed events. Strontium ions, which are lighter in mass compared to radium, will strike the detector first, followed by radium ions.

Testing and calibration of the TOFMS was important for the first laser cooling and trapping of radium ions. Before searching for the radium ion fluorescence, we first confirmed that all rod pulse timings were correct by monitoring the pickup signal on an oscilloscope. To ensure that the TOFM was working, we loaded large clouds of stron-

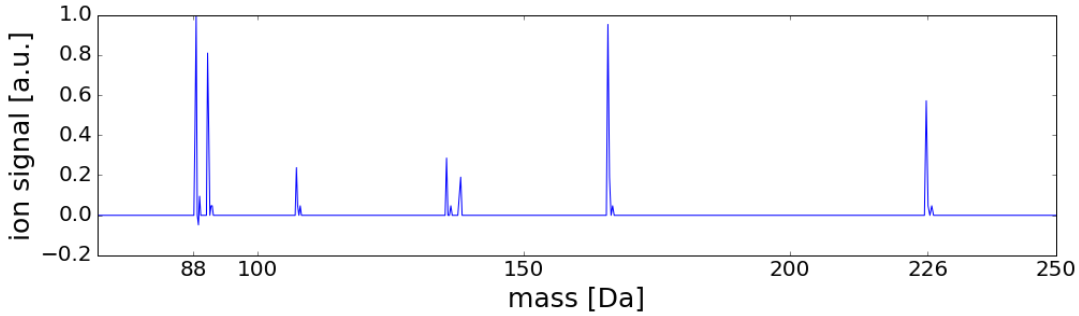

Figure 7.6: Observed TOFMS signal after ablating the $RaCl_2$ target and loading the trap with strontium ions. We calibrate the signal to the first observed signal that we assume to be $^{88}Sr^+$. Intermediate mass ions between $^{88}Sr^+$ and $^{226}Ra^+$ are a result of molecular ions that form as a result of ablation.

tium atoms from the effusive oven and ejected them towards the TOFMS. Though there was nothing to compare the observed signal against this confirmed that the TOFMS was detecting the charged particles. We used these large clouds to further optimize the high voltages used for the trap rf rods, the Einzel lenses, and the CEM. Following this optimization the radium sample was first ablated at extremely low power followed by the trap being loaded with strontium ions which were then detected with the TOFMS, see Fig. 7.5. We gradually increased the ablation laser power until signal corresponding to the radium ion mass was observed, see Fig. 7.6. We then optimized the ablation loading parameters, tuning the power and the delay of the trap turning back on following an ablation pulse.

Chapter 8

Fundamental Radium Ion Atomic Properties

This chapter provides an overview of our measurements of fundamental radium ion atomic properties. This chapter includes the contents of our work, *Measurements of electric quadrupole transitions in* $^{226}Ra^{+}$ [6].

8.1 State of Knowledge in 2019

Prior to the first laser cooling and trapping of radium ions in 2019 [5], there were only four direct radium-226 ion frequency measurements. These frequency measurements were made approximately one century ago with a hollow cathode lamp [84], and were measured at the GHz level of precision, see Table 8.1. Notably, the $S_{1/2} \rightarrow D_{3/2}$ and $S_{1/2} \rightarrow D_{5/2}$ electric quadrupole transitions were not measured in $^{226}\mathrm{Ra}^{+}$, nor were they ever driven in any radium ion isotope.

Table 8.1: Existing $^{226}Ra^{+}$ direct frequency measurements in 2019, made nearly one century ago [84]

Transition	Frequency (GHz)
$7s\ ^2S_{1/2} \rightarrow 7p\ ^2P_{3/2}$	785 723(4)
$7s\ ^2S_{1/2} \rightarrow 7p\ ^2P_{1/2}$	640 092(7)
$6d\ ^2D_{3/2} \rightarrow 7p\ ^2P_{3/2}$	423 438(6)
$7s\ ^2S_{1/2} \rightarrow 6d\ ^2D_{5/2}$	-
$6d\ ^2D_{5/2} \rightarrow 7p\ ^2P_{3/2}$	373 717(5)
$7s\ ^2S_{1/2} \rightarrow 6d\ ^2D_{3/2}$	-
$6d\ ^2D_{3/2} \rightarrow 7p\ ^2P_{1/2}$	-

As far as lifetime and branching fraction measurements are concerned, there was a single lower bound on the $D_{5/2}$ state lifetime and no measurements of the $P_{1/2}$ or $P_{3/2}$ lifetime measurements, see Table 8.2.

Table 8.2: Existing Ra^{+} lifetime and branching fraction measurements in 2019.

Ra^{+} State	Lifetime	Branching Fraction
$7p\ ^2P_{1/2}$	-	-
$7p\ ^2P_{3/2}$	-	-
$6d\ ^2D_{3/2}$	-	N/A
$6d\ ^2D_{5/2}$	$>$ 232 ms [34]	N/A

8.2 Electric Quadrupole Transition Frequencies

This section includes the contents of our work, *Measurements of electric quadrupole transitions in* $^{226}Ra^{+}$ [6].

We report the first driving of the $7s\ ^2S_{1/2} \rightarrow 6d\ ^2D_{3/2}$ and $7s\ ^2S_{1/2} \rightarrow 6d\ ^2D_{5/2}$ electric quadrupole (E2) transitions in Ra^{+}. We measure the frequencies of both E2 transitions, and two other low-lying transitions in $^{226}Ra^{+}$ that are important for controlling the radium ion's motional and internal states: $6d\ ^2D_{3/2} \rightarrow 7p\ ^2P^o_{3/2}$ and $6d\ ^2D_{5/2} \rightarrow 7p\ ^2P^o_{3/2}$.

8.2.1 Introduction

The radium ion has two subhertz-linewidth electric quadrupole (E2) transitions from the ground state: $7s\ ^2S_{1/2} \rightarrow 6d\ ^2D_{5/2}$ at 728 nm and $7s\ ^2S_{1/2} \rightarrow 6d\ ^2D_{3/2}$ at 828 nm. The E2 transition to the $D_{5/2}$ state, which has a lifetime of ∼300 ms [79], is useful for electron shelving, ground-state cooling, and controlling an optical qubit, and it could also serve as the clock transition for an optical clock [73]. Measurements of these two quadrupole transitions across a chain of isotopes can be used to obtain information related to the nuclear structure of radium, such as the specific mass shift and the change in mean-square nuclear charge radii [85, 86]. The degree of nonlinearity in a King plot comparison of the two transitions could set bounds on new physics beyond the standard model [87]. There are 11 radium isotopes between mass number 213 and 234 with half-lives longer than 1 min that could be ionized, trapped, and compared with high precision on a King plot. A precision King plot can also be made using one E2 transition in Ra^+ and the Ra $^1S_0 \rightarrow\ ^3P_0$ intercombination line at 765 nm, which has a $2\pi \times 5$ mHz linewidth [88].

In this work we measure the two $7s \rightarrow 6d$ electric quadrupole transition frequencies, as well as the frequencies of the $6d\ ^2D_{3/2} \rightarrow 7p\ ^2P^o_{3/2}$ (708-nm) and $6d\ ^2D_{5/2} \rightarrow 7p\ ^2P^o_{3/2}$ (802-nm) electric dipole transitions (see Fig. 8.1) in $^{226}Ra^+$ ($I = 0$, 1600 yr half-life). Previously the only optical frequency measurement in $^{226}Ra^+$ with an uncertainty of less than 4 GHz is that of the $7s\ ^2S_{1/2} \rightarrow 7p\ ^2P^o_{1/2}$ (468-nm) Doppler cooling transition [5]. Combining that measurement with the measurements in this work, we calculate the $6d\ ^2D_{3/2} \rightarrow 7p\ ^2P^o_{1/2}$ (1079-nm) and $7s\ ^2S_{1/2} \rightarrow 7p\ ^2P^o_{3/2}$ (382-nm) frequencies, which are useful for laser-cooling Ra^+.

For our measurements we use a single laser-cooled radium ion, which is loaded by ablating a 10 μCi $RaCl_2$ target ∼15 mm from the trap. The radio-frequency trapping voltage is turned on 20 μs after ablation to enhance the loading efficiency. The radium

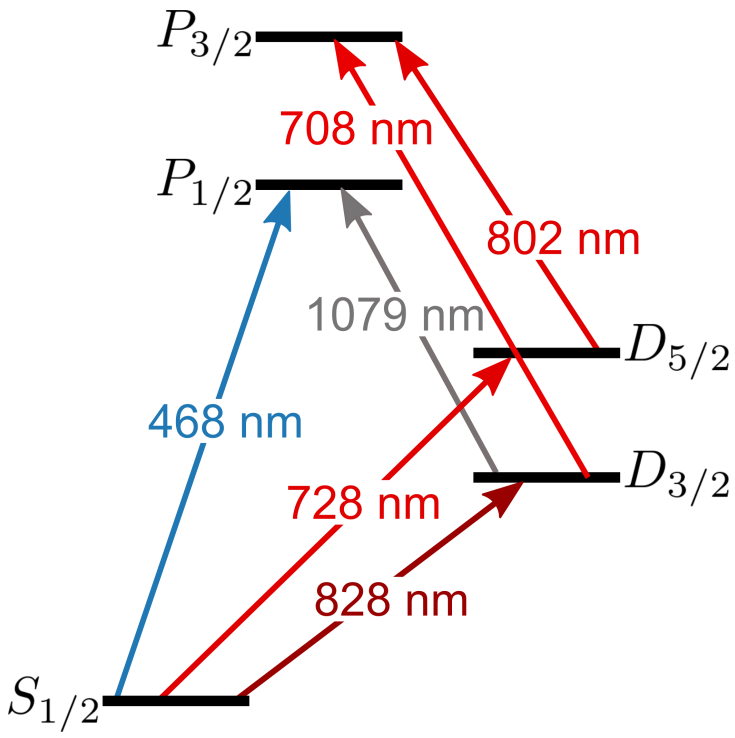

Figure 8.1: The Ra^+ energy level structure showing the transitions driven in this work.

ion trap and loading procedure used in this work have been described previously [5]. We use a heated iodine vapor cell as a frequency reference. The Ra^+ spectroscopy transitions and the iodine reference are driven with a tunable Ti:sapphire laser, whose frequency is recorded with a wavemeter (High Finesse WS-8) to determine the Ra^+ transition frequencies from the known iodine reference lines. We describe the Ra^+ transition measurements and fits in Sec. 8.2.2, and the iodine frequency reference spectroscopy in Sec. 8.2.7. From the combined iodine and Ra^+ data we determine the Ra^+ transition frequencies in Sec. 8.2.8, and with these values we present an updated King plot that includes radium-226 in Sec. 8.2.9.

8.2.2 Radium Spectroscopy

The Ra^+ transitions are measured using state detection, where the ion is bright if the population is in the cooling cycle and dark otherwise. Bright-state fluorescence photons at 468 nm are collected onto a photomultiplier tube and the counts are then time-tagged with respect to the measurement pulse sequences [57]. In 1 ms of state detection 35 photons are collected on average if the population is in the $S_{1/2}$ or $D_{3/2}$ "bright" state, and 1.5 photons of background scattered light if the population is shelved in the $D_{5/2}$ "dark" state. We set the bright-state detection threshold to 12 counts.

All Ra^+ spectroscopy pulse sequences begin with 0.5 ms of laser cooling and an initial state detection (see SD1 in Fig. 8.2). If the state detection finds the ion in the dark state, then the data point is excluded because the ion is not properly initialized. All pulse sequences finish with a second state detection step and then optical pumping to remove any remaining population from the $D_{5/2}$ state. We give a detailed description of the $7s\ ^2S_{1/2} \rightarrow 6d\ ^2D_{5/2}$ electric quadrupole "clock" transition measurement. The other measurements are similar, with brief descriptions provided.

8.2.3 $7s\ ^2S_{1/2} \rightarrow 6d\ ^2D_{5/2}$ (728 nm)

The pulse sequence for the clock transition measurement is shown in Fig. 8.2. Before each measurement we Doppler-cool the ion for 0.5 ms. The initial state detection determines whether the ion is cooled, and whether the population is in a bright state (SD1). Any population in the $D_{3/2}$ state is then optically pumped with light at 1079 nm to the ground state (P1). The $7s\ ^2S_{1/2} \rightarrow 6d\ ^2D_{5/2}$ spectroscopy transition is then driven with light at 728 nm for 1 ms (P2), and if the light is on resonance, the population can be shelved to the $D_{5/2}$ state, and the shelving probability is measured with a second state detection (SD2). To prepare for the next measurement any shelved population is cleaned

out with light at 802 nm, which drives the population to the $S_{1/2}$ and $D_{3/2}$ bright states (P3). Over many pulse sequences the 728-nm laser is swept over ∼100 MHz to drive all possible transitions between Zeeman levels of the two states. The $7s\ ^2S_{1/2} \rightarrow 6d\ ^2D_{5/2}$ spectroscopy is shown in Fig. 8.4, along with an inset of the corresponding iodine absorption reference spectrum.

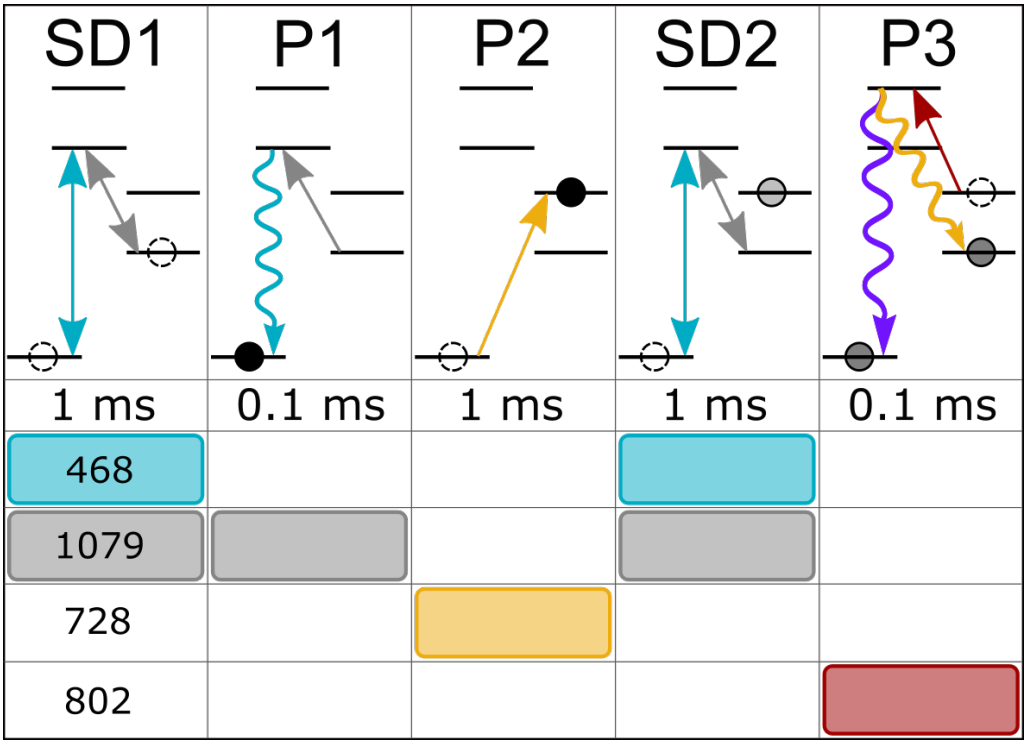

Figure 8.2: The pulse sequence for the $^2S_{1/2} \rightarrow^2 D_{5/2}$ E2 transition measurement. Squiggly lines depict E1 allowed decays, straight lines show optical pumping transitions, and double-arrows indicate optical cycling transitions.

To resolve the $S_{1/2} \rightarrow D_{5/2}$ and $S_{1/2} \rightarrow D_{3/2}$ Zeeman sub-structure of the transitions, a 7.8-G magnetic field is applied parallel to the trap's radio-frequency rods, which we define as the z axis. The magnetic field spreads the $S_{1/2} \rightarrow D_{5/2}$ transitions across ∼60 MHz. The energy splitting due to the applied magnetic field is calculated from $\Delta E_j = g_j \mu_B B m$, where g_j is the Landé g-factor for state with total angular momentum j, μ_B is the Bohr magneton, B is the magnetic field, and m is the magnetic quantum

number. The Rabi frequency for transitions between the $S_{1/2,m}$ and the $D_{5/2,m'}$ Zeeman levels is

$$\begin{aligned}\Omega =&\left|\frac{eE_0}{2\hbar}\langle S_{1/2}||r^2\mathbf{C}^{(2)}||D_{5/2}\rangle\right.\\ &\left.\sum_{j=-2}^{2}\begin{pmatrix}1/2 & 2 & 5/2\\ -m & \Delta m & m'\end{pmatrix} g^{(\Delta m)}\right|,\end{aligned} \tag{8.1}$$

where $\langle S_{1/2}||r^2\mathbf{C}^{(2)}||D_{5/2}\rangle$ is the reduced matrix element, the summation is over Wigner 3-j symbols and a geometry-dependent factor, $g^{(\Delta m)}$ [89, 90], given by

$$\begin{aligned}g^{(0)} =&\frac{1}{2}\Big|\cos(\gamma)\sin(2\phi)\Big|,\\ g^{(\pm1)} =&\frac{1}{\sqrt{6}}\Big|\cos(\gamma)\cos(2\phi)+i\sin(\gamma)\cos(\phi)\Big|,\\ g^{(\pm2)} =&\frac{1}{\sqrt{6}}\Big|\frac{1}{2}\cos(\gamma)\sin(2\phi)+i\sin(\gamma)\sin(\phi)\Big|,\end{aligned} \tag{8.2}$$

where Δm is the change in magnetic quantum number, ϕ is the angle between the laser's k vector and the magnetic field, and γ is the angle between the laser polarization and the magnetic field vector projected into the plane of incidence.

For E2 transitions $\Delta m = 0, \pm1, \pm2$ are allowed, which gives rise to 10 transitions between Zeeman levels for $S_{1/2} \rightarrow D_{5/2}$. We measure these transitions using $\phi = 45°$, and two values of γ, 0° and 90°, which suppress certain $|\Delta m|$ transitions (see Fig. 8.3). We fit the spectroscopy data to a sum of 10 Lorentzians, from which we extract the applied magnetic field, ϕ, γ, and the $S_{1/2} \rightarrow D_{5/2}$ transition frequency. Due to the 468- and 1079-nm laser polarizations, during Doppler cooling the ground-state $m = -1/2$ level is preferentially populated, and so reduces the probability of transition occurring from the $m = 1/2$ level. The ground state population imbalance is one of the fitting parameters. The ∼0.5-Hz natural linewidth of the $S_{1/2} \rightarrow D_{5/2}$ transition is broadened by laser power and magnetic field fluctuations. There are small micromotion sidebands in the spectrum

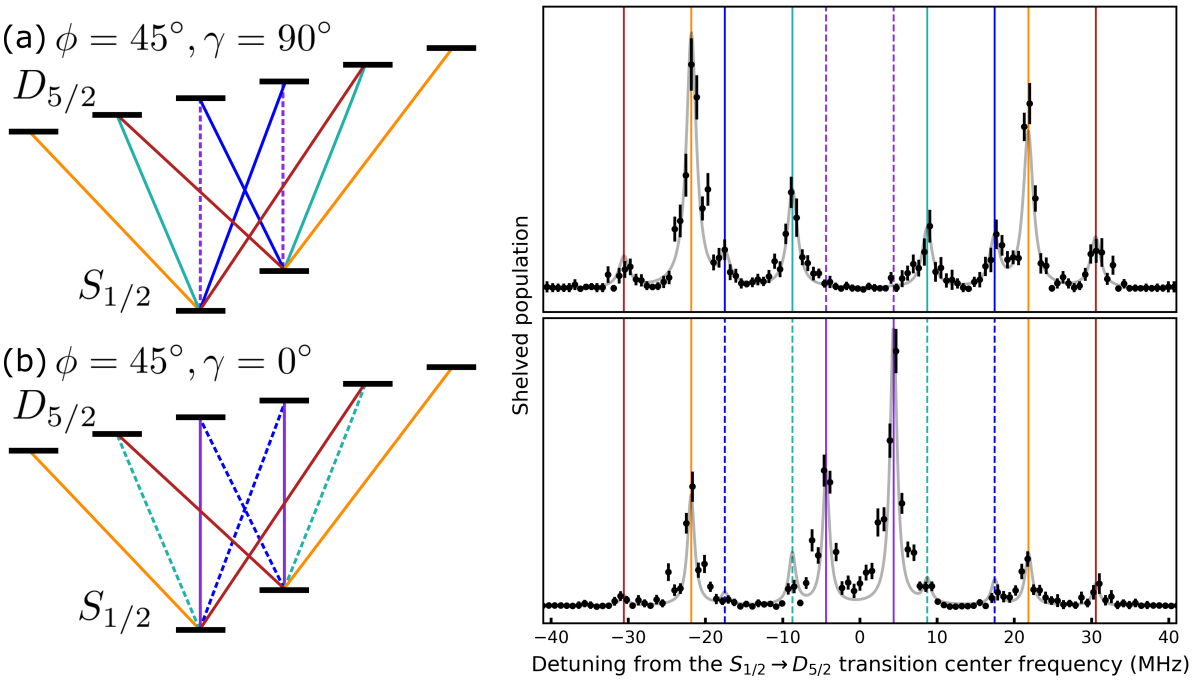

Figure 8.3: Two measurements of the $S_{1/2} \rightarrow D_{5/2}$ transition with angle $\phi = 45°$ between the k-vector and the magnetic field: (a) angle $\gamma = 90°$ between the laser polarization and the magnetic field, which suppresses $\Delta m = 0$; (b) $\gamma = 0°$, which suppresses $\Delta m = \pm 1$. Dashed lines indicate transitions suppressed by the choice of ϕ and γ. Symmetric pairs of transitions are the same color. Error bars are the most likely 68% confidence interval of a binomial distribution.

at our trap drive frequency, 1.8 MHz. We average the two center frequencies extracted from the two fits of the spectra at different values of γ to determine the $S_{1/2} \rightarrow D_{5/2}$ transition frequency.

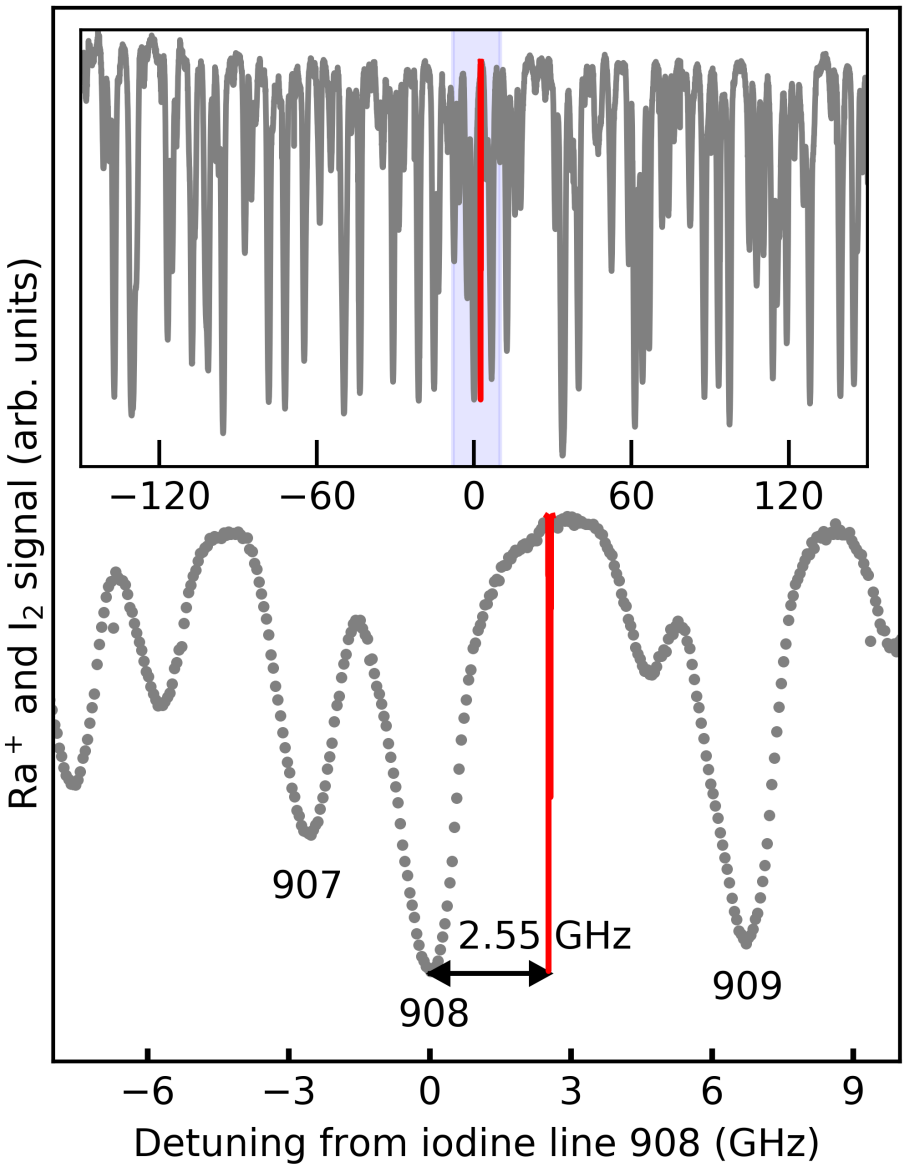

Figure 8.4: The iodine absorption spectrum is plotted with the Ra^+ scan, where the iodine data (gray) and Ra^+ data (red; see Fig. 8.3) are scaled and offset to highlight the detuning between the transitions. We use the line indices from [91, 92] to denote iodine lines. Inset: Iodine lines in a 300-GHz range around the closest reference line, 908, with the outset region highlighted in blue.

8.2.4 $6d\ ^2D_{5/2} \rightarrow 7p\ ^2P^o_{3/2}$ (802 nm)

For measuring both the $^2D_{5/2} \rightarrow\ ^2P_{3/2}$ and the $^2D_{3/2} \rightarrow\ ^2P_{3/2}$ transitions a magnetic field of ∼2.5 G is applied to prevent coherent dark states [11]. After initialization, the ion is optically pumped to the $D_{5/2}$ state with light at 468 and 708 nm for 60 μs. Any population in the $D_{5/2}$ state is then pumped with the spectroscopy light at 802 nm for 150 μs. If the light is on resonance, the population can be driven to the $P_{3/2}$ state, where decays will populate the bright states (see Fig. 8.6). After the second state detection the $D_{5/2}$ state is optically pumped with resonant 802-nm light from an external cavity diode laser.

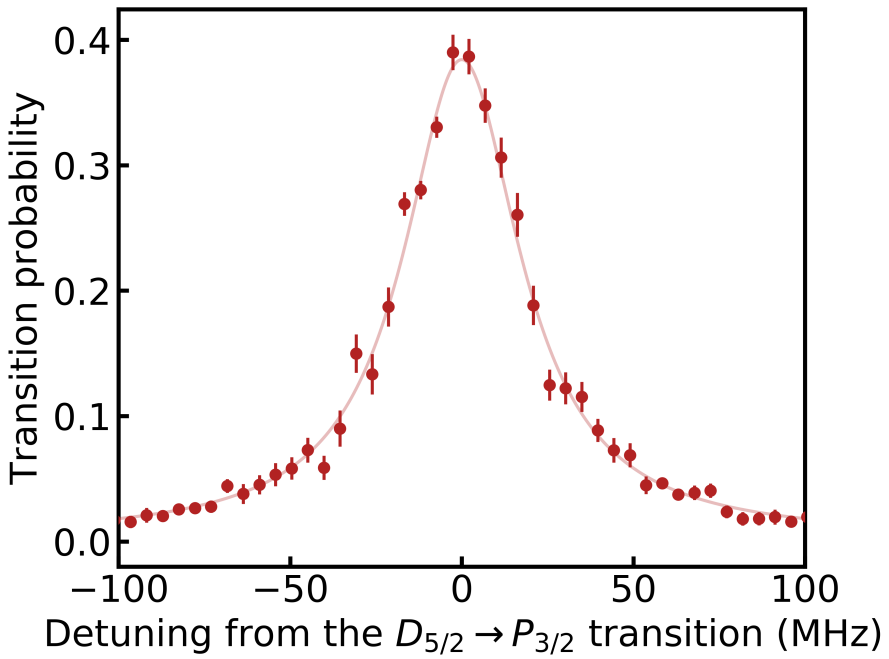

Figure 8.5: Spectroscopy of the $D_{5/2} \rightarrow P_{3/2}$ transition. A Lorentzian fit gives an FWHM of 41.5(9) MHz.

To determine the line center for the $D_{5/2} \rightarrow P_{3/2}$ transition we fit the data to a Lorentzian (see Fig. 8.6). The full width at half-maximum (FWHM) of 41.5(9) MHz gives a lower bound of 3.84(9) ns for the $P_{3/2}$-state lifetime, which agrees with the calculated

value of 4.73 ns [79]. The $P_{3/2}$ state lifetime would later be measured as 4.78(3) ns [93]. A direct measurement of the The 802-nm laser light is incident on the ion along the trap's z axis to minimize micromotion broadening [8]. We measured the 802-nm laser's beam waist to be 300(50) μm and our beam power to be 1.2(1) μW. We estimate that the transition is power broadened by ∼8 MHz from the 802-nm beam waist and power.

8.2.5 $7s\ ^2S_{1/2} \rightarrow 6d\ ^2D_{3/2}$ (828 nm)

After initialization, any population in the $D_{3/2}$ state is optically pumped with light at 1079 nm for 100 μs to the ground state. The $7s\ ^2S_{1/2} \rightarrow 6d\ ^2D_{3/2}$ transition is driven with light at 828 nm for 10 ms, and if the light is on resonance, the ion can be shelved to the $D_{3/2}$ state. Any population in the $D_{3/2}$ state is then pumped with light at 708 nm for 60 μs, which drives the population to the $P_{3/2}$ state whose decays populate the $S_{1/2}$ and $D_{5/2}$ states.

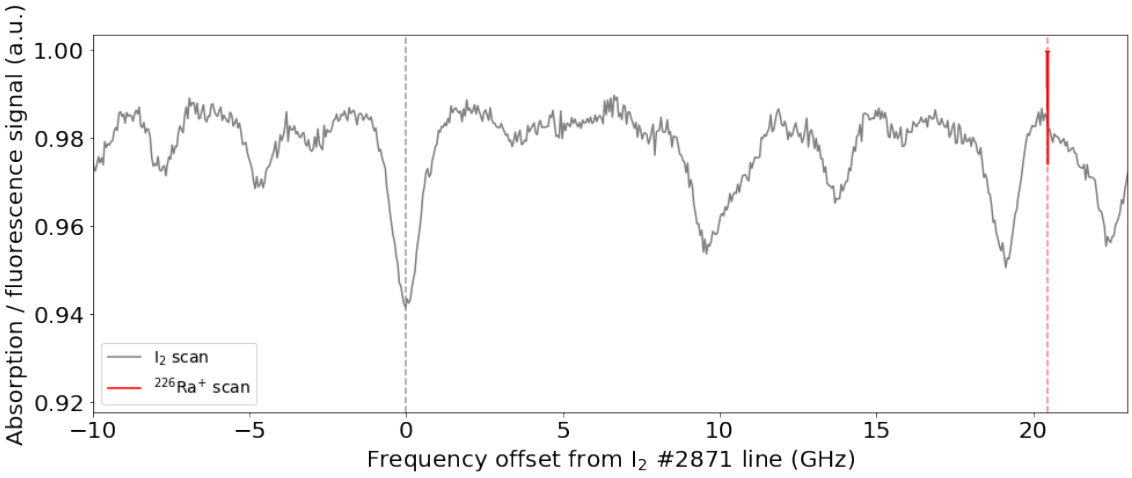

Figure 8.6: The iodine absorption spectrum is plotted with the $S_{1/2} \rightarrow D_{3/2}$ Ra^+ scan, where the iodine data (gray) and Ra^+ data (red) are scaled and offset to highlight the detuning between the transitions. The closest iodine from the $S_{1/2} \rightarrow D_{3/2}$ is line 2871.

The population is shelved to the $D_{5/2}$ state with a low fidelity due to the branching

fraction from the $P_{3/2}$ state. The shelved probability is determined from a binomial distribution of k shelved events (corresponding to fewer than 12 photons collected during the second state detection) in n trials (where the ion is properly initialized at the beginning of the pulse sequence). There are eight transitions between Zeeman levels for the $S_{1/2} \rightarrow D_{3/2}$ transition. We fit the spectra in a similar fashion as the $S_{1/2} \rightarrow D_{5/2}$ transition to extract the center frequency.

8.2.6 $6d\ ^2D_{3/2} \rightarrow 7p\ ^2P^o_{3/2}$ (708 nm)

After initialization, any population in the $S_{1/2}$ state is optically pumped with light at 468 nm for 100 μs to the $D_{3/2}$ state. The population is then pumped with light at 708 nm for 50 μs, and if the light is on resonance, the population can be driven to the $P_{3/2}$ state whose decays populate the $S_{1/2}$ and $D_{5/2}$ bright states. The data are fit to a Lorentzian to determine the center frequency.

8.2.7 Iodine Frequency Reference

For iodine absorption spectroscopy a Ti:sapphire laser is scanned at 10 MHz per second across a frequency range that includes at least two iodine reference lines, as well as the target Ra^+ transition. To reduce drift in the wavemeter measurement we measure the iodine spectra both before and after Ra^+ spectroscopy. We use one iodine line as the frequency reference, and we determine the line's frequency by fitting the line's absorption dip in both scans to a Voigt function and averaging the two centers. We then calibrate the iodine line frequency we measured with a wavemeter to an absolute frequency using IodineSpec5 [94, 95], which provides a comprehensive I_2 reference data set based on iodine spectrum measurements including the original iodine atlas work [91, 92]. We fit the corresponding absorption dip in the IodineSpec5 data set to a Voigt function to

determine the absolute frequency of the measured iodine line center.

The $^{127}I_2$ vapor cell frequency reference (75 mm long, with a 19-mm outer diameter and windows angled at 11°) is heated in a tube furnace to ∼500°C, the temperature at which the iodine atlas lines were measured [91, 92]. We scan the temperature of the I_2 cell by ±50°C around 500°C and vary an applied magnetic field by ±4 G, and for both we find frequency shifts within the fitting uncertainty. To compensate for laser power drifts the power is recorded on a reference photodiode before the iodine cell.

8.2.8 Ra^+ Transition Frequencies

The Ra^+ transition frequencies are calculated from the frequency difference between the radium and the iodine reference line centers that are recorded with a wave-meter. The fit iodine reference lines calculated in IodineSpec5 are used to calibrate the wavemeter frequencies.

The closest iodine reference line to the $S_{1/2} \rightarrow D_{5/2}$ transition is line 908 from [91, 92], which we calculate using IodineSpec5 to be 412 004.754(15) GHz. From the difference between radium and iodine spectroscopy center fits, 2.947 GHz, we determine a transition frequency of 412 007.701(18) GHz. We take the total uncertainty in our measurements to be $\sigma_{\text{total}} = \sqrt{\sigma^2_{\text{Ra}^+} + \sigma^2_{\text{I}_2} + \sigma^2_{\text{spec}} + \sigma^2_{\text{wm}}}$, where σ_{Ra^+} is the radium fitting uncertainty, σ_{I_2} is the measured iodine fitting uncertainty, σ_{spec} is the IodineSpec5 line uncertainty, and σ_{wm} is the wavemeter uncertainty, 10 MHz. The IodineSpec5 line uncertainties range from 2 to 45 MHz for the lines referenced in this work. The IodineSpec5 fitting uncertainties are on the kilohertz level and are negligible compared to the other uncertainties.

The reported value for the $D_{3/2} \rightarrow P_{1/2}$ transition, 277 818.95(8) GHz, comes from the frequency difference between the $S_{1/2} \rightarrow D_{3/2}$ E2 transition measured in this work and the measurement of the $S_{1/2} \rightarrow P_{1/2}$ transition by Fan, *et al.* [5].

Table 8.3: Summary of $^{226}Ra^{+}$ frequency measurements. All units are GHz. *Frequencies calculated from measurements. †Frequencies extrapolated from a King plot [96].

Transition	[84]	[73]	This work, [5]
$S_{1/2} \rightarrow P_{3/2}$	785 723(4)	785 721.670(70)*	785 722.10(3)*
$S_{1/2} \rightarrow P_{1/2}$	640 092(7)	640 096.647(23)*	640 096.63(6) [5]
$D_{3/2} \rightarrow P_{3/2}$	423 438(6)	···	423 444.39(3)
$S_{1/2} \rightarrow D_{5/2}$	···	···	412 007.701(18)
$D_{5/2} \rightarrow P_{3/2}$	373 717(5)	···	373 714.40(2)
$S_{1/2} \rightarrow D_{3/2}$	···	362 277.361(33)†	362 277.68(5)
$D_{3/2} \rightarrow P_{1/2}$	···	277 819.285(18)†	277 818.95(8)*

From our measurements we can calculate the $S_{1/2} \rightarrow P_{3/2}$ (382-nm) transition frequency by summing either the 728- and 802-nm frequencies, 785 722.10(3) GHz, or the 828- and 708-nm frequencies, 785 722.07(5) GHz. Both pairs of transitions originate in the ground state and end in the $P_{3/2}$ state. The two calculated frequencies are in good agreement, and we report the value calculated from the 728- and 802-nm frequencies, as the uncertainty in the underlying measurements are smaller. The measured and calculated frequencies are summarized in Table 8.3.

There are discrepancies between the transition frequencies measured in this work and those reported by Nunez, *et al.* [73] (see Table 8.3). We are able to resolve some of the discrepancies by redoing the analysis in [73]. The $D_{3/2} \rightarrow P_{1/2}$ transition frequency reported in [73], 277 819.285(18) GHz, is extrapolated from a King plot with data from Giri *et al.* [96]. From the 1079 nm/482 nm King plot (Fig. 4 in [96]) we find a slope of $-0.342(7)$ and a y-intercept of $-2.2(5)$ THz amu, which gives the transformed isotope shift [see Eq. (4) below] of 54.5(1.3)THz amu and the $D_{3/2} \rightarrow P_{1/2}$ transition frequency in $^{226}Ra^{+}$ of 277 819.2(3) GHz. This value agrees with our measurement. The $S_{1/2} \rightarrow D_{3/2}$ transition frequency reported in [73] is calculated from the frequency difference between the $S_{1/2} \rightarrow P_{1/2}$ and the $D_{3/2} \rightarrow P_{1/2}$ transitions. With the recalculated value of the $D_{3/2} \rightarrow P_{1/2}$ frequency, the $S_{1/2} \rightarrow D_{3/2}$ transition frequency is 362 277.4(3) GHz, which

is also in agreement with our measurement. There remains the discrepancy between the $S_{1/2} \rightarrow P_{3/2}$ frequency measured in this work and the value reported in [73]. This discrepancy could be resolved by direct spectroscopy of the $S_{1/2}$-to-$P_{3/2}$ transition in one of many radium isotopes, including isotope(s) 212, 214, or 221-226 [35].

8.2.9 King Plot

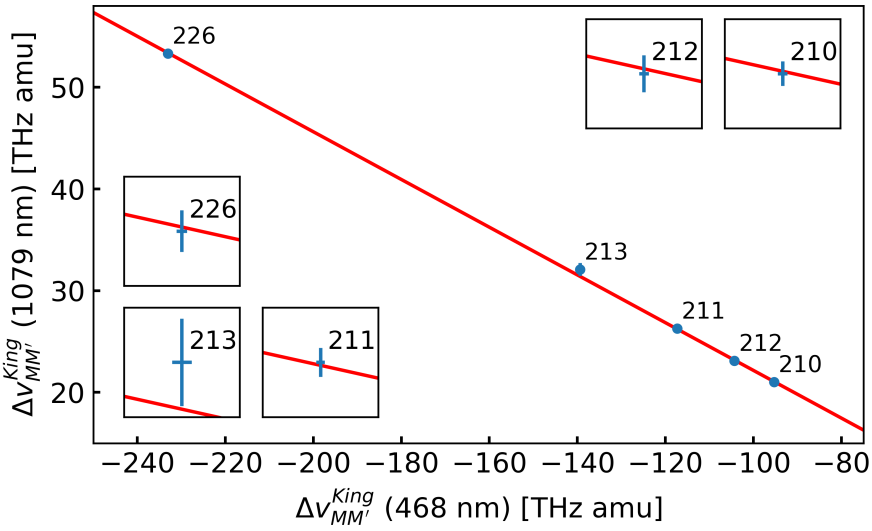

Figure 8.7: A King plot of the transformed isotope shifts of the $D_{3/2} \rightarrow P_{1/2}$ versus the $S_{1/2} \rightarrow P_{1/2}$ transitions. The reference isotope is $^{214}Ra^{+}$. Insets: Magnifications of x200 for the 468 nm axis and x50 for the 1079 nm axis.

We determine isotope shifts for the 708- and 1079-nm transitions in $^{226}Ra^{+}$. The isotope shift between a target and a reference isotope is $\delta\nu_{MM'} = \nu_M - \nu_{M'}$, where M is the target isotope nuclear mass, M' is the reference isotope nuclear mass, and ν is the transition frequency. We use $^{214}Ra^{+}$, which has a closed neutron shell, as the reference isotope [36]. The 1079-nm $^{214}Ra^{+}$ reference frequency is 277 805.656 GHz [96] and the 708-nm $^{214}Ra^{+}$ reference frequency is 423 434.989 GHz [34]. Isotope shifts of 468, 708,

and 1079 nm are listed in Table 8.4. The isotope shift is parameterized as

$$\delta\nu_{MM'} = (K_{\mathrm{NMS}} + K_{\mathrm{SMS}})\frac{M - M'}{MM'} + F_{\mathrm{FS}}\lambda_{MM'}, \tag{8.3}$$

where K_{NMS} and K_{SMS} are the normal and specific mass shifts, F_{FS} is the field shift, and $\lambda_{MM'}$ is the Seltzer moment, which to lowest order is the difference in mean square nuclear charge radii, $\lambda_{MM'} \approx \delta\langle r^2\rangle_{MM'}$ [85]. The transformed isotope shift is

$$\Delta\nu^{\mathrm{King}}_{MM'} = \delta\nu_{MM'}\frac{MM'}{M - M'} - K_{\mathrm{NMS}}, \tag{8.4}$$

from which the ratio of field shifts between transitions and the difference in specific mass shifts can be determined [97]. King plot comparisons of the transformed isotopes shifts give the Ra^+ field shift ratios, $F_{708}/F_{468} = -0.171(3)$ and $F_{1079}/F_{468} = -0.235(2)$, which are summarized in Table 8.5. The 1079 nm/468 nm King plot is shown in Fig. 8.7.

Table 8.4: Measured Ra^+ isotope shifts of the 468-, 708-, and 1079-nm transitions for $^{210-213}Ra^+$ and $^{226}Ra^+$ relative to $^{214}Ra^+$. All units are MHz. The 468 nm isotope shifts are from [36]. The 708- and 1079-nm isotope shifts for $^{210-213}Ra^+$ are from [98]. *An isotope shift calculated in this work.

Isotope	468 nm	708 nm	1079 nm
210	8449(6)	···	-1884(16)
211	7770(4)	···	-1755(14)
212	4583(3)	-701(20)	-1025(12)
213	3049(3)	-453(34)	-707(14)
214	0	0	0
226	−57 852(18)	9403(27)*	13 294(76)*

8.2.10 Conclusion

The first driving of the 728- and 828-nm electric quadrupole transitions in Ra^+ lays the groundwork for quantum information science and precision measurement experiments

with Ra^+. Isotope shift spectroscopy of Ra^+ dipole transitions has been done at the ISOLDE facility at CERN, and could be extended to a high precision by trapping Ra^+ and measuring the E2 transitions [99]. Estimates for the nonlinearities of a King plot of radium's two narrow linewidth transitions following [100] could guide searches to constrain new physics.

Table 8.5: $^{226}Ra^+$ field shift ratios.

FS Ratio	Theory [98]	Experiment [98]	This work
F_{708}/F_{468}	-0.16(1)	-0.136(57)	-0.171(3)
F_{1079}/F_{468}	-0.23(2)	-0.244(11)	-0.235(2)

8.3 $S_{1/2} \rightarrow P_{3/2}$ Transition Frequency

As detailed in the previous section, our calculated $S_{1/2} \rightarrow P_{3/2}$ transition frequency [6] had a discrepancy of five combined standard deviations with that of [73], see Table 8.6. To resolve this discrepancy, we directly measured the $S_{1/2} \rightarrow P_{3/2}$ transition frequency using a single laser-cooled radium ion referenced to a transition in molecular iodine, see Fig. 8.8. The details of this work can be found in [101]. We found the direct frequency measurement to be consistent with that of the calculated frequency made from the sum of two direction frequency measurements made in [6], and described above.

Table 8.6: Summary of $7s\ ^2S_{1/2} \rightarrow 7p\ ^2P^o_{3/2}$ transition frequency measurements in $^{226}Ra^+$. All values are offset from 785 722 000 MHz. *Frequencies calculated from indirect measurements.

Transition	[84]	[73]	[6]	[101]
$S_{1/2} \rightarrow P_{3/2}$	1000(4000)	$-330(70)$*	100(30)*	110(20)

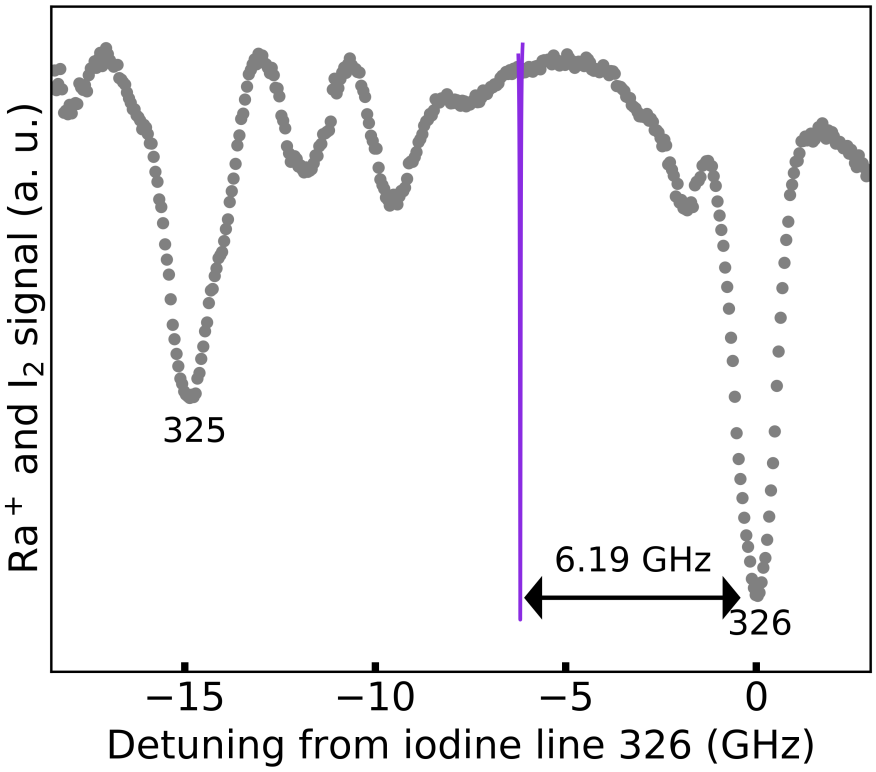

Figure 8.8: The iodine (gray) and radium (purple, frequencies divided by two) spectroscopy data scaled and vertically offset. The closest iodine lines to the transition are lines 325 and 326 [91].

8.4 Branching Fraction and Lifetime Measurements

Precise values for electric dipole matrix elements provide fundamental knowledge for atomic and molecular systems and are needed for many applications, including the development of atomic clocks. Measurements of excited-state lifetimes and branching fractions are used to calculate the dipole matrix elements, which can then be used to determine leading systematic effects of an optical clock, such as the blackbody radiation shift and laser-induced ac Stark shifts [102].

8.4.1 $P_{1/2}$ State Branching Fraction

Measurements of the $P_{1/2}$ state branching fractions are summarized in Chapter 7 and in [5].

8.4.2 $P_{3/2}$ State Branching Fraction

Our measurement of the radium ion $P_{3/2}$ state branching fractions can be found in [103]. These measurements used a similar measurement scheme to branching fraction measurements with Ca^+ [104], Sr^+ [105], and Ba^+ [106].

8.4.3 $P_{3/2}$ State Lifetime Measurement

Our measurement of the radium ion $P_{3/2}$ state lifetime measurement can be found in [93]. These measurements used a similar measurement scheme to the lifetime measurements in Ca^+ [107, 108] and Lu^+ [109].

8.4.4 $P_{1/2}, D_{3/2}, D_{5/2}$ State Lifetime Measurements

The radium ion $P_{1/2}$ state lifetime can be calculated from measurements of the magic wavelength, which is the zero crossing of the dynamic differential scalar polarizability of the $S_{1/2} \rightarrow D_{5/2}$ clock transition. Measurements of the magic wavelength in Ca^+ [110] and Ba^+ [111] have been made. Theoretical calculations of the magic wavelength have been made for the radium ion [112]. Our group is preparaing to make the measurement of the magic wavelength with a radium-225 clock, because the light shift can be measured to higher precision due to the magnetic field insensitive clock transition of radium-225.

The radium ion $D_{3/2}$ and $D_{5/2}$ state lifetimes can be measured by optically pumping the population to the respective excited state and waiting a variable amount of time to see if the population has decayed back to the ground state or not. We have made a

preliminary measurement of the $D_{5/2}$ state lifetime, see Fig. 8.9, and of the $D_{3/2}$ state lifetime. Fits to an exponential decay give a lifetime of 301.5(1.3) ms for the $D_{5/2}$ state and 625(20) ms for the $D_{3/2}$ state, in good agreement with existing theoretical calculations [79]. The preliminary measurements are limited by background gas collisions, and we are waiting to break vacuum to try to achieve a lower background gas pressure. Because the radium atom mass is so high, high-precision measurements of the lifetime can serve as a useful test for quantum electrodynamics.

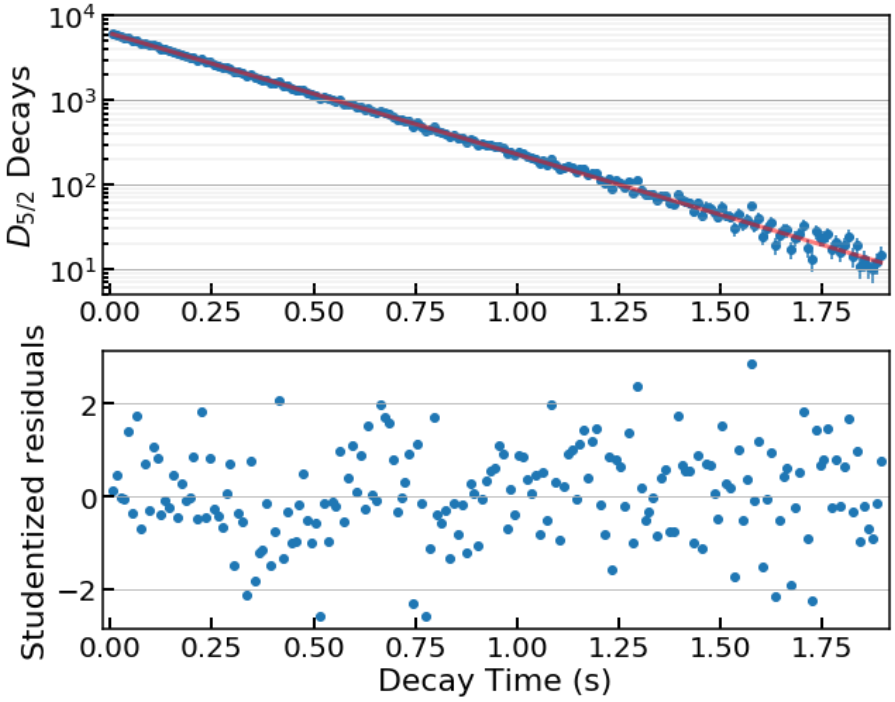

Figure 8.9: Observed decays and their respective residuals as a function of decay time for the radium ion $D_{5/2}$ state. A fit to the exponential decay gives a lifetime of 301.5(1.3) ms. The population is pumped to the $D_{5/2}$ state with light at 468, 1079, and 708 nm.

8.5 Current State of Knowledge

This chapter has provided a summary of our existing and ongoing measurements of radium ion atomic properties. Currently, all low-lying radium-226 transition frequencies have been measured on the MHz level, see Table 8.7, and branching fractions of the $P_{1/2}$ and $P_{3/2}$ state have been measured, see Table 8.8. Lifetime measurements are ongoing, with a value of the $P_{3/2}$ state lifetime already reported [93].

Table 8.7: $^{226}Ra^{+}$ direct frequency measurements as of 2022. * denotes a preliminary measurement

Transition	Frequency (GHz)
$7s\ ^2S_{1/2} \rightarrow 7p\ ^2P_{3/2}$	785 722.11(3) [101]
$7s\ ^2S_{1/2} \rightarrow 7p\ ^2P_{1/2}$	640 096.63(6) [5]
$6d\ ^2D_{3/2} \rightarrow 7p\ ^2P_{3/2}$	423 444.39(3) [6]
$7s\ ^2S_{1/2} \rightarrow 6d\ ^2D_{5/2}$	412 007.701(18) [6]
$6d\ ^2D_{5/2} \rightarrow 7p\ ^2P_{3/2}$	373 714.40(2) [6]
$7s\ ^2S_{1/2} \rightarrow 6d\ ^2D_{3/2}$	362 277.68(5) [6]
$6d\ ^2D_{3/2} \rightarrow 7p\ ^2P_{1/2}$	277 818.95(8) [6]

Table 8.8: $^{226}Ra^{+}$ lifetime and branching fraction measurements as of 2022.

Ra^{+} State	Lifetime	Branching Fraction
$7p\ ^2P_{1/2}$	$\geq$ 7.3(1) ns [5]	0.9104(7), 0.0896(7) [5]
$7p\ ^2P_{3/2}$	4.78(3) ns [93]	0.87678(20), 0.10759(10), 0.01563(21) [103]
$6d\ ^2D_{3/2}$	301.5(1.3)* ms	N/A
$6d\ ^2D_{5/2}$	625(20)* ms	N/A

Chapter 9

Precision Timekeeping

This chapter introduces atomic clocks and some of their features, applications, and future directions.

9.1 Atomic Clocks

Atoms are an ideal frequency standard because any element, regardless of space or time is absolutely alike in every physical property [113]. By building devices that count the frequency of the mechanical oscillation of an electron about an atom's core, we can realize robust timekeeping systems when environmental and relativistic effects are considered. The first molecular atomic clock was demonstrated with ammonia molecules as the source of vibrations in 1949. Shortly after, atomic clocks that used cesium began development, and in 1967 the 13th General Conference on Weights and Measures redefined the second as the inverse of the 9,192,631,770 Hz ground state hyperfine resonance frequency of the cesium-133 atom. The cesium standard remains to this day.

9.2 Optical Atomic Clocks

Optical atomic clocks use lasers, whose light is stabilized to narrow-linewidth optical transitions in neutral atoms or trapped ions, as the oscillator, and optical frequency combs as the counter. Because the frequency of optical transitions is higher than the frequency of microwave transitions, optical clocks can achieve higher stability and performance than their microwave counterparts. Optical clocks are now the most precise instrument ever realized [1], and are exciting for many science and engineering applications, including searches for new physics and the improvement of global navigation satellite systems [113].

9.3 Transportable Optical Clocks

A transportable optical clock is a clock that can be transported out of a laboratory environment. Early demonstrations have seen optical clocks placed on opposite ends of Tokyo Skytree [114] and separated by long distances in mountain ranges [115]. These results are exciting for a fully realized transportable optical clock that would able to be remotely deployed and operated for a long period of time without maintenance, similar to existing rubidium, hydrogen maser, or the recently demonstrated Hg^+ systems in space.

9.4 Global Navigation Satellite Systems

Atomic clocks are the enabling technology behind global navigation satellite systems. By measuring the time delay between signals sent from atomic clocks on Earth and atomic clocks on satellites, the distance between two systems can be determined in the simplest sense by multiplying the time delay by the speed of light c. At this times, all atomic clocks on satellites are based on microwave standards. Shifting to transportable optical clocks is appealing for improving the operation of global navigation satellite systems, but

will require robust and compact clock components.

9.5 Integrated Photonics

The use of integrated photonics with chip traps is promising for achieving small clock form factors and system robustness, where alignment is lithographically defined. On-chip lasers also eliminate the need for optical access through magnetic field shielding, reducing magnetic field noise at the ion. This could be important for operation in space where magnetic field noise is more than 100 times that on Earth [4]. Recently, the Sr^+ ion was laser-cooled and the clock transition coherently manipulated with light delivered entirely via integrated photonic Si_3N_4 grating couplers and waveguides [22]. The advances with Si_3N_4 photonics are appealing, but optical absorption losses in the material increase exponentially as wavelengths drop below 450 nm [23]. Such losses require higher starting

Table 9.1: Cooling and clock laser wavelengths for existing trapped ion clocks.

Species	λ_{cool} (nm)	λ_{clock} (nm)
$^{199}Hg^+$	194	282
$^{115}In^+$	231	236
$^{27}Al^+$ (Mg^+)	279.5	267
$^{171}Yb^+$ (oct.)	370	467
$^{171}Yb^+$ (quad.)	370	436
$^{40}Ca^+$	397	729
$^{88}Sr^+$	422	674
$^{225}Ra^+$	468	728
$^{138}Ba^+$	493	1762
$^{176}Lu^+$	646	804

laser powers, which leads to higher thermal loads and degradation. AlN waveguides have the potential to extend integrated photonics further into the blue, as the onset of losses for AlN occurs around 400 nm, but current crystals suffer from high defect density and are limited to 25 mm wafers [116, 23]. In either case, material defects and optical losses

will be significantly less acute at longer wavelengths. This makes systems such as Ra^+, whose shortest wavelength at 468 nm is far from the UV compared to most optical clocks, see Table 9.1, and redder than the cooling transitions of Ca^+ and Sr^+ (397 nm and 422 nm), especially promising for a compact transportable optical clock. A render of what a compact, transportable clock might look like is shown in Fig. 9.1. There, not only is the light delivered from integrated photonic waveguides, but also the lasers themselves are on the chip.

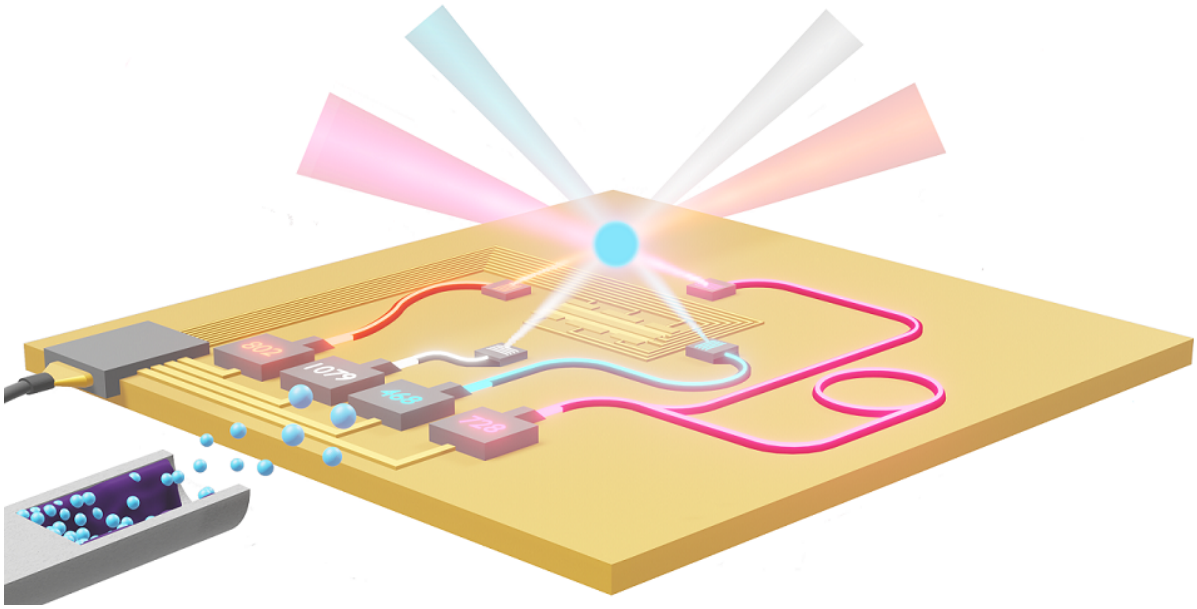

Figure 9.1: Vision of a compact, transportable Ra^+ optical clock. Radium atoms (teal) accumulate in the oven via nuclear decays from thorium (purple). An applied current heats the oven, which generates a flux of radium atoms, that can be photo-ionized and loaded into the trap. The Doppler cooling wavelength at 468 nm is far from the UV compared to nearly all optical clocks, and promising for integrated on-chip photonic technology.

9.6 Redefinition of the Second

The performance of several optical clocks with various atoms has now surpassed that of the primary cesium frequency standard [117, 118, 119, 120], which marks a significant

advance towards a proposed redefinition of the second [121]. Still, the question of what atomic species should serve as the primary frequency standard in the redefinition of the second remains. Nominally optical clocks that have high transition frequencies and low total systematics, such as the Al^+ ion optical clock [117], could serve as this primary standard. However, the deep-UV transition could limit the long-term performance and system reliability. Therefore, exploring different systems in neutral atoms and trapped ions is desirable to find a balance between achievable performance and reliability for a primary frequency standard. As optical frequency combs enable frequency comparison with accuracies at 10^{-19} or lower [122], they enable the dissemination of time with secondary representations of the second through frequency comparisons. If the secondary standards have similar stability and uncertainties as the primary standard, they can serve as a powerful time-keeping extensions anywhere in the world. These secondary standards could then be systems that are more robust, able to be readily produced and deployed. Optical fiber links between nearby research labs has proven to be an effective way to directly compare clock optical frequencies [1]. However, direct fiber links are not feasible between continents, and the accuracy of the intercontinental frequency transfer and comparison will be limited by the stability of atomic clocks on satellites. Therefore, it is necessary to develop robust, transportable optical clocks that can operate in space if a redefinition of the second is to be realized [123]. Ion clocks such as $^{87}Sr^+$ and $^{225}Ra^+$, are promising for transportable systems due to their integrated photonic friendly transitions, low power requirements, and magnetic field insensitive transitions. Optical frequency comparisons between $^{87,88}Sr^+$ and $^{225,226}Ra^+$ and measurements of their absolute transition frequencies will establish these ions as secondary frequency standards. Currently, none of these isotopes have existing frequency comparisons with other optical frequency standards, see Fig. 9.2, but we look to make these measurements in the near future.

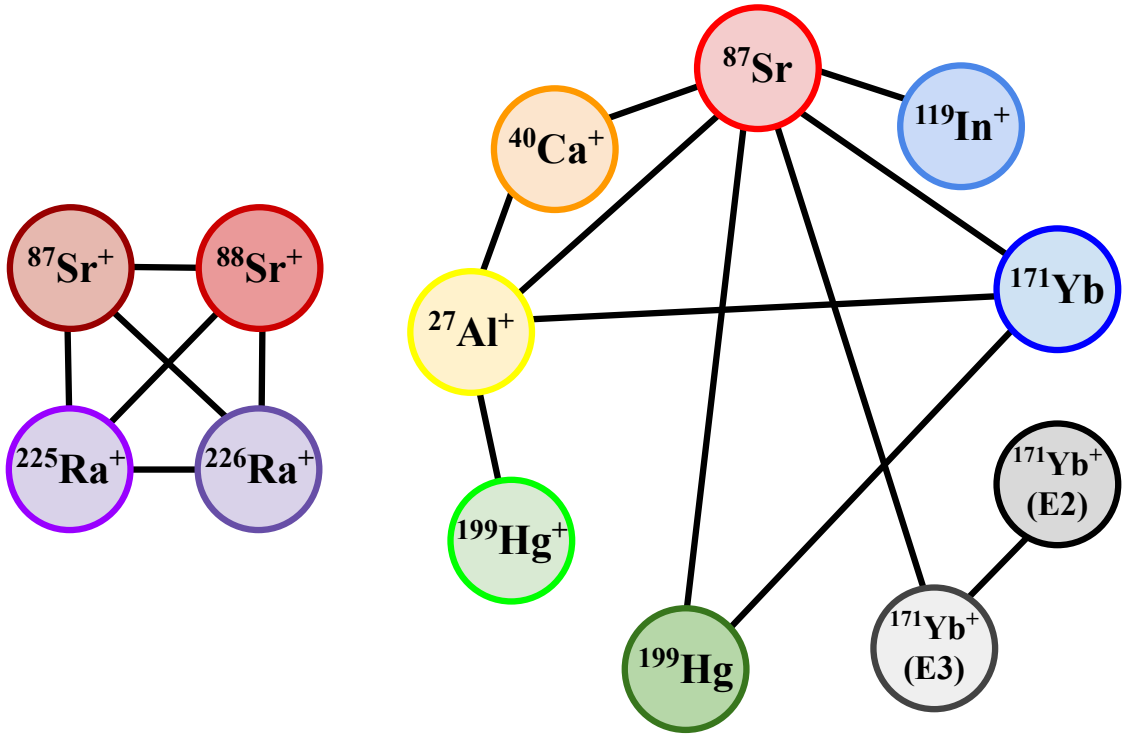

Figure 9.2: (left) Proposed first frequency comparison between radium and strontium ion clocks. Four different optical clocks could be compared: $^{87}Sr^{+}$, $^{88}Sr^{+}$, $^{225}Ra^{+}$, and $^{226}Ra^{+}$. (right) Existing optical frequency comparisons.

Chapter 10

A Radium Ion Optical Clock

This chapter includes the contents of our work, *Radium Ion Optical Clock* [7], additional information on the $^{226}Ra^{+}$ clock, and plans for a $^{225}Ra^{+}$ ion optical clock.

10.1 $^{226}Ra^{+}$ Optical Clock

We report the first operation of a Ra^{+} optical clock, a promising high-performance clock candidate. The clock uses a single trapped $^{226}Ra^{+}$ ion and operates on the $7s\ ^2S_{1/2} \rightarrow 6d\ ^2D_{5/2}$ electric quadrupole transition. By self-referencing three pairs of symmetric Zeeman transitions, we demonstrate a frequency instability of $1.1\times10^{-13}/\sqrt{\tau}$, where τ is the averaging time in seconds. The total systematic uncertainty is evaluated to be $\Delta\nu/\nu = 9 \times 10^{-16}$. Using the clock, we realize the first measurement of the ratio of the $D_{5/2}$ state to the $S_{1/2}$ state Landé g-factors: $g_D/g_S = 0.598\,805\,3(11)$ A Ra^{+} optical clock could improve limits on the time variation of the fine structure constant, $\dot{\alpha}/\alpha$, in an optical frequency comparison. The ion also has several features that make it a suitable system for a transportable optical clock.

Optical clocks, based on narrow-linewidth atomic transitions, are the most precise

instruments ever realized [1]. The performance of several optical clocks, using different atoms, have now surpassed that of the primary cesium frequency standard [117, 118, 119, 120], which marks a significant advance toward a proposed redefinition of the second [121]. Optical clocks also have the potential to uncover new physics beyond the standard model at the high-precision, low-energy frontier, including searches for ultralight scalar dark matter [124], the time variation of fundamental constants [125, 2], and violations of Einstein's equivalence principle [114]. In an effort to improve clock performance, atomic systems that are less sensitive to limiting systematic uncertainties such as Lu^+ [126] and Ba^{4+} [127] have been proposed. For both advancing clock performance and for their enhanced sensitivity to potential sources of new physics, systems including highly-charged ions [128] and a radioactive thorium nuclear clock [129, 130] are being pursued.

The radium ion is well suited to realizing a high-performance optical clock [73]. The $7s\ ^2S_{1/2} \rightarrow 6d\ ^2D_{5/2}$ electric quadrupole clock transition ($\lambda = 728$ nm, $\tau \approx 300$ ms, $\Gamma/2\pi = 0.5$ Hz) in Ra^+ has a small, negative differential static scalar polarizability (DSSP) $\Delta\alpha_0 = -22.2(1.7)$ a.u. [131]. This leads to both a small frequency shift due to the blackbody radiation (BBR) environment and allows for clock operation at a trap drive frequency (6.2 MHz) such that the micromotion-induced scalar Stark shift and the second-order Doppler shift cancel [132, 133]. Along with the expected clock performance, the radium ion has the largest positive enhancement to the time variation of the fine structure constant, $\kappa_{\mathrm{Ra}} = 2.8$, of any demonstrated clock [134]. The current constraint on $\dot{\alpha}/\alpha$ is derived from a frequency comparison between an optical clock based on the Yb^+ (E2) transition ($\tau \approx 50$ ms) and a second clock based on the Yb^+ (E3) transition [2]. Considering sensitivities of demonstrated clocks, the Yb^+ (E2) transition has the second largest positive enhancement to the time variation of the fine structure constant, $\kappa_{\mathrm{E2}} = 1$, and the Yb^+ (E3) transition has largest negative enhancement, $\kappa_{\mathrm{E3}} = -6$. This makes the radium ion an appealing system to compare against other clocks to improve constraints

on $\dot{\alpha}/\alpha$.

In this Letter, we demonstrate the first operation of a radium optical clock by stabilizing a narrow-linewidth laser at 728 nm to the $7s\ ^2S_{1/2} \rightarrow 6d\ ^2D_{5/2}$ transition of a single $^{226}Ra^+$ ion ($I = 0$). The 728 nm laser is an external cavity diode laser stabilized to an ultralow expansion glass cavity. We present an evaluation of the key systematic shifts and uncertainties as well as a self-referenced measurement of the clock frequency instability. From measurements made during the clock operation, we report the first measurement of the ratio of the $D_{5/2}$ state to the $S_{1/2}$ state Landé g-factors.

The relevant Ra^+ level structure, laser configuration, and quantization field used in this Letter are shown in Fig. 10.1. A single radium-226 ion is loaded by laser ablation of an $\sim$10 μCi $RaCl_2$ target located 15 mm from the center of a linear Paul trap with characteristic dimensions $r_0 = 3$ and $z_0 = 7.5$ mm, see [5]. The radio frequency (rf) trap drive is operated at $\Omega_{\rm rf}/2\pi = 993$ kHz, and for a single radium ion the axial secular frequency is $\omega_z/2\pi = 78.5$ kHz and the radial secular frequencies are $\omega_r/2\pi = 141$ and 156 kHz. Acousto-optic modulators (AOMs) control the frequency and amplitude of all beams during clock operation. Clock state readout is performed by collecting 468 nm photons scattered by the Ra^+ ion onto a photomultiplier tube [6]. As there is no magnetic field shielding around the vacuum apparatus, each clock interrogation cycle is synchronized to the laboratory 60 Hz power line to minimize Zeeman shifts due to magnetic field fluctuations.

Linearly polarized 728 nm light is used to drive the $|S_{1/2}, m = \pm 1/2\rangle \rightarrow |D_{5/2}, m = \pm 1/2\rangle$ (C1), $|S_{1/2}, m = \pm 1/2\rangle \rightarrow |D_{5/2}, m = \pm 3/2\rangle$ (C2), and $|S_{1/2}, m = \pm 1/2\rangle \rightarrow |D_{5/2}, m = \pm 5/2\rangle$ (C3) symmetric Zeeman transitions to operate the clock in a self-comparison mode [135]. By measuring symmetric Zeeman components that comprise all sublevels of the $D_{5/2}$ state ($|m| = 1/2, 3/2, 5/2$), the linear Zeeman shift and the electric quadrupole shift are both canceled [102, 135].

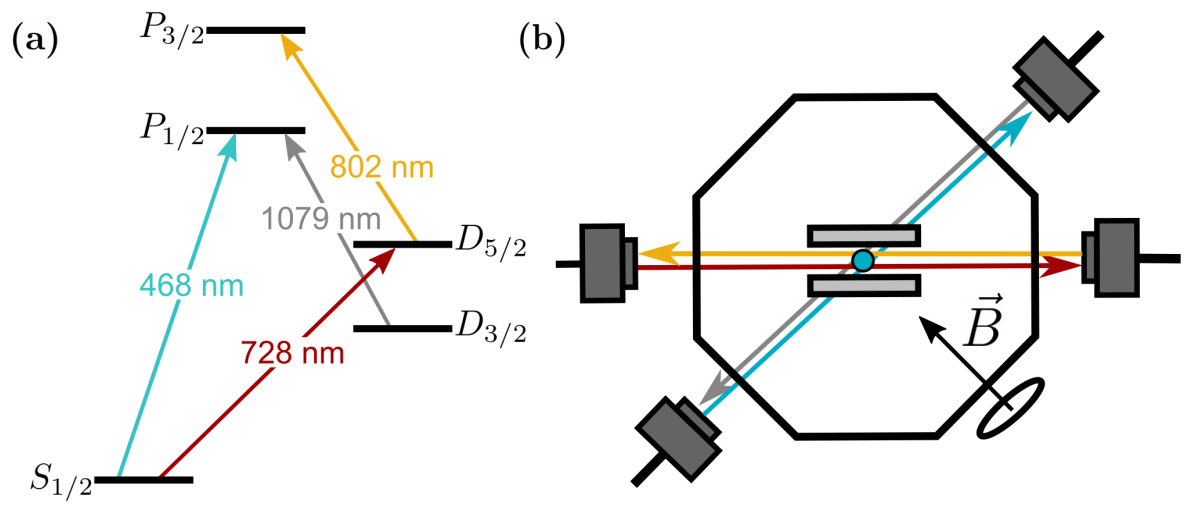

Figure 10.1: (a) The Ra^+ level structure for clock operation. (b) Orientation of the lasers and the magnetic field used in this Letter. The 728 nm clock beam (red) is at 45° with respect to the magnetic field to drive all ten possible Zeeman transitions between the $S_{1/2}$ and $D_{5/2}$ states.

Each clock interrogation cycle begins with an initial state detection (0.5 ms) to determine correct initialization of the population into the $S_{1/2}$ or $D_{3/2}$ laser cooling states. Following the initial state detection, the ion is Doppler cooled (5 ms) and the population is optically pumped to the appropriate $|S_{1/2}, m = \pm 1/2\rangle$ state (2 ms). We then coherently interrogate the clock transition (3 ms) on either the blue- or red-detuned half width at half maximum (HWHM), after which a state detection pulse is applied. In addition to probing the HWHM of the Zeeman transitions to determine the transition center frequency, we also interrogate the peak maximum, as well as six detunings around the peak. For every 20 interrogation cycles of the HWHM and peak maximum, we interrogate the six detunings around the peak to ensure that symmetric Zeeman transitions are probed with equal excitation probabilities and that all transitions remain locked, see Fig. 10.2 inset. To reset the system, we clean out population remaining in the $D_{5/2}$ state by driving the $D_{5/2} \rightarrow P_{3/2}$ dipole transition (200 μs) where decays populate the $S_{1/2}$

and $D_{3/2}$ states.

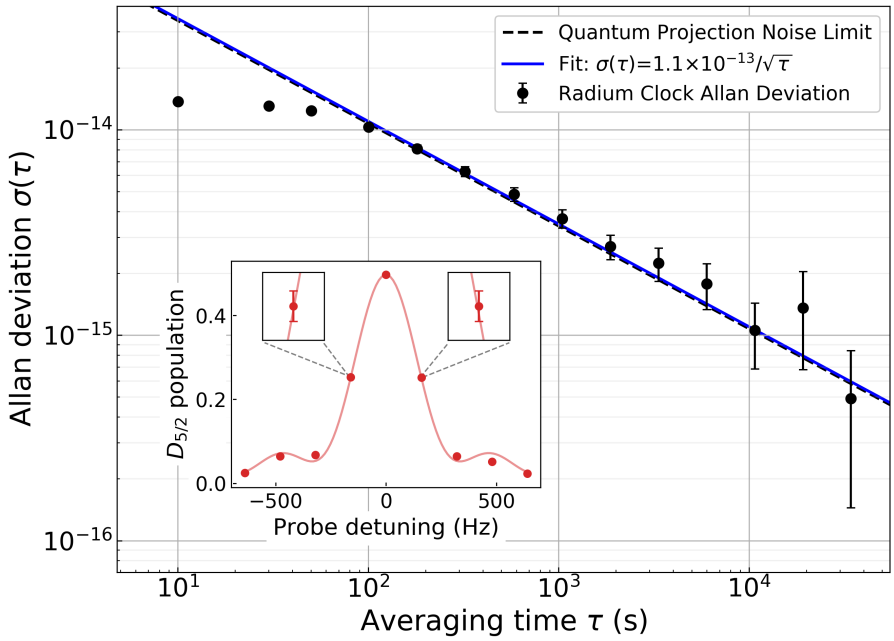

Figure 10.2: Allan deviation of the Ra^+ optical clock measured over ≈100 000 s. The fractional stability (blue line) with a 3 ms interrogation time is $1.1\times10^{-13}/\sqrt{\tau}$. The quantum projection noise limit that accounts for the motional decoherence and line shape is calculated using the method described in [135]. The inset shows the $|S_{1/2}, m = -1/2\rangle \rightarrow |D_{5/2}, m = -1/2\rangle$ Zeeman transition averaged over the entire measurement. The HWHM lock points are magnified by 200× on both axes. Error bars represent one standard deviation. The proportion of the population driven to the excited state is limited by decoherence due to thermal motion. The Fourier-limited linewidth of the measured transition corresponds to a 2.7 ms interrogation time.

After each interrogation cycle, the frequencies of the six Zeeman transitions are updated with individual lock servos to stabilize the clock laser's frequency to the $7s\ ^2S_{1/2} \rightarrow 6d\ ^2D_{5/2}$ atomic resonance. The error signal for an interrogation cycle is given by $E = (n_\mathrm{b} - n_\mathrm{r})/n$, where n_b and n_r are the number of times the population was driven to the excited state during interrogation on the blue- and red-detuned HWHM and $n = 20$ is the total number of interrogations [135]. If the initial state detection determined that the population was in the $D_{5/2}$ state, the interrogation is not used in the error signal calculation. The shift of the center detuning of each Zeeman transition is updated from the

previous detuning using the error signal and the measured drift rate of the optical cavity. Both of these values are updated throughout the experiment based on the shift of the clock transition center frequency, see Supplemental Material [136]. The center frequency of the $7s\ ^2S_{1/2} \rightarrow 6d\ ^2D_{5/2}$ transition is derived from an average of the three Zeeman pairs (C1, C2, and C3) following each interrogation cycle. The total interrogation cycle time for the three pairs of Zeeman transitions is 10 s, where the twenty interrogation cycles of the HWHM and peak maximum takes ~ 6.1 s, the single interrogation cycle of the six detunings around the peak takes ~ 0.6 s, and the pulse programming and data saving takes ~ 3 s.

The measured Ra^+ clock instability is shown in Fig. 10.2. An Allan deviation is obtained from the frequency difference of the three Zeeman pairs, (C1, C2), (C2, C3), and (C1, C3). The average of these three Allan deviations is divided by $\sqrt{6}$ to obtain the self-referenced fractional frequency stability of $\sigma(\tau) = 1.1 \times 10^{-13}/\sqrt{\tau}$, where τ is the averaging time in seconds [135].

A summary of systematic frequency shifts and uncertainties is shown in Table 10.1. The overall frequency instability is currently limited by the clock interrogation time and the dead time in the total interrogation cycle. The 3 ms interrogation time on the clock transition is mainly limited by decoherence due to short-term ambient magnetic field noise. The 728 nm clock laser intensity used to drive a π-pulse with a 3 ms interrogation time is 0.5(3) kW/m^2, which leads to a probe-induced ac Stark shift of $\Delta\nu/\nu = (1.7 \pm 0.9) \times 10^{-15}$. This shift can be reduced by several orders of magnitude by implementing upgrades to the apparatus, such as magnetic field shielding and a trap that can support stronger radial confinement, which would enable interrogation times that approach the $D_{5/2}$ excited state lifetime of $\tau \sim 300$ ms [79]. Additionally, techniques such as hyper-Ramsey spectroscopy [137] or frequency stepping [138] could reduce this shift. All other laser beams (468, 802, 1079 nm) are turned off using double-pass AOMs during

the clock interrogation pulse. To ensure that there is no leakage light present through the AOMs, they are also backed with mechanical shutters (SR474). During each interrogation cycle, the mechanical shutters are closed before the clock laser pulse.

Blackbody radiation generated by the finite temperature of the trapping environment causes an ac Stark shift on the clock transition which depends on the DSSP of the transition and the effective temperature of the BBR at the location of the ion. The BBR-induced frequency shift is evaluated using the theoretical DSSP, $\Delta\alpha_0 = -22.2(1.7)$ a.u. [131] and the effective temperature of the BBR field at the ion's location, $T_{\mathrm{BBR}} = 295(4)$ K [139]. To determine the ambient effective temperature and uncertainty observed by the ion, we measured the maximum temperature differential (3 K) of the vacuum chamber and performed a numerical simulation, using a finite element method, to estimate the maximum temperature rise (0.3 K) of the ion trap due to trap drive heating. The resulting BBR-induced frequency shift is evaluated as $\Delta\nu/\nu = (4.3 \pm 0.4) \times 10^{-16}$. At the current level of precision, the total uncertainty in the BBR shift is dominated by the uncertainty in the DSSP, and, based on previous work in Ca^+ and Sr^+, the dynamic correction to the DSSP is negligible compared to the current theoretical uncertainty [131, 140].

During clock operation, we average the frequencies of symmetric Zeeman pairs to synthesize a clock frequency that is first-order insensitive to magnetic fields. However, we have observed that magnetic field fluctuations at the location of the ion can be significant during the dead time between probing individual transitions in a Zeeman pair. This effect has been observed in previous single ion clocks based on Ca^+ and can lead to a frequency shift due to a residual magnetic field drift between clock probes [141, 142]. The longest dead time between probings of a Zeeman pair is 50 ms, which is largely due to synchronizing the measurement with the 60 Hz ac power line. Given an average magnetic field drift rate of $(0 \pm 7) \times 10^{-13}$ T/s observed in our system, and the maximum Zeeman shift sensitivity among all transitions used, 2.8×10^{10} Hz/T, the pair averaged frequency

shift is estimated to be $\Delta\nu/\nu = (0 \pm 2) \times 10^{-18}$.

Collisions between the Ra^+ ion and background gas molecules (e.g. H_2) can lead to a phase shift during the clock probe pulse. Here, we bound the corresponding clock frequency shift by assuming a worst case estimate of the phase shift of $\pm\pi/2$, which occurs in the middle of a Rabi pulse. In this case, a collision with a background gas molecule leads to a frequency shift of $0.15R_{\text{coll}}$, where R_{coll} is the background gas collision rate [143]. We measure R_{coll} in our trap to be $0.0013(4)\text{s}^{-1}$ using the technique described in [103], which corresponds to a fractional frequency shift due to background gas collisions of $\Delta\nu/\nu = (0 \pm 6) \times 10^{-19}$.

Table 10.1: Fractional frequency shifts ($\Delta\nu/\nu$) and uncertainties of the $^{226}Ra^+$ $7s\ ^2S_{1/2} \rightarrow 6d\ ^2D_{5/2}$ clock.

Effect	Shift	Uncertainty
Clock laser Stark shift	1.7×10^{-15}	9×10^{-16}
Blackbody radiation	4.3×10^{-16}	4×10^{-17}
Magnetic field drift	0	2×10^{-18}
Background gas collisions	0	6×10^{-19}
Secular motion	-6.0×10^{-19}	6×10^{-19}
Excess micromotion	-4.2×10^{-18}	5×10^{-19}
Quadratic Zeeman	4.2151×10^{-16}	1.2×10^{-19}
Electric quadrupole	0	3×10^{-20}
Total	2.5×10^{-15}	9×10^{-16}

Frequency shifts due to ion motion are characterized as that due to excess micromotion (EMM), due to the rf drive, and secular (thermal) motion. Ion motion leads to frequency shifts due to relativistic time dilation and the ac Stark effect [144]. Here, the time-dilation shift is the dominant source of frequency shift and uncertainty and is expressed as $\Delta\nu/\nu = -v^2/(2c^2)$, where v is the speed of the ion in the laboratory frame and c is the speed of light in vacuum. The EMM-induced frequency shift is evaluated by measuring the amplitude of the ion motion at the trap drive frequency, $\Omega_{\text{rf}}/2\pi$ [136]. The frequency shift due to secular motion is evaluated by characterizing

the ion temperature during clock operation [102, 136]. The frequency shift due to secular motion is $\Delta\nu/\nu = (-6.0 \pm 0.6) \times 10^{-19}$, and the EMM-induced frequency shift is $\Delta\nu/\nu = (-3.9 \pm 0.5) \times 10^{-18}$. The clock frequency shifts and uncertainties due to ion motion can be reduced by using an ion trap design that minimizes residual rf fields and supports higher secular motion frequencies. Trap improvements and operation at the "magic" rf drive frequency (6.2 MHz) are expected to reduce both the magnitude and uncertainty of motional frequency shifts [131].

Additional systematic shifts, including the quadratic Zeeman shift and the electric quadrupole shift and their uncertainties are constrained at the low 10^{-19} level (fractional), see the Supplemental Material.

The ratio of Landé g-factors, g_D/g_S, is directly obtained from the clock measurement data [145]. From a single clock measurement, such as shown in Fig. 10.2, we determine three ratios of Landé g-factors from the frequency division of the three Zeeman pairs, see Fig. 10.3 (a). The weighted average of these three ratios gives a value for g_D/g_S. The reported g_D/g_S ratio is calculated from a weighted average of five measurements at different magnetic fields. The assigned uncertainty is the standard deviation of the measurements, resulting in $g_D/g_S = 0.598\,805\,3(11)$, see Fig. 10.3. Because of the rf trapping field, an ac magnetic field is present at the trap frequency, B_{trap}, at the location of the ion, which shifts the measured g_D/g_S [146]. By performing direct spectroscopy of individual Zeeman transitions with the rf trapping frequency set to the ground state magnetic sublevel splitting, we are able to set an upper bound of $B_{\text{trap}} \leq 7 \times 10^{-8}$ T. The systematic shift due to the maximum B_{trap} value is significantly smaller than the statistical uncertainty of g_D/g_S for all magnetic fields where the Landé g-factor ratio was measured. To improve upon this initial measurement, the $S_{1/2}$ state Landé g-factor in Ra^+ could be directly measured to high precision in a Penning trap [147] or in a comparison with a co-trapped ion magnetometer [148], which would, in turn, give the

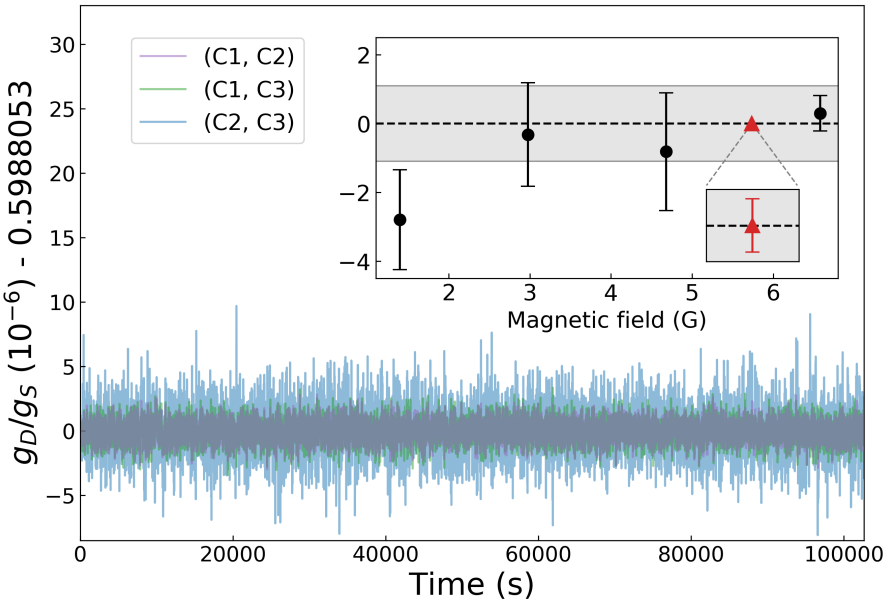

Figure 10.3: The three g-factor ratios calculated from the 3 ms interrogation time clock measurement data presented in Fig. 10.2. The red triangle in the inset represents the weighted average of these data, $g_D/g_S = 0.598\,805\,25(3)$ The circle markers are weighted averages of ∼2000 s of clock data with a 250 μs interrogation time taken at a range of magnetic fields. The shorter interrogation and measurement time results in a larger uncertainty. The gray fill represents the full standard deviation of the five clock measurements, which we assign as the uncertainty for the g-factor ratio measurement.

$D_{5/2}$ state Landé g-factor based on the ratio measured here.

In conclusion, we have demonstrated the operation of a $^{226}Ra^{+}$ ion clock with a total systematic uncertainty of $\Delta\nu/\nu = 9 \times 10^{-16}$ and a frequency instability of $\sigma(\tau) = 1.1 \times 10^{-13}/\sqrt{\tau}$. The current clock performance is primarily limited by (1) short-term magnetic field noise at the ion's location, which limits the clock interrogation time, (2) the uncertainty in the DSSP that dominates the uncertainty in the frequency shift due to BBR, and (3) limitations in the trap design that lead to motional decoherence. The ambient magnetic field noise can be reduced by adding magnetic field shielding, as has been done with $^{40}Ca^{+}$ [141] and $^{88}Sr^{+}$ [102] and motional decoherence can be reduced by using an improved trap design [117, 149]. Reduced magnetic field sensitivity could be realized with radium-225, which has first-order magnetic field insensitive states due to its $I = 1/2$ nuclear spin. The 14.9 day half-life of radium-225 can be overcome by using an oven based on the decay of thorium-229 ($\tau_{1/2} \approx 7340$ y), as demonstrated with a 10 μCi oven source [33]. Such a source promises a long-term *in vacuo* supply of radium-225, as the thorium vapor pressure is more than a trillion times smaller than radium [150], which also makes it robust to inadvertently exhausting the atom supply by running the oven at high temperatures [151]. These features, along with the photonic-technology compatible wavelengths of Ra^{+} and the low optical power requirements of an ion clock make it an intriguing candidate for a transportable optical clock.

10.2 $^{226}Ra^{+}$ Clock Systematics and Additional Information

10.2.1 Clock Measurement Sequence

State Detection: The signal for each interrogation are the 468 nm photons spontaneously emitted by the radium ion, which are collected onto a photomultipler tube (PMT), Hamamatsu H10682-210. During 0.5 ms of state detection 25 photons are collected on average if the population is in the $S_{1/2}$ or $D_{3/2}$ states, and 1.5 photons of background scattered light are collected if the population is shelved in the $D_{5/2}$ clock state. We set the bright-state detection threshold to 5.5 counts.

State Preparation: We simultaneously drive the $|S_{1/2}, m = \mp 1/2\rangle \rightarrow |D_{5/2}, m = \pm 3/2\rangle$, $D_{3/2} \rightarrow P_{1/2}$, and $D_{5/2} \rightarrow P_{3/2}$ transitions to prepare the population in the $|S_{1/2}, m = \pm 1/2\rangle$ state.

Cleanout: To prepare for the next interrogation any population shelved in the clock state is cleaned out with light at 802 nm, where decays from the $P_{3/2}$ state populate the $S_{1/2}$ and $D_{3/2}$ states.

10.2.2 Lock Servo

The individual locking servos update the frequency detuning of each Zeeman transitions by $\Delta\nu$, following,

$$\Delta\nu = GE + r_{\text{cavity}} t_c, \tag{10.1}$$

where $E = (n_b - n_r)/n$ is the error signal defined in the text, G is a gain parameter, t_c is the total interrogation cycle time (10 s), r_{cavity} is the cavity drift rate ($\sim$0.2 Hz/s). The

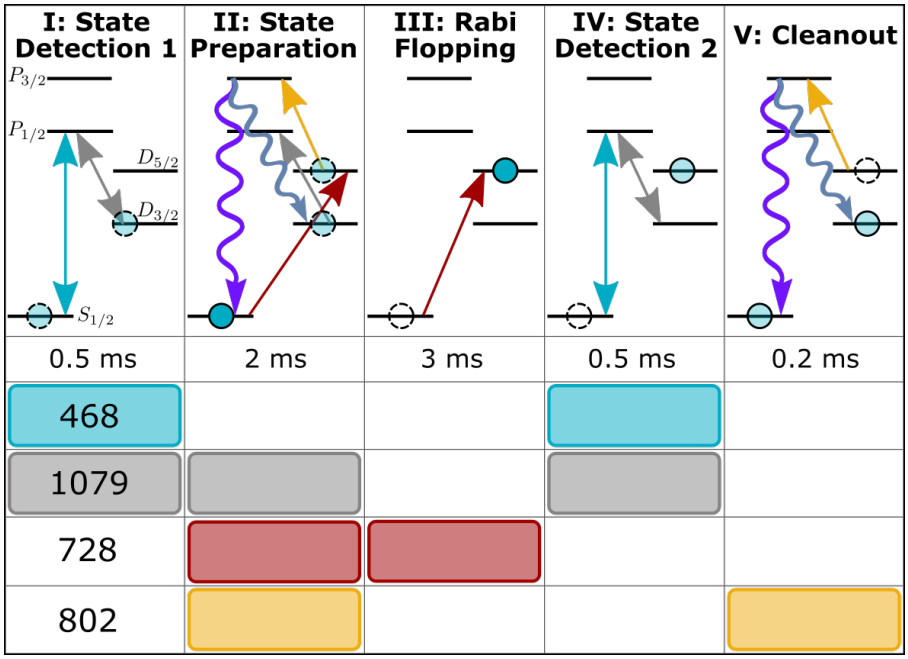

Figure 10.4: The measurement sequence for a single interrogation. There is a 5 ms Doppler cool period after the first state detection which is not shown in the figure. Squiggly lines depict E1 allowed decays, straight lines show optical pumping transitions, and double-arrows indicate optical cycling transitions.

cavity drift rate is updated with the average frequency of all transitions probed using an integral servo, with a time constant of ∼1000 s.

10.2.3 Clock Systematics

Excess micromotion shifts: Second-order Doppler shift

The second-order Doppler shift in fractional form is

$$\frac{\Delta\nu_{\mathrm{D2}}}{\nu_0} = -\left(\frac{\Omega}{\omega_0}\right)^2 \sum_{x,y,z} R_i, \tag{10.2}$$

where ν_0 is the radium clock transition frequency in Hz, Ω is the trap rf drive frequency, $\omega_0 = 2\pi\nu_0$, and $\sum R_i$ is the sum of the micromotion sideband intensity ratios [102]. We use $\nu_0 = 412\,007.701(18)$ GHz [6], $\Omega_{\mathrm{rf}}/2\pi = 993$ kHz, and $\sum R_i = 0.74(8)$, which we

determine from measuring the micromotion sidebands in three near-orthogonal directions. We calculate $\Delta\nu_{\mathrm{D2}} = -1.77(19)$ mHz.

Excess micromotion shifts: Scalar Stark shift

The scalar Stark shift in fractional form is

$$\frac{\Delta\nu_{\mathrm{scalar}}}{\nu_0} = -\frac{\Delta\alpha_0}{\hbar\omega_0}\left(\frac{m\Omega^2 c}{e\omega_0}\right)^2 \sum_{x,y,z} R_i, \tag{10.3}$$

where $\Delta\alpha_0$ is the differential static scalar polarizability and m is the mass of the ion [102]. We use $\Delta\alpha_0 = -22.2(1.7)$ a.u. [131]. We calculate $\Delta\nu_{\mathrm{scalar}} = 0.045(6)$ mHz.

Excess micromotion shifts: Tensor Stark shift

The maximum possible tensor stark shift in fractional form is

$$\frac{\Delta\nu_{\mathrm{tensor}}}{\nu_0} = -\frac{\alpha_2}{\hbar\omega_0}\left(\frac{m\Omega^2 c}{e\omega_0}\right)^2 \sum_{x,y,z} R_i, \tag{10.4}$$

where α_2 is the $D_{5/2}$ state tensor polarizability [102]. We use $\alpha_2(D_{5/2}) = -52.6(5)$ a.u. [131]. We calculate $\Delta\nu_{\mathrm{tensor}} = 0.108(12)$ mHz. We use the sum of the maximum shift and uncertainty, 0.120 mHz, as the uncertainty for this shift.

Thermal motion shift: Second-order Doppler shift

The fractional second-order Doppler shift due to the ion's secular motion is

$$\frac{\Delta\nu_{\mathrm{D2}}}{\nu_0} = -\frac{5kT_{\mathrm{ion}}}{2mc^2}, \tag{10.5}$$

where T_{ion} is the temperature of the ion, and k is the Boltzmann constant [144, 102, 152]. We measured the ion temperature along the axial and radial mode directions by driving

Rabi oscillations on the clock transition and determined an average temperature of $T_{\text{ion}} = 0.6$ mK. We estimate the temperature uncertainty to be 0.6 mK to account for fluctuations in Doppler cooling laser frequencies and any temperature imbalance between different secular motion modes. This measured T_{ion} is consistent with the Doppler cooling limit $T_c = 0.4$ mK. The corresponding frequency shift is $\Delta\nu_{\text{D2}} = -0.3(3)$ mHz.

Thermal motion shift: Scalar Stark shift

The fractional scalar Stark shift due to the ion's thermal motion is

$$\frac{\Delta\nu_{\text{scalar}}}{\nu_0} = -\frac{kT_{\text{ion}}}{mc^2}\frac{\Delta\alpha_0}{\hbar\omega_0}\left(\frac{m\Omega c}{e}\right)^2, \tag{10.6}$$

where T_{ion} is the temperature of the ion [144, 102, 152]. Here, the shift is measured to be $\Delta\nu_{\text{scalar}} = 0.003(3)$ mHz.

Electric quadrupole shift

The electric quadrupole shift is cancelled because we are averaging Zeeman pairs. We can approximate the uncertainty on this cancellation from the electric quadrupole shift magnitude, $A_Q = [\Delta f_Q(m_{j'} = 5/2) - \Delta f_Q(m_{j'} = 1/2)]/6$ [102]. From the frequency difference between shifted pairs we determine the average drift rate of A_Q to be -1.3 μHz/s. Given our cycle time of 10 s we estimate the electric quadrupole shift uncertainty to be 0.013 mHz.

Clock laser ac Stark shift

728 nm: The ac Stark shift due to off-resonant dipole coupling is

$$\Delta\nu_{\text{ac}}(\lambda) = -\frac{\Delta\alpha_{\text{ac}}(\lambda)}{2hc\epsilon_0}I = \kappa(\lambda)I, \tag{10.7}$$

where $\Delta\alpha_{\rm ac}(\lambda) = \Delta\alpha_{\rm ac}(D_{5/2}, \lambda) - \Delta\alpha_{\rm ac}(S_{1/2}, \lambda)$, λ is the laser wavelength and $\kappa(\lambda)$ is the ac Stark shift intensity coefficient [102]. Using $\Delta\alpha_{\rm ac}(D_{5/2}, 728\text{ nm}) = -169(4)$ a.u. and $\Delta\alpha_{\rm ac}(S_{1/2}, 728\text{ nm}) = 140(3)$ a.u. (Private Communications), we calculate $\kappa(728\text{ nm}) = 1.45(2)$ mHz/(W/m^2). We measure the clock laser intensity to be 500(300) W/m^2. The large uncertainty in the clock laser intensity is due to probing all Zeeman transitions with equal contrast, which requires different AOM driving amplitudes. We calculate the clock laser ac Stark shift to be 0.7(4) Hz.

Quadratic Zeeman shift

The quadratic Zeeman shift is caused by the mixing of the $D_{5/2}$ and $D_{3/2}$ sublevels when the ion is exposed to a magnetic field. This shift is

$$\nu_{ZQ} = \langle \nu'_{ZQ}(m_j) \rangle = \frac{2}{15} \left(\frac{[\mu_B B(g_s - 1)]^2}{h^2 \nu_{DD}} \right), \tag{10.8}$$

where B is the magnetic field, $g_S = -g_e$, μ_B is the Bohr magneton, and ν_{DD} is the energy separation between the $D_{5/2}$ and $D_{3/2}$ states [102]. We use a static magnetic field of $B = 0.00057369(8)$ T, and $\nu_{DD} = 49.730\,02(5)$ THz [6]. We calculate $\nu_{ZQ} = 173.66(5)$ mHz.

10.2.4 Evaluation of the Landé g-factor Ratio

From the clock measurement data we calculate three Landé g-factor ratios from the three Zeeman pairs (C1, C2, and C3) defined in the text. For a given Zeeman transition the frequency detuning from the 728 nm transition center is given by

$$\delta = \kappa \frac{g_D}{g_S} m_D - \kappa m_S, \tag{10.9}$$

where $\kappa = g_S \mu_{\rm B} B/h$, and g_S is the ground state Landé g-factor, $\mu_{\rm B}$ is the Bohr magneton, B is the magnetic field, and h is the Planck constant. The C1, C2, and C3 frequency

detunings can be written as

$$\begin{aligned}
\mathrm{C1} &= \delta_{1/2\to 1/2} - \delta_{-1/2\to -1/2} = \kappa\left(\frac{g_D}{g_S} - 1\right) \\
\mathrm{C2} &= \delta_{1/2\to 3/2} - \delta_{-1/2\to -3/2} = \kappa\left(3\frac{g_D}{g_S} - 1\right) \\
\mathrm{C3} &= \delta_{1/2\to 5/2} - \delta_{-1/2\to -5/2} = \kappa\left(5\frac{g_D}{g_S} - 1\right)
\end{aligned}$$

The frequency ratios of C1, C2, and C3 then directly give three Landé g-factor ratios

$$\frac{g_D}{g_S} = \frac{\frac{C1}{C3} - 1}{5\frac{C1}{C3} - 1} = \frac{\frac{C1}{C2} - 1}{3\frac{C1}{C2} - 1} = \frac{\frac{C2}{C3} - 1}{5\frac{C2}{C3} - 3} \tag{10.10}$$

This method cancels out the electric quadrupole shift as C1, C2, and C3 are the frequency differences between symmetric Zeeman transitions.

10.2.5 Autler Townes Shift

When the energy splitting between the ground state Zeeman sublevels, $\omega_S = g_S\mu_\mathrm{B}B_0/\hbar$, equals the rf trapping frequency, $\Omega_\mathrm{rf}/2\pi = 993$ kHz, there is an Autler-Townes splitting ($g_S\mu_\mathrm{B}B_\mathrm{trap}/2\hbar$) of the clock transition due to the trap's magnetic field, B_trap, driving the $|S_{1/2}, m = \pm 1/2\rangle \to |S_{1/2}, m = \mp 1/2\rangle$ transition. To bound B_trap, we set $\Omega_\mathrm{rf} = \omega_S$ within 1 kHz by changing the static magnetic field B_0. We did not observe any splitting at the sub 200 Hz level during direct spectroscopy of individual Zeeman transitions, which indicates that the Rabi frequency due to the trap's magnetic field is not larger than $\sim$1 kHz. Therefore the corresponding B_trap must be no larger than 7×10^{-8} T. The B_trap shifts the Landé g-factor ratio, g_D/g_S, by

$$\frac{g_D}{g_S} = \left[\frac{1 + \frac{1}{2}\frac{\omega_D^2}{\omega_D^2 - \Omega_\mathrm{rf}^2}\frac{\langle B_\mathrm{trap}^2\rangle}{B_0^2}}{1 + \frac{1}{2}\frac{\omega_S^2}{\omega_S^2 - \Omega_\mathrm{rf}^2}\frac{\langle B_\mathrm{trap}^2\rangle}{B_0^2}}\right] \mathrm{r}, \tag{10.11}$$

where $\omega_D = g_D \mu_B B_0/\hbar$ and r is the measured Landé g-factor ratio at the given static magnetic field [145]. The shift in the measured Landé g-factor ratio due to B_{trap} is much smaller than the statistical uncertainty of the measured Landé g-factor ratio.

10.2.6 Clock Cycle

A breakdown of the radium-226 clock cycle is shown in Fig. Timings are rounded for simplicity 10.5.

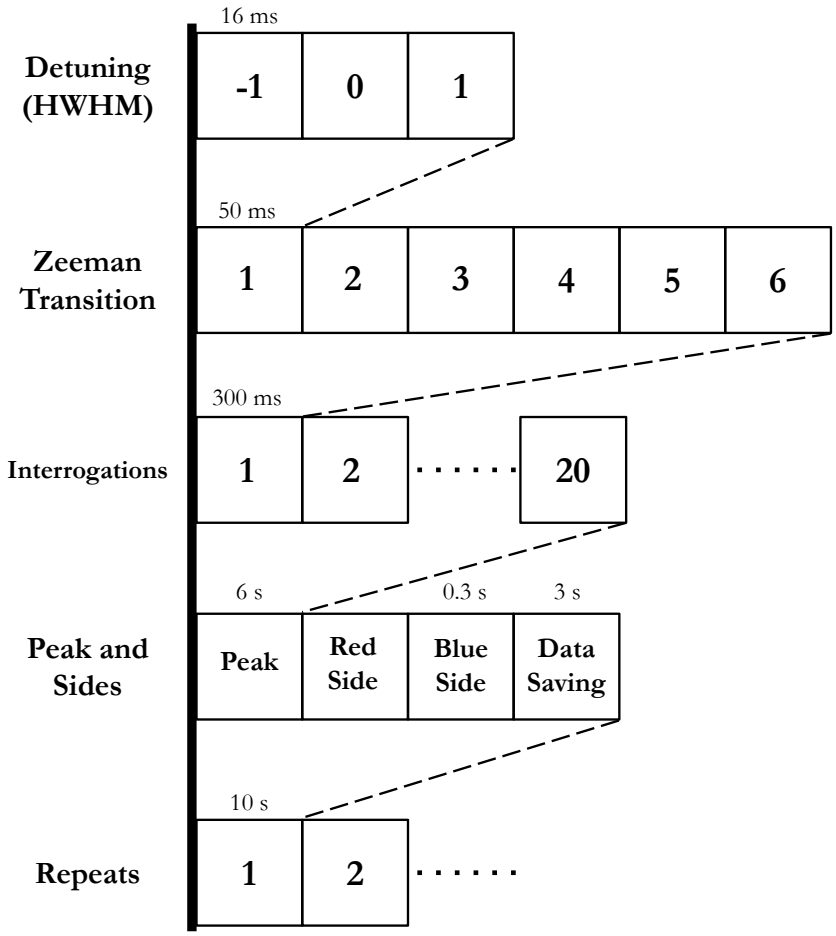

Figure 10.5: Breakdown of the $^{226}Ra^{+}$ clock cycle. Each clock interrogation cycle is synchronized to the laboratory 60 Hz power line to minimize Zeeman shifts due to magnetic field fluctuations. The total interrogation cycle time for the three pairs of Zeeman transitions is 10 s, where the twenty interrogation cycles of the HWHM and peak maximum takes ~ 6.1 s, the single interrogation cycle of the six detunings around the peak takes ~ 0.6 s, and the pulse programming and data saving takes ~ 3 s.

10.3 $^{225}Ra^{+}$ Optical Clock

As described in section 10.1, a $^{225}Ra^{+}$ is promising for its magnetic field insensitive clock transition and straightforward state preparation procedure. Isotope shifts of the 468 nm Doppler cooling transition in the radium ion are known at the MHz level [36], which should quickly enable intial work with the isotope. In this section we detail some of operational aspects of the clock, including laser cooling, state preparation, clock interrogation, and cleanout.

10.3.1 Laser Cooling and State Preparation

Laser cooling of $^{225}Ra^{+}$ can be accomplished by driving the $|S_{1/2}, F = 0\rangle \rightarrow |P_{1/2}, F = 1\rangle$ and $|S_{1/2}, F = 1\rangle \rightarrow |P_{1/2}, F = 1\rangle$ Doppler cooling transitions. If Doppler cooling light

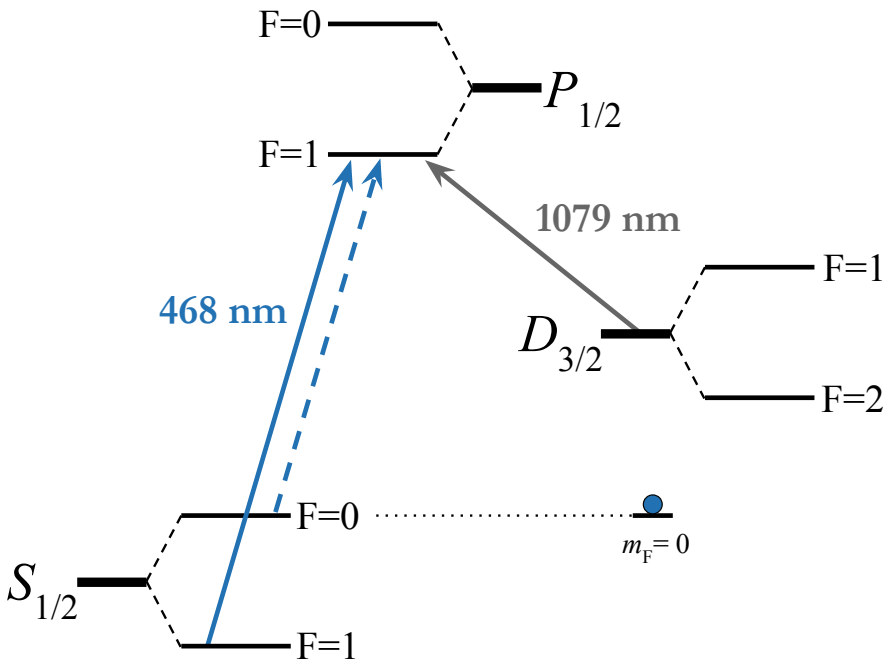

Figure 10.6: Laser cooling and state preparation of $^{225}Ra^{+}$. By turning off the Doppler cooling light driving the $|S_{1/2}, F = 0\rangle \rightarrow |P_{1/2}, F = 1\rangle$ transition (dashed, blue) the population is prepared with high fidelity to $|S_{1/2}, F = 0, m = 0\rangle$ ground state. 1079 nm light (gray) is used to repump decays to the $D_{3/2}$ state.

polarized to drive π transitions is used it will also be necessary to drive the $|S_{1/2}, F = 1\rangle \rightarrow |P_{1/2}, F = 0\rangle$ to clean the population out of the $|S_{1/2}, F = 1, m = 0\rangle$ magnetic sublevel. Any decays to the $D_{3/2}$ state can be repumped by driving the $|D_{3/2}, F = 1\rangle \rightarrow |P_{1/2}, F = 1\rangle$ and $|D_{3/2}, F = 2\rangle \rightarrow |P_{1/2}, F = 1\rangle$ transitions. High-fidelity state preparation to the $|S_{1/2}, F = 0, m = 0\rangle$ magnetic sublevel can be realized by turning off the 468 nm light driving the population out of that state [153], see Fig. 10.6. It may be possible to use a single laser for laser cooling if a 468 nm electro-optic modulator can be driven at the 27.7 GHz ground state hyperfine splitting of radium-225 [35], or if a second-order EOM sideband at 13.85 GHz has sufficient power.

10.3.2 Clock Interrogation and Cleanout

Choice of the clock transition is relatively straightforward for the $^{225}Ra^{+}$ clock. Due to selection rules, the only allowed electric quadrupole transition from the $|S_{1/2}, F = 0, m = 0\rangle$ ground state is the $|S_{1/2}, F = 0\rangle \rightarrow |D_{5/2}, F = 2\rangle$ transition. Because the $m_F = 0 \rightarrow m_{F'} = 0$ transitions are insensitive to the first-order Zeeman shift we will drive to the $|D_{5/2}, F = 2, m = 0\rangle$ magnetic sublevel. Following state detection of the population, which will use the same transitions as laser cooling, the $|D_{5/2}, F = 2\rangle \rightarrow |P_{3/2}, F = 1\rangle$ transition can be driven to reset the population to the $S_{1/2}$ or $D_{3/2}$ state. Because the $|D_{5/2}, F = 3\rangle \rightarrow |P_{3/2}, F = 1\rangle$ transition is electric dipole forbidden we do not have to worry about driving that transition.

10.3.3 Other Considerations

For the $^{226}Ra^{+}$ optical clock, the electric quadrupole shift is canceled by averaging over 6 Zeeman transitions that contain all magnetic sublevels in the $D_{5/2}$ state [7]. However, because only a single Zeeman transition $|S_{1/2}, F = 0, m = 0\rangle \rightarrow |D_{5/2}, F = 2, m = 0\rangle$

transition is driven in the $^{225}Ra^{+}$ optical clock, an alternative method is needed to deal with the electric quadrupole shift. The electric quadrupole shift would otherwise lead to considerable uncertainty in the error budget, due to the large radium $D_{5/2}$ state quadrupole moment $\Theta = 4.59(9)ea_0^2$ [37]. To cancel the electric quadrupole shift in ion species with nuclear spin $I > 0$, it is possible to measure the clock transition in three mutually orthogonal magnetic field quantization axes [154], as is done for the Hg^{+} [155] and Yb^{+} (E2) ion clocks [156]. Exceptions to this requirement are the Al^{+} [157] and Yb^{+} (E3) [158] ion clocks, which have exceptionally small quadrupole moments.

Other systematics for the $^{225}Ra^{+}$ optical clock are similar in nature and magnitude to that of the $^{226}Ra^{+}$ optical clock, and should be straightforward to address and measure.

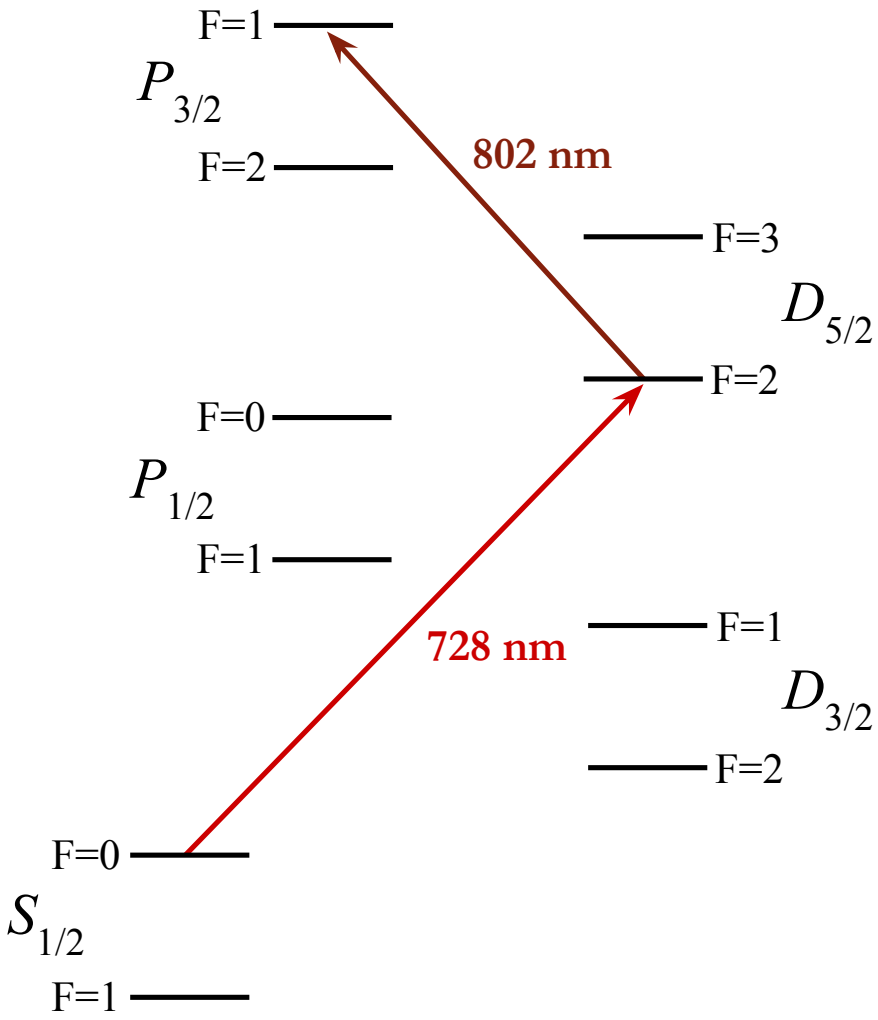

Figure 10.7: Clock interrogation and cleanout of $^{225}Ra^{+}$. 728 nm light (red) drives the $|S_{1/2}, F = 0, m = 0\rangle \rightarrow |D_{5/2}, F = 2, m = 0\rangle$ clock transition. 802 nm light (dark red) drives the $|D_{5/2}, F = 2\rangle \rightarrow |P_{3/2}, F = 1\rangle$ cleanout transition.

Chapter 11

A Strontium Ion Optical Clock

11.1 Motivation

The high nuclear spin $I = 9/2$ of $^{87}Sr^{+}$ makes the ion an interesting candidate for an optical clock [159]. Similar to the proposed $^{43}Ca^{+}$ ion optical clock [160], which has nuclear spin $I = 7/2$, the $^{87}Sr^{+}$ ion's numerous hyperfine and magnetic sublevels result in several possibilities for clock transitions that have a reduced sensitivity to environmental perturbations. In addition, the strontium ion wavelengths are far from the UV, which make the ion promising for an integrated photonics transportable clock. Work with $^{87}Sr^{+}$ is straightforward if one has an existing $^{88}Sr^{+}$ ion trapping system. ^{87}Sr is stable and has a natural abundance of 7%, which makes it possible to work with the isotope without the need for an enriched atomic source. Because the ground state hyperfine splitting is only 5 GHz [24], it is possible to laser cool the ion with an electro-optic modulator, without the need for a second Doppler cooling laser. As such, work with the ion only requires a change in the Doppler cooling and repump frequencies compared to $^{88}Sr^{+}$, see Fig. 11.1.

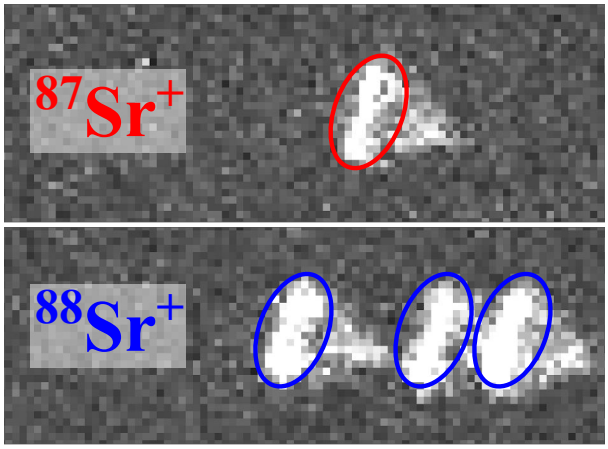

Figure 11.1: Co-trapped $^{87}Sr^{+}$ (top, red) and $^{88}Sr^{+}$ (bottom, blue). By detuning the Doppler cooling and repump laser frequencies we can control which isotope is bright.

11.2 Laser Cooling

Laser cooling of $^{87}Sr^{+}$ can be realized in several ways. We describe a laser cooling scheme that is most adaptable to realizing high-fidelity state preparation to the $|S_{1/2}, F = 4, m = 0\rangle$ state. We describe the state preparation in the following section.

A single 422 nm EOM is needed for Doppler cooling of $^{87}Sr^{+}$. The center frequency of the 422 nm light through the EOM should be resonant with the $|S_{1/2}, F = 5\rangle \rightarrow |P_{1/2}, F = 5\rangle$ transition. Two rf tones should then be driven on the EOM: one at the frequency separation between the $|S_{1/2}, F = 5\rangle \rightarrow |P_{1/2}, F = 5\rangle$ and $|S_{1/2}, F = 5\rangle \rightarrow |P_{1/2}, F = 4\rangle$ transitions (0.87 GHz), and the other at the frequency separation between the $|S_{1/2}, F = 5\rangle \rightarrow |P_{1/2}, F = 5\rangle$ and $|S_{1/2}, F = 4\rangle \rightarrow |P_{1/2}, F = 4\rangle$ transitions (4.13 GHz). The two tones can be combined on a power splitter/combiner from the direct digital synthesizer sources, and will also drive the $|S_{1/2}, F = 4\rangle \rightarrow |P_{1/2}, F = 5\rangle$ transition when driven simultaneously.

A single 1092 nm EOM is needed for repumping decays to the $D_{3/2}$ state. The center frequency through the EOM should be resonant with the $|D_{3/2}, F = 5\rangle \rightarrow |P_{1/2}, F = 5\rangle$ transition. Two tones should be driven on the EOM, one at 240 MHz to drive the

$|D_{3/2}, F = 4\rangle \rightarrow |P_{1/2}, F = 5\rangle$ and $|D_{3/2}, F = 6\rangle \rightarrow |P_{1/2}, F = 5\rangle$ transitions, and one at 430 MHz to drive the $|D_{3/2}, F = 3\rangle \rightarrow |P_{1/2}, F = 4\rangle$ transition. The second tone might not be necessary because the higher order sideband from the 240 MHz tone might sufficiently drive the $|D_{3/2}, F = 3\rangle \rightarrow |P_{1/2}, F = 4\rangle$ transition depending on the laser intensity.

11.3 State Preparation

State preparation of nuclear spin $I > 1/2$ ions can be realized to the $|S_{1/2}, F = 4, m = 0\rangle$, $|S_{1/2}, F = 5, m = 0\rangle$, or $|S_{1/2}, F = 5, m = \pm 5\rangle$ state. We describe the state preparation protocols in the following subsections.

11.3.1 State Preparation to $m_F = 0$

State preparation to a $m_F = 0$ magnetic sublevel in the $S_{1/2}$ ground state can be realized with Doppler cooling light polarized to drive π transitions, see Fig. 11.2. By only driving one of the Doppler cooling EOM tones used for laser cooling at a time, the population can be prepared to the $|S_{1/2}, F = 4, m = 0\rangle$ state with high fidelity as demonstrated by work with the $^{137}Ba^{+}$ qubit [3]. Because Doppler cooling light polarized to drive π transitions is used, the $|S_{1/2}, F = 5, m = 0\rangle \rightarrow |P_{1/2}, F = 5, m = 0\rangle$ and $|S_{1/2}, F = 4, m = 0\rangle \rightarrow |P_{1/2}, F = 4, m = 0\rangle$ transitions are forbidden by electric dipole selection rules. The $|S_{1/2}, F = 5\rangle \rightarrow |P_{1/2}, F = 5\rangle$ and $|S_{1/2}, F = 5\rangle \rightarrow |P_{1/2}, F = 4\rangle$ transitions are driven to clear errors out of the $|S_{1/2}, F = 5\rangle$ hyperfine level, while the $|S_{1/2}, F = 4\rangle \rightarrow |P_{1/2}, F = 4\rangle$ transitions clears errors out of the $|S_{1/2}, F = 4\rangle$ hyperfine level. The 0.87 GHz and 4.13 GHz EOM tones must be driven one at a time, stroboscopically, to avoid driving the $|S_{1/2}, F = 4\rangle \rightarrow |P_{1/2}, F = 5\rangle$ transition, which would clean out population from the desired $|S_{1/2}, F = 4, m = 0\rangle$ state.

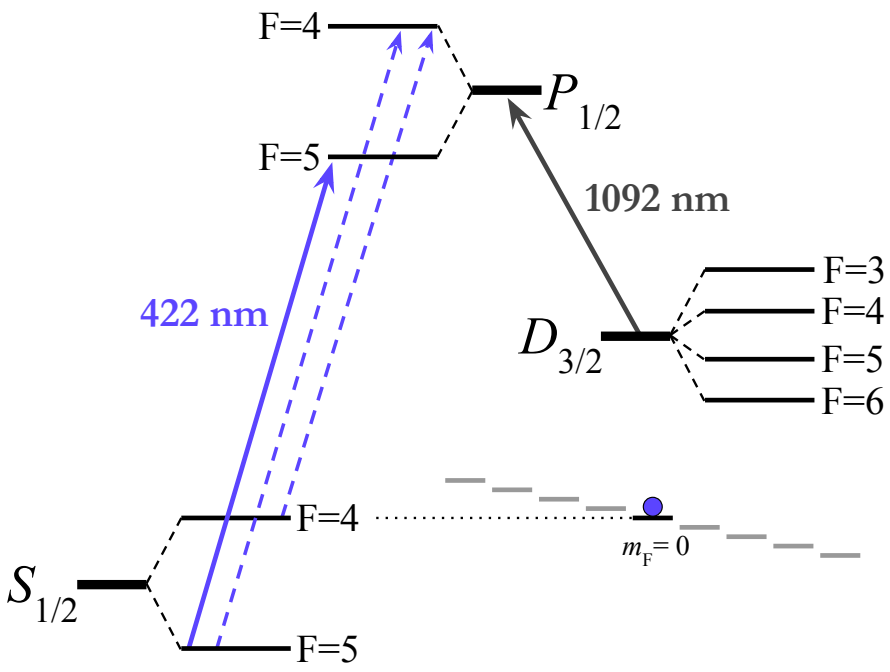

Figure 11.2: High-fidelity state preparation to the $|S_{1/2}, F = 4, m = 0\rangle$ ground state in $^{87}Sr^{+}$. Doppler cooling 422 nm light polarized to drive π transitions drives the $|S_{1/2}, F = 5\rangle \rightarrow |P_{1/2}, F = 5\rangle$ transition (solid blue), and with the aid of an EOM stroboscopically drives the $|S_{1/2}, F = 5\rangle \rightarrow |P_{1/2}, F = 4\rangle$ and $|S_{1/2}, F = 4\rangle \rightarrow |P_{1/2}, F = 4\rangle$ transitions (dashed blue). 1092 nm light repumps any population that decays to the metastable $D_{3/2}$ state.

To prepare the population to the $|S_{1/2}, F = 5, m = 0\rangle$ state the center EOM frequency would need to be resonant with the $|S_{1/2}, F = 4\rangle \rightarrow |P_{1/2}, F = 4\rangle$ transition, and the sidebands would need to stroboscopically drive the $|S_{1/2}, F = 4\rangle \rightarrow |P_{1/2}, F = 5\rangle$ and $|S_{1/2}, F = 5\rangle \rightarrow |P_{1/2}, F = 5\rangle$ transitions.

11.3.2 State Preparation to $m_F = \pm 5$

State preparation to the $|S_{1/2}, F = 5, m = 5\rangle$ magnetic sublevel can be realized with Doppler cooling light polarized to drive π and σ^+ transitions, see Fig. 11.3. In this protocol, two different Doppler cooling 422 nm beams would be needed to drive π and σ^+ transitions. Because there are two $\sigma^{\pm}$-polarized transitions, it makes sense to use

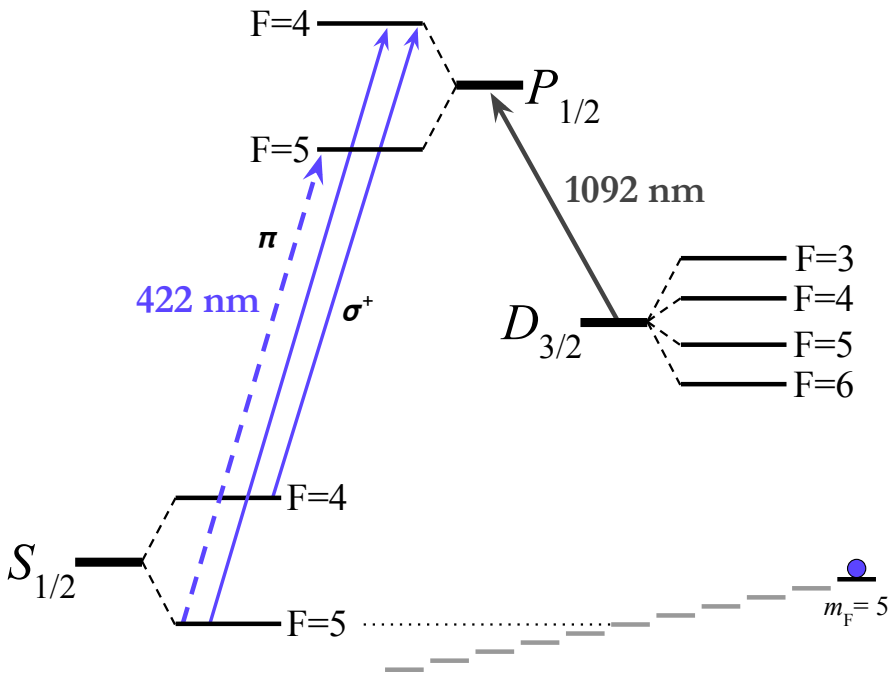

Figure 11.3: Polarization state preparation to a stretched state. By turning off the Doppler cooling light polarized to drive π transitions that is driving the $|S_{1/2}, F = 5\rangle \rightarrow |P_{1/2}, F = 5\rangle$ transition, the Doppler cooling light polarized to drive σ^+ transitions that is driving the $|S_{1/2}, F = 5\rangle \rightarrow |P_{1/2}, F = 4\rangle$ and $|S_{1/2}, F = 4\rangle \rightarrow |P_{1/2}, F = 4\rangle$ transitions (solid blue) will prepare the population to the $|S_{1/2}, F = 5, m = 5\rangle$ ground state with high fidelity. 1092 nm light repumps any population that decays to the metastable $D_{3/2}$ state.

an EOM to drive the $|S_{1/2}, F = 4\rangle \rightarrow |P_{1/2}, F = 4\rangle$ and $|S_{1/2}, F = 5\rangle \rightarrow |P_{1/2}, F = 4\rangle$ transitions. By turning off the Doppler cooling light polarized to drive π transitions the $|S_{1/2}, F = 5\rangle \rightarrow |P_{1/2}, F = 5\rangle$ transition the population will have no way to be driven out of the $|S_{1/2}, F = 5, m = \pm 5\rangle$ magnetic sublevel because of electric dipole selection rules. This method was demonstrated with $^{43}Ca^+$ and over 95% state preparation fidelity was observed after 10μs [161, 162].

To prepare the population to the $|S_{1/2}, F = 5, m = -5\rangle$ state Doppler cooling light polarized to drive π and σ^- transitions would be needed to drive the $|S_{1/2}, F = 4\rangle \rightarrow |P_{1/2}, F = 4\rangle$ and $|S_{1/2}, F = 5\rangle \rightarrow |P_{1/2}, F = 4\rangle$ transitions. Because there are fewer magnetic sublevels in the $|S_{1/2}, F = 4\rangle$ hyperfine level compared to the $|S_{1/2}, F = 5\rangle$

hyperfine level, it is not readily possible to prepare the population into those stretched states.

11.4 Hyperfine Splitting

To determine the $S_{1/2}$ and $D_{5/2}$ state hyperfine splittings it is necessary to solve the Breit-Rabi Hamiltonians,

$$H_{\text{hfs}}^{S_{1/2}} = hA_{S_{1/2}}\mathbf{I}\cdot\mathbf{J} \tag{11.1a}$$

$$H_{\text{hfs}}^{D_{5/2}} = hA_{D_{5/2}}\mathbf{I}\cdot\mathbf{J} + hB_{D_{5/2}}\frac{3(\mathbf{I}\cdot\mathbf{J})^2 + \frac{3}{2}(\mathbf{I}\cdot\mathbf{J}) - I(I+1)J(J+1)}{2I(2I-1)J(J-1)}, \tag{11.1b}$$

where h is Planck's constant and $A_{D_{5/2}}(A_{S_{1/2}})$ and $B_{D_{5/2}}$ are the state hyperfine constants. In a nonzero magnetic field the Hamiltonian in equation 11.1 is replaced by,

$$H^{(D_{5/2})} = H_{\text{hfs}}^{D_{5/2}} + g_{D_{5/2}}\mu_B\mathbf{J}\cdot\mathbf{B} + g_I^{'}\mu_B\mathbf{I}\cdot\mathbf{B}, \tag{11.2}$$

where $g_{D_{5/2}}$ is the electronic g factor of the $D_{5/2}$ state and $g_I^{'}$ denotes the nuclear g factor [161]. We use the AtomicDensityMatrix package in Mathematica to diagonalize these Hamiltonians and to save the data across a range of magnetic fields, see Fig. 11.4 and Fig. 11.5. We then analyze the saved data from Mathematica in Python. We found that when we evaluated the eigenstates at a particular magnetic field that certain magnetic sublevels actually exist to a small extent in a superposition with other levels. This effect is more pronounced in the $D_{5/2}$ state magnetic sublevels with the exception of stretched states or the $m_F = 0$ magnetic sublevel in a given excited state hyperfine level.

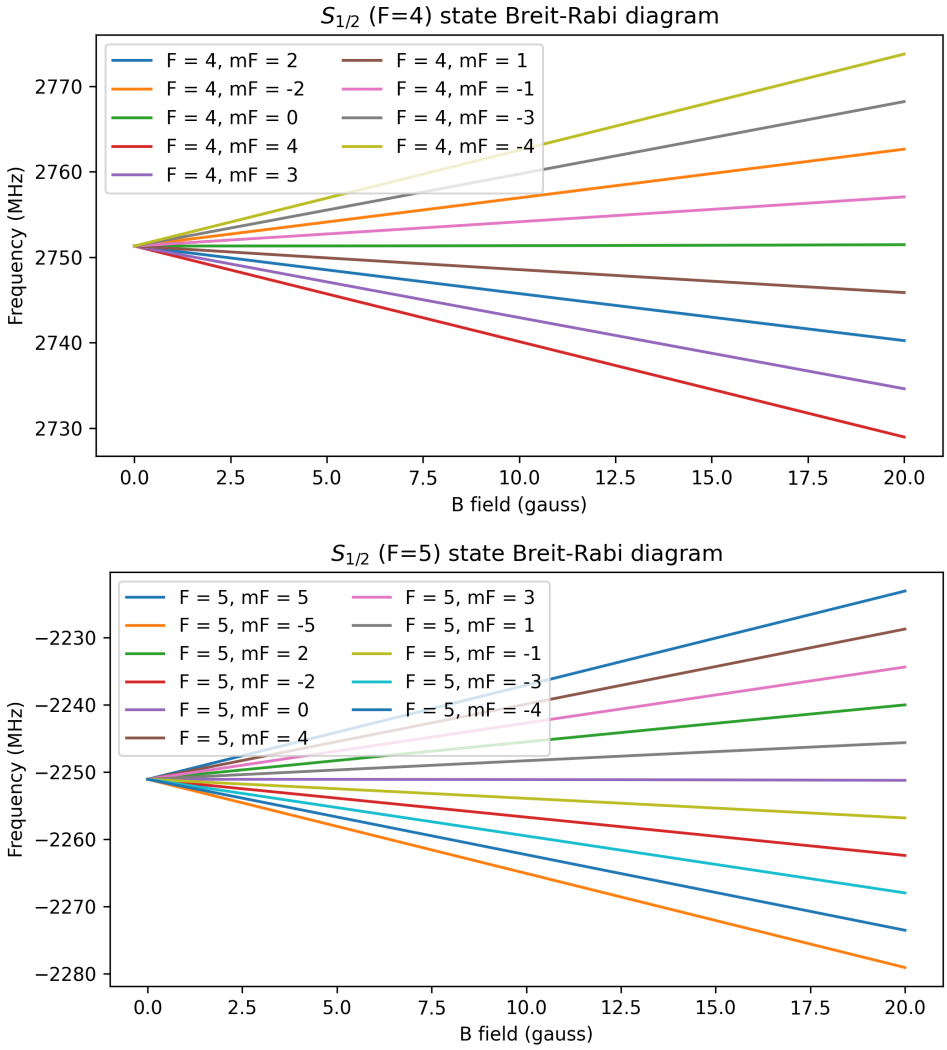

Figure 11.4: Zeeman shifts of the $S_{1/2}$ state hyperfine levels of $^{87}Sr^{+}$.

11.5 Choice of Clock Transition

With 20 magnetic sublevels in the $S_{1/2}$ ground state and 60 magnetic sublevels in the $D_{5/2}$ state, there are a rather large number of possible clock transitions to choose from. If one selects a straightforward state preparation protocol described above, the choice of clock transitions are narrowed down to those originating from the $|S_{1/2}, F = 4, m = 0\rangle$, $|S_{1/2}, F = 5, m = 0\rangle$, or $|S_{1/2}, F = 5, m = \pm 5\rangle$ state. This narrows down the selection

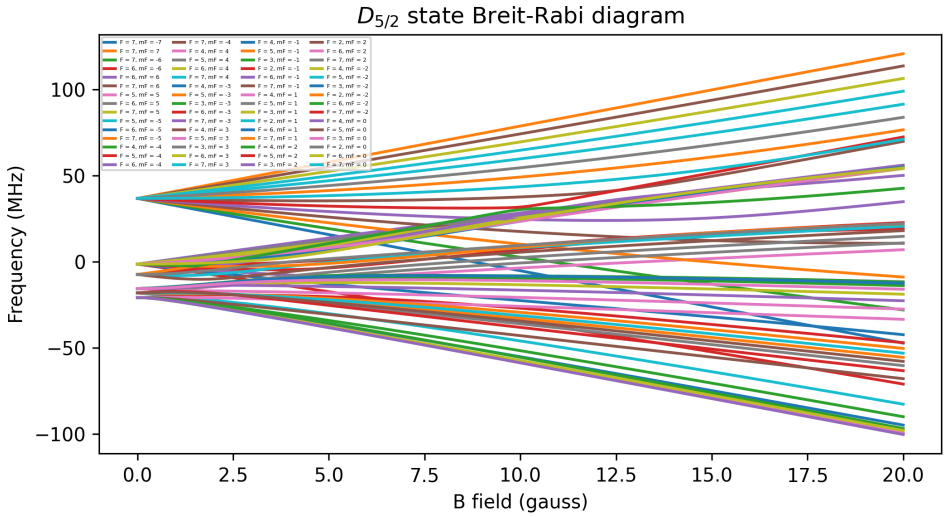

Figure 11.5: Zeeman shifts of the $D_{5/2}$ state hyperfine levels of $^{87}Sr^{+}$. A legend showing the 60 different magnetic sublevels is included primarily for comedic purposes.

somewhat, but choosing the desired transition is still dependent on the clock application. We describe two different applications, and the respective transitions that may be suitable in the following subsections.

11.5.1 Transportable System

Key considerations for a transportable system are magnetic field insensitivity and the technical limitations of the setup. For example, if state preparation was done to a stretched state, another 422 nm Doppler cooling beam and port would be required. This makes preparing to a ground state $m_F = 0$ magnetic sublevel desirable for a transportable setup. Similar to the $^{225}Ra^{+}$ optical clock, to cancel the electric quadrupole shift it would be necessary to measure the clock transition in three mutually orthogonal directions [154]. However, another possibility exists for the $^{87}Sr^{+}$ ion clock. The electric quadrupole shift Δf_Q is defined as

$$\Delta f_Q = \frac{1}{4}\nu_Q(3\cos^2\theta - 1)\left(m_{j'}^2 - \frac{J'(J'+1)}{3}\right), \tag{11.3}$$

where ν_Q is a characteristic frequency shift proportional to the electric field gradient and the electric quadrupole moment, θ is the angle between the electric field gradient principal axis and the quantization axis defined by the applied magnetic field, and $m_{J'}$ is the magnetic sublevel where J' is the hyperfine level [102]. As such, because the $S_{1/2}$ state has no quadrupole moment, and if the $D_{5/2}$ state chosen has $J' = 3$ and $m_{J'} = \pm 2$, there will be no electric quadrupole shift for the $|S_{1/2}, F = 4, m = 0\rangle \rightarrow |D_{5/2}, F = 3, m = \pm 2\rangle$ or $|S_{1/2}, F = 5, m = 0\rangle \rightarrow |D_{5/2}, F = 3, m = \pm 2\rangle$ transitions.

We plot the frequency shifts in a magnetic field for selected clock transitions in Fig. 11.6. The top plot shows some of the most magnetic field insensitive transitions for transitions that originate from the $|S_{1/2}, F = 4, m = 0\rangle$ ground state, which is easiest to prepare the population to because of the fewer magnetic sublevels compared to the $|S_{1/2}, F = 5\rangle$ hyperfine level. Fortuitously, among these transitions is the $|S_{1/2}, F = 4, m = 0\rangle \rightarrow |D_{5/2}, F = 3, m = 2\rangle$ transition, which also happens to be first order magnetic field insensitive. This transition would be able to realize a high-performance optical clock with minimal technical challenges. Eliminating the electric quadrupole shift is helpful for lower the total systematic uncertainty of the clock. After the uncertainty in blackbody radiation shift, the uncertainty in the electric quadrupole shift is the largest systematic effect in the Yb^+ (E2) clock [2]. Some consideration would need to made for cancelling the linear Zeeman shift, but that could be accomplished by also driving the $|S_{1/2}, F = 4, m = 0\rangle \rightarrow |D_{5/2}, F = 3, m = -2\rangle$ transition.

11.5.2 Lab System

We assume for a lab system that technical challenges such as adding additional beams can easily be addressed. Thus, the only consideration for the clock is choosing the transitions that have the lowest sensitivity to first-order and quadratic Zeeman shifts.

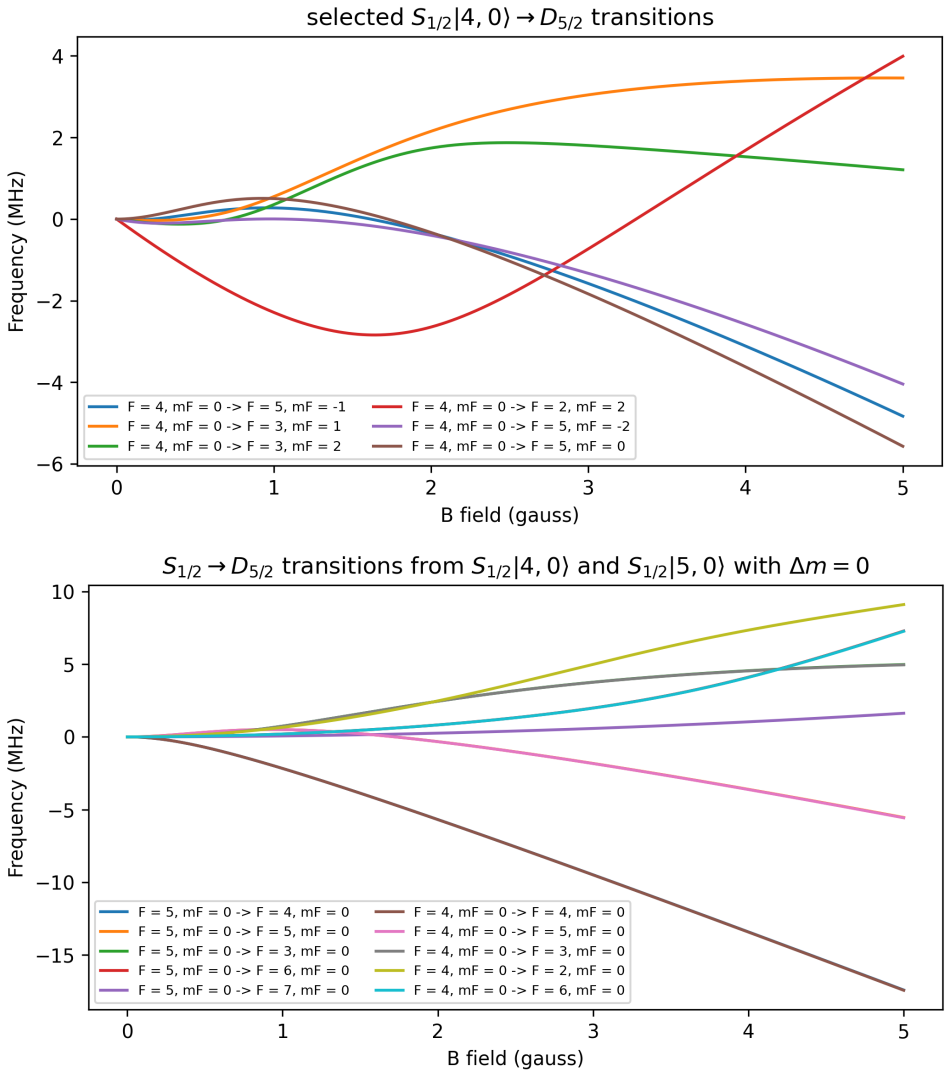

Figure 11.6: Selected $^{87}Sr^{+}$ clock transitions. The top plot shows some of the most magnetic field insensitive transitions that originate from the $|S_{1/2}, F = 4, m = 0\rangle$ ground state. The bottom plot shows some of the most magnetic field insensitive field transitions to the $|S_{1/2}, F = 4, m = 0\rangle$ or $|S_{1/2}, F = 5, m = 0\rangle$ state with $\Delta m = 0$.

It is understood that $m_F = 0 \rightarrow m_{F'} = 0$ transitions are insensitive to the first-order Zeeman shift. So if we start from there, we only need to consider the quadratic shift of the $D_{5/2}$ state $m_F = 0$ sublevels which are much larger than those of the $S_{1/2}$ ground state. The quadratic Zeeman shifts for the $D_{5/2}$ state $m_F = 0$ sublevels were calculated in [28], and are shown in Table 11.1.

Table 11.1: Quadratic Zeeman shifts for the $|D_{5/2}, F, m = 0\rangle$ magnetic sublevels. Shifts were calculated in [28].

Level ($\|F, 0\rangle$)	Quadratic Zeeman shift (Hz/μT^2)
2	67
3	56
4	-341
5	189
6	20
7	6.4

We can see from Table 11.1 that the quadratic Zeeman shift of the $|D_{5/2}, F = 7, m = 0\rangle$ magnetic sublevel is considerably lower than those of other hyperfine levels. Due to selection rules, the only $\Delta m = 0$ transition that then exists is the $|S_{1/2}, F = 5, m = 0\rangle \rightarrow |D_{5/2}, F = 7, m = 0\rangle$, which was proposed by [28] for frequency standard applications. The quadratic Zeeman shift in the Yb^+ (E2) ion clock was measured to be 52.13(9) Hz/μT^2 [163]. This shift is in agreement with the calculated value 52.096(16) Hz/μT^2 [164]. In the current state-of-the-art Yb^+ (E2) ion clock this contributes a fractional frequency shift and uncertainty of $463(3) \times 10^{-18}$ to the uncertainty budget. Because the quadratic Zeeman shift of the $|S_{1/2}, F = 5, m = 0\rangle \rightarrow |D_{5/2}, F = 7, m = 0\rangle$ is approximately two orders of magnitude larger than that of the Yb^+ (E2) ion clock it will be important to have robust magnetic field control.

11.5.3 Other Considerations

As pointed out by Benhlem, *et al.* [161], it is important to consider the trap drive frequency of the system. The separation between magnetic sublevels in the $D_{5/2}$ is of the same magnitude as typical trap drive frequencies, which could drive unwanted transitions and give rise to large ac-magnetic level shifts.

Chapter 12

Future Clock Directions

I once asked a professor who is working towards compact transportable optical clocks if they were more interested in transportable optical clocks for new physics searches or to improve global positioning systems. They replied, "*Both! If there is new physics, the transportable clocks will detect it, and if not we can improve global positioning systems.*" At first I figured the answer was an easy way out of hard question, but the more I thought it, the more I realized the answer was correct. Any transportable optical clock, that is robust enough to be deployed on a ship, plane, or even satellite will have an immediate and lasting impact on a wide range of science and engineering applications, including searches for new physics. The challenging aspect is making transportable systems more compact and able to be run autonomously, with operational lifetimes that justify the cost of deployment. This chapter describes a proposal for reducing photonic-related requirements, one of the most significant technical challenges for transportable trapped ion clocks, by reducing the number of lasers required for operation to three or even two.

12.1 Three-level Ion Optical Clocks

This section includes the contents of a work in preparation, *Three-level ion optical clocks*.

To reduce complexity and increase system robustness we propose an optical clock with trapped alkaline-earth-like ions that use only three electronic states for clock operation. Compared to traditional single ion clocks this reduces the number of lasers required. The proposed clock uses hyperfine levels for clock readout operations and therefore requires nuclear spin $I > 0$. The primary limitation for such a clock is due to state detection errors from off-resonant scattering events. In general, large hyperfine splittings reduce state detection errors, making systems with large nuclei appealing for realizing a three-level clock. We consider the $^{225}Ra^{+}$ ion as a candidate system for a three-level clock, and discuss the potential to help realize a transportable optical clock.

12.1.1 Introduction

Transportable optical clocks are promising for tests of Einstein's equivalence principle [114], searches for dark matter [124], and improved timekeeping and global positioning systems [113]. In combination with clock networks on Earth, optical clocks on satellites would improve limits on the accuracy of intercontinental frequency transfer and comparison, and aid deep space navigation [4, 1]. However, there is a gap between existing state-of-the-art optical clocks and the desired turn-key systems that can be deployed, or even run autonomously, e.g. as part of an advanced global positioning system network. Generation, control, and delivery of laser light with integrated photonics is desirable for such advanced clocks. The use of integrated photonics is promising for achieving smaller clock form factors and system robustness, where optical alignment can be lithographically

defined. Integrated photonics may further enhance magnetic field shielding by reducing vacuum system windows. This enhancement could be important in satellite orbit where the magnetic field variation is more than 100 times the variation seen on earth [4]. We propose optical clock systems that require fewer lasers, which should reduce the barriers for realizing a clock with integrated photonics.

Clocks based on trapped ions are a potential path towards robust transportable optical clocks. Ion traps use electromagnetic potentials which result in long storage times, and clock operation only needs low-power lasers. In realizations with candidate systems Ca^+ and Sr^+ [16, 17], the excited clock state is separate from the states used for laser cooling and state detection, and an additional laser is needed to reset the electronic population between clock interrogations [165, 141]. In total, five electronic states are used along with four laser wavelengths for these relatively simple clocks. To further ease requirements for the use of integrated photonics, the number of required lasers can be reduced from four to three, or possibly only two lasers with optical clocks based on three-level Λ systems.

Alkaline-earth-like ions with nuclear spin $I > 0$ can realize clock operation in a three-level Λ system by using their hyperfine structure. In the proposed scheme only three electronic transitions are driven: the $S_{1/2} \rightarrow D_{3/2}$ clock transition, the $S_{1/2} \rightarrow P_{1/2}$ Doppler cooling transition, and the $D_{3/2} \rightarrow P_{1/2}$ repump transition, see the levels in our example system Fig. 12.1. Similar to the $^{171}Yb^+$ [174] and $^{199}Hg^+$ [175] clocks, alkaline-earth-like ions with nuclear spin $I > 0$ have magnetic field insensitive clock transitions and can be directly laser cooled [28, 161, 176]. In these protocols state detection, which determines if the clock transition was driven, relies on detecting population in distinct hyperfine levels due to the interconnectedness of the electronic Λ structure [153]. Off-resonant scattering limits the state detection fidelity, and we calculate these state detection errors for candidate clock ions. Larger hyperfine splittings result in lower state detection errors due to off-resonant scattering. For species with large hyperfine splittings,

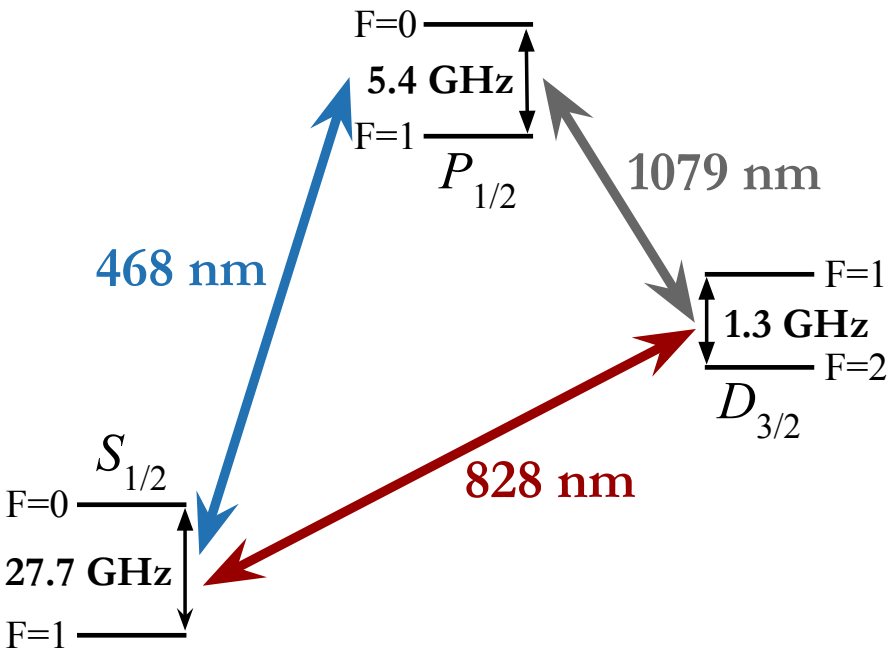

Figure 12.1: The $^{225}Ra^{+}$ level structure for clock operation showing the Doppler cooling (blue), repump (gray), and clock (red) transitions. Hyperfine splittings of the states are shown.

generally heavy atoms, the clock performance is not limited by state detection errors. We consider such a heavy ion, $^{225}Ra^{+}$, as an example system for a three-level clock, and discuss its potential to realize a transportable clock.

12.1.2 Clock Operation

Four steps constitute a three-level ion optical clock measurement sequence: laser cooling, state preparation, clock interrogation, and state detection, see Fig. 12.2. Driving the $S_{1/2} \rightarrow P_{1/2}$ and $D_{3/2} \rightarrow P_{1/2}$ transitions laser cools the ion. The population is then prepared to a $|S_{1/2}, F, m = 0\rangle$ sublevel in the $S_{1/2}$ ground state, where F denotes the hyperfine level and m denotes the magnetic sublevel. The $S_{1/2} \rightarrow D_{3/2}$ clock transition is then interrogated with either a Rabi or Ramsey measurement [177]. During state detection, scattered $S_{1/2} \rightarrow P_{1/2}$ photons are collected onto a detector. If the total

photon counts exceeds a predetermined detection threshold, the state detection event is characterized as "bright", otherwise the event is characterized as "dark". These bright and dark state detection events determine the probability that the clock transition was driven.

In the following subsections we consider a $^{225}Ra^{+}$ clock, nuclear spin $I = 1/2$, and describe operation for two different clock protocols: one requires a microwave source, and another requires Doppler cooling light polarized to drive π transitions. For nuclear spin $I > 1/2$, we consider a $^{137}Ba^{+}$, $I = 3/2$, and describe clock operation with Doppler cooling light polarized to drive π transitions.

12.1.3 $I = 1/2$ Microwave

In the first sequence described a microwave source and addressing three electronic transitions is required, see Fig. 12.2. Driving the $|S_{1/2}, F = 0\rangle \rightarrow |P_{1/2}, F = 1\rangle$ and $|S_{1/2}, F = 1\rangle \rightarrow |P_{1/2}, F = 1\rangle$ transitions Doppler cools the ion. Any decays to the $D_{3/2}$ state are repumped to the $P_{1/2}$ state by driving the $|D_{3/2}, F = 1\rangle \rightarrow |P_{1/2}, F = 1\rangle$ and $|D_{3/2}, F = 2\rangle \rightarrow |P_{1/2}, F = 1\rangle$ transitions. The population is then prepared in the $|S_{1/2}, F = 0, m = 0\rangle$ state by turning off the light driving the $|S_{1/2}, F = 0\rangle \rightarrow |P_{1/2}, F = 1\rangle$ transition [175]. The $|S_{1/2}, F = 0, m = 0\rangle \rightarrow |D_{3/2}, F = 2, m = 0\rangle$ electric quadrupole transition is driven followed by a $|D_{3/2}, F = 2, m = 0\rangle \rightarrow |D_{3/2}, F = 1, m = 0\rangle$ microwave π-pulse at 1.3 GHz. The $|S_{1/2}, F = 1\rangle \rightarrow |P_{1/2}, F = 0\rangle$ and $|D_{3/2}, F = 1\rangle \rightarrow |P_{1/2}, F = 0\rangle$ transitions are then used for state detection of the population. If the ion remains in the $|S_{1/2}, F = 0\rangle$ state, the resulting state detection event is dark. Otherwise, if the clock interrogation drives the ion to the $|D_{3/2}, F = 2\rangle$, it is subsequently shelved to the $|D_{3/2}, F = 1\rangle$ state with the microwave pulse and the state detection event is bright.

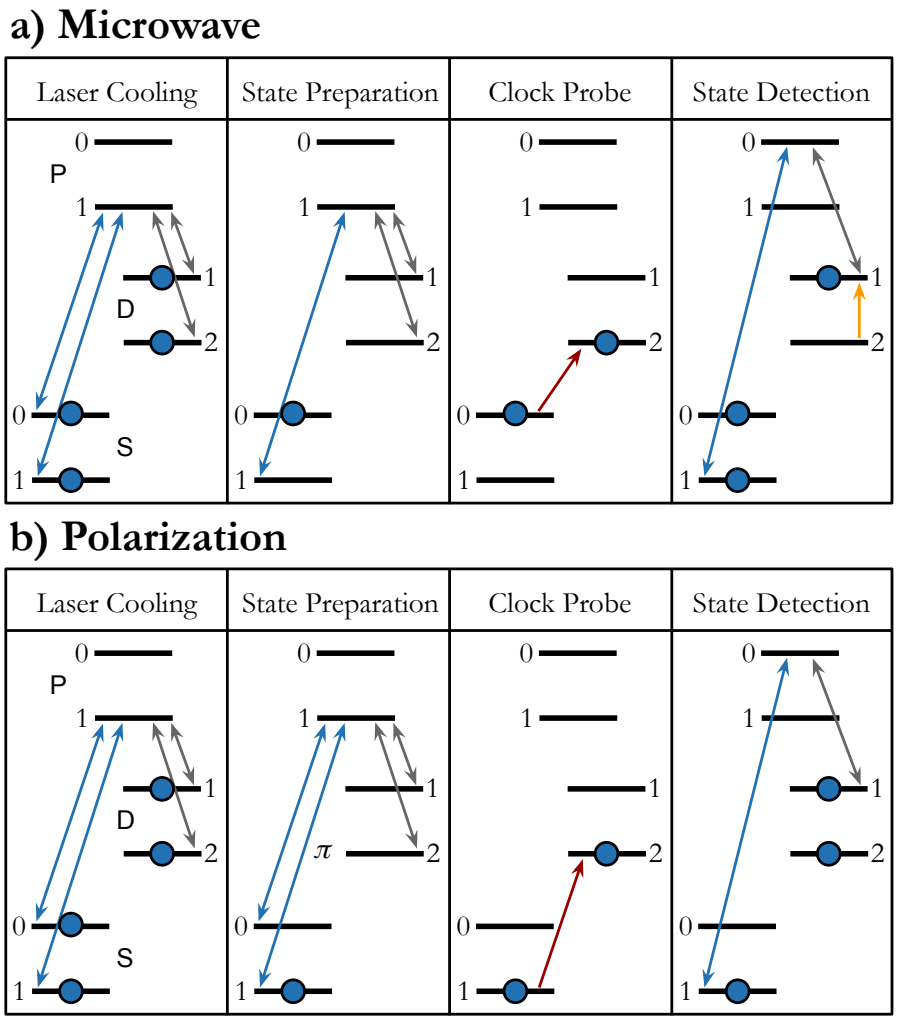

Figure 12.2: Clock measurement sequences for a $^{225}Ra^{+}$ ion optical clock based on the $S_{1/2} \rightarrow D_{3/2}$ transition (red). The total angular momentum quantum number F is shown next to each level. Arrows represent transitions between hyperfine levels, blue circles represent populated hyperfine levels, and gray circles represent the dark state during state detection. The $S_{1/2} \rightarrow P_{1/2}$ Doppler cooling transition (blue), $D_{3/2} \rightarrow P_{1/2}$ repump transition (gray), and $|D_{3/2}, F = 2, m = 0\rangle \rightarrow |D_{3/2}, F = 1, m = 0\rangle$ microwave transition (yellow) are shown. (a) Microwave clock sequence. (b) Polarization clock sequence.

12.1.4 $I = 1/2$ Polarization

The polarization clock sequence requires driving three electronic transitions and using Doppler cooling light polarized to drive π transitions, see Fig. 12.2 b). Laser cooling uses the same transitions as in the microwave sequence: the $|S_{1/2}, F = 0\rangle \rightarrow |P_{1/2}, F = 1\rangle$, $|S_{1/2}, F = 1\rangle \rightarrow |P_{1/2}, F = 1\rangle$, $|D_{3/2}, F = 1\rangle \rightarrow |P_{1/2}, F = 1\rangle$, and $|D_{3/2}, F = 2\rangle \rightarrow |P_{1/2}, F = 1\rangle$ transitions. But, state preparation requires laser polarization that drives π transitions within the $|S_{1/2}, F = 1\rangle \rightarrow |P_{1/2}, F = 1\rangle$ transition to prepare the population in the $|S_{1/2}, F = 1, m = 0\rangle$ sublevel [176, 3]. The $|S_{1/2}, F = 1, m = 0\rangle \rightarrow |D_{3/2}, F = 2, m = 0\rangle$ electric quadrupole transition is then driven. The $|S_{1/2}, F = 1\rangle \rightarrow |P_{1/2}, F = 0\rangle$ and $|D_{3/2}, F = 1\rangle \rightarrow |P_{1/2}, F = 0\rangle$ transitions are then used for state detection of the population. If the clock transition is driven the population will be in a dark state.

12.1.5 $I > 1/2$ Polarization

The polarization clock sequence for species with nuclear spin $I > 1/2$ requires driving three electronic transitions and using Doppler cooling light polarized to drive π transitions during state preparation. For $^{137}Ba^{+}$, driving the $|S_{1/2}, F = 2\rangle \rightarrow |P_{1/2}, F = 2\rangle$, $|S_{1/2}, F = 1\rangle \rightarrow |P_{1/2}, F = 2\rangle$, and $|S_{1/2}, F = 2\rangle \rightarrow |P_{1/2}, F = 1\rangle$ transitions Doppler cools the ion. Decays to the $D_{3/2}$ state are repumped to the $P_{1/2}$ state by driving the $|D_{3/2}, F = 0\rangle \rightarrow |P_{1/2}, F = 1\rangle$, $|D_{3/2}, F = 1\rangle \rightarrow |P_{1/2}, F = 1\rangle$, $|D_{3/2}, F = 2\rangle \rightarrow |P_{1/2}, F = 1\rangle$, and $|D_{3/2}, F = 3\rangle \rightarrow |P_{1/2}, F = 2\rangle$ transitions. The population is then prepared in the $|S_{1/2}, F = 1, m = 0\rangle$ state by stroboscopically driving the $|S_{1/2}, F = 1\rangle \rightarrow |P_{1/2}, F = 1\rangle$ and $|S_{1/2}, F = 2\rangle \rightarrow |P_{1/2}, F = 1\rangle$ transitions [3]. The $|S_{1/2}, F = 1, m = 0\rangle \rightarrow |D_{3/2}, F = 3, m = 0\rangle$ electric quadrupole transition is driven. The same transitions for laser cooling are then used for state detection of the population with the exception of the $|S_{1/2}, F = 1\rangle \rightarrow |P_{1/2}, F = 2\rangle$ and $|D_{3/2}, F = 3\rangle \rightarrow |P_{1/2}, F = 2\rangle$

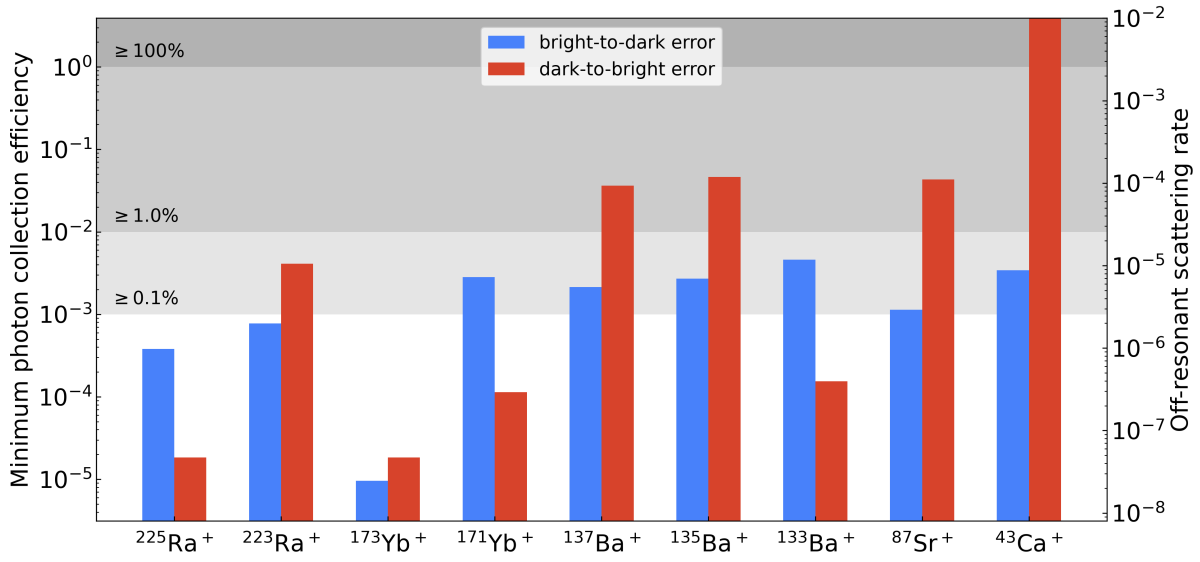

Figure 12.3: Histogram of bright-to-dark (blue) and dark-to-bright (red) errors. The left y-axis shows the off-resonant scattering rate for the errors, and the right y-axis shows the minimum photon collection efficiency needed for a 95% state detection fidelity with the requirement that 20 photons are collected. Gray shadings show the 100%, 1%, and 0.1% collection efficiency cutoffs. A collection efficiency above 100% is not possible as it would require counting more photons than actually exist.

transitions. If the clock transition is driven the population will be in a dark state.

12.1.6 State Detection Fidelity

Off-resonant scattering between hyperfine levels results in state detection infidelities for the clock [153]. "Bright-to-dark" errors occur when the population is off-resonantly driven from a bright hyperfine level to a dark one during the state detection. The probability of a bright-to-dark error per cooling transition photon scattered is

$$\epsilon_{\mathrm{bd}} = [\eta_{\mathrm{PS}} + (1-p) \times \eta_{\mathrm{PD}}/p] \times L(\delta, \Gamma) \tag{12.1}$$

where p is the $P_{1/2}$ state electronic branching fraction to the $S_{1/2}$ state, η_{PS} is the $|P_{1/2}, F\rangle \rightarrow |S_{1/2}, F'\rangle$ hyperfine branching fraction, η_{PD} is the $|P_{1/2}, F\rangle \rightarrow |D_{3/2}, F''\rangle$

hyperfine branching fraction, where F is the $P_{1/2}$ state hyperfine level that the population was off-resonantly driven to, and F' and F'' are the $S_{1/2}$ and $D_{3/2}$ state dark hyperfine levels. $L(\delta, \Gamma)$ is a Lorentzian where δ is the detuning from the transition resonance and Γ is the transition linewidth. "Dark-to-bright" errors ϵ_{db} occur when the population in the dark state is off-resonantly driven to a bright state, and are calculated in a similar way to ϵ_{bd} where F' and F'' are the $S_{1/2}$ and $D_{3/2}$ state bright hyperfine levels.

For the microwave sequence and the example case of $^{225}\mathrm{Ra}^{+}$, $\eta_{\mathrm{PS}} = 1/3$, $\eta_{\mathrm{PD}} = 5/6$, and $p = 0.9104(7)$ [5], we discuss the state detection infidelties, see Fig. 12.2. During state detection, the $|S_{1/2}, F = 1\rangle \rightarrow |P_{1/2}, F = 0\rangle$ is driven, but off-resonant scattering results in two sources of bright-to-dark error and one source of dark-to-bright error. A bright-to-dark error can occur when the state detection light addressing the $|S_{1/2}, F = 1\rangle \rightarrow |P_{1/2}, F = 0\rangle$ off-resonantly drives the $|S_{1/2}, F = 1\rangle \rightarrow |P_{1/2}, F = 1\rangle$ transition, which is detuned by the $P_{1/2}$ state hyperfine splitting (5.45 GHz). A bright-to-dark error can also occur when the state detection light addressing the $|D_{3/2}, F = 1\rangle \rightarrow |P_{1/2}, F = 0\rangle$ transition off-resonantly drives the $|D_{3/2}, F = 1\rangle \rightarrow |P_{1/2}, F = 1\rangle$ transition, which is also detuned by the HF_P splitting. The dark-to-bright error can occur when the $|S_{1/2}, F = 1\rangle \rightarrow |P_{1/2}, F = 0\rangle$ state detection light drives the $|S_{1/2}, F = 0\rangle \rightarrow |P_{1/2}, F = 1\rangle$ transition. But, this transition is detuned from the laser frequency by the sum of the $P_{1/2}$ and $S_{1/2}$ state hyperfine splittings (5.45 and 27.7 GHz, respectively [35]). This large detuning, 33.1 GHz, makes the microwave sequence, Sec. 12.1.3, more robust to dark-to-bright errors compared to the polarization sequence where the detuning is only the $D_{3/2}$ state hyperfine splitting (1.3 GHz [37]) Sec. 12.1.4. For the microwave sequence the probability of a bright-to-dark error is $\epsilon_{\mathrm{bd}} = 8.9 \times 10^{-7}$, and $\epsilon_{\mathrm{db}} = 4.3 \times 10^{-8}$ for a dark-to-bright error. Errors for other non-zero nuclear spin isotopes are shown in Table 12.2.

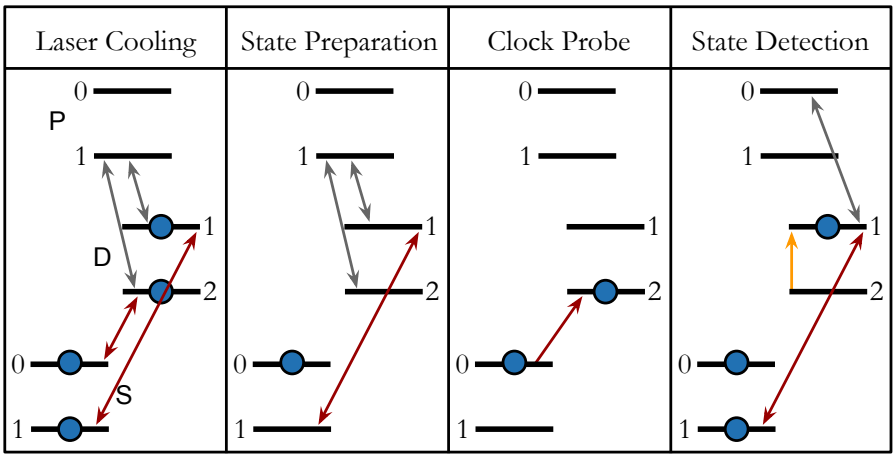

Figure 12.4: Clock measurement sequences for a two-laser $^{225}Ra^{+}$ ion optical clock based on the $S_{1/2} \rightarrow D_{3/2}$ transition (red), which is also used for Doppler cooling. Arrows represent transitions between hyperfine levels and blue circles represent populated hyperfine levels. The $D_{3/2} \rightarrow P_{1/2}$ repump transition (gray) and $|D_{3/2}, F = 2, m = 0\rangle \rightarrow |D_{3/2}, F = 1, m = 0\rangle$ microwave transition (yellow) are shown.

The off-resonant scattering rates for bright-to-dark and dark-to-bright errors, and the associated minimum photon collection efficiency needed to obtain a 95% state detection fidelity are shown in Fig. 12.3. The minimum photon collection efficiency is calculated with the requirement that on average 20 photons are collected during state detection. For $I = 1/2$ isotopes, the systems are robust against dark-to-bright errors, while for $I > 1/2$ isotopes, the four hyperfine levels in the $D_{3/2}$ state make the systems more susceptible to dark-to-bright errors during state detection. For a 95% state detection fidelity, the $^{225}Ra^{+}$ ion requires a 0.038% photon collection efficiency, considerably lower than the 0.28% photon collection efficiency demonstrated for the $^{226}Ra^{+}$ ion optical clock [7]. The $^{173}Yb^{+}$ ion has the lowest state detection error, 0.03%, among the ions considered. The low minimum photon collection efficiency state detection error is because of the high $P_{1/2}$ state to $S_{1/2}$ state branching fraction of 99.5% [153] and the nonsequential ordering of the four hyperfine levels in the $D_{3/2}$ state, which results in a larger detuning than sequential ordering.

12.1.7 Two Laser Clock Operation

A three-level clock may also enable clock operation with only two lasers addressing two electronic transitions. The ion could be laser cooled by strongly driving the $S_{1/2} \rightarrow D_{3/2}$ electric quadrupole transition and repumping with the $D_{3/2} \rightarrow P_{1/2}$ transition. Laser cooling has been achieved on the similar $S_{1/2} \rightarrow D_{5/2}$ electric quadrupole transition in $^{40}Ca^{+}$ [179]. For a three-level clock cooling on the $S_{1/2} \rightarrow D_{5/2}$ transition drops the requirement to drive the $S_{1/2} \rightarrow P_{1/2}$. For $^{225}Ra^{+}$ the clock would only need 828 nm and 1079 nm lasers, see Fig. 12.4. To perform Doppler cooling the $|S_{1/2}, F = 0\rangle \rightarrow |D_{3/2}, F = 2\rangle$ and $|S_{1/2}, F = 1\rangle \rightarrow |P_{1/2}, F = 1\rangle$ transitions are driven while driving the $|D_{3/2}, F = 2\rangle \rightarrow |P_{1/2}, F = 1\rangle$ and $|D_{3/2}, F = 1\rangle \rightarrow |P_{1/2}, F = 1\rangle$ transitions to repump population. The population is then prepared in the $|S_{1/2}, F = 0, m = 0\rangle$ state by turning off the light driving the $|S_{1/2}, F = 0\rangle \rightarrow |D_{3/2}, F = 2\rangle$ transition. For clock interrogation, the $|S_{1/2}, F = 0, m = 0\rangle \rightarrow |D_{3/2}, F = 2, m = 0\rangle$ transition is driven, followed by a $|D_{3/2}, F = 2, m = 0\rangle \rightarrow |D_{3/2}, F = 1, m = 0\rangle$ microwave π-pulse at 1.3 GHz which populates a bright state if the clock transition was driven. The $|S_{1/2}, F = 1\rangle \rightarrow |D_{3/2}, F = 1\rangle$ and $|D_{3/2}, F = 1\rangle \rightarrow |P_{1/2}, F = 0\rangle$ transitions are then driven for state detection. More power would be needed at 828 nm for laser cooling compared to the three laser schemes described in Sec. 12.1.2, but the trade-off in power could be enabling for integrated photonics as the only required wavelengths are now in the IR.

12.1.8 Conclusion

We have proposed three-level clocks with alkaline-earth-like ions with non-zero nuclear spin based on the $S_{1/2} \rightarrow D_{3/2}$ transition. We show that heavy species with large hyperfine splittings, including $^{133}Ba^{+}$, $^{171}Yb^{+}$, $^{173}Yb^{+}$, $^{223}Ra^{+}$, and $^{225}Ra^{+}$, are promis-

ing for realizing such clocks. We highlight $^{225}Ra^{+}$ as a candidate system for a three-level transportable clock due to its low state detection infidelity, ability to achieve low total systematic uncertainty, and suitability for integrated photonics [7]. Optical losses in integrated photonics generally decrease the farther the light is from the UV [116, 23], which makes clock species such as Ra^{+} [7], whose shortest wavelength is at 468 nm, see Fig. 12.1, promising for integrated photonics. The radium ion clock $\lambda = 828$ nm and repump $\lambda = 1079$ nm transitions could also be frequency summed to generate the $\lambda = 468$ nm Doppler cooling light, eliminating the need for a blue laser.

Among the alkaline-earth elements, the radium ion has the lowest sensitivity to blackbody radiation, and is promising for reaching total systematic uncertainty at the low 10^{-18} level [32, 7]. Similar to the other alkaline-earth-like ions, the radium ion's $S_{1/2} \rightarrow D_{3/2}$ clock transition has a negative differential scalar polarizability clock transition, see Table 12.1. This enables operation at a magic rf trap drive frequency, see Table 12.1.6, such that the micromotion induced-scalar Stark shift and the second-order Doppler shift cancel [132]. For $^{225}Ra^{+}$, the quadratic zeeman shift coefficient at zero field is smaller than that of the $^{171}Yb^{+}$ ion, see Table 12.2. In a clock frequency comparison with a protocol proposed here Ra^{+} could help improve the constraints on $\dot{\alpha}/\alpha$ [2]. For Ra^{+}, the sensitivity K to the time variation of the fine structure constant $\dot{\alpha}/\alpha$ of the $S_{1/2} \rightarrow D_{3/2}$ clock transition $K_{3/2} = 3.03$ is higher than the $S_{1/2} \rightarrow D_{5/2}$ transition $K_{5/2} = 2.78$, which is the largest positive K among demonstrated optical clocks [134]. This increase in sensitivity also comes with an improved stability because of the $D_{3/2}$ state lifetime 638(10) ms is more than a factor of two longer compared to the $D_{5/2}$ state lifetime 303(4) ms [79].

Table 12.1: Relevant atomic properties for alkaline-earth-like ions are given, including the $S_{1/2} \rightarrow P_{1/2}$ transition linewidth, $P_{1/2}$ state to $S_{1/2}$ state branching fraction p, transition wavelengths (nm), differential scalar polarizability α_0 (atomic units) of the $S_{1/2} \rightarrow D_{3/2}$ clock transition, and $D_{3/2}$ state lifetime.

Ion	$\Gamma/2\pi$ (MHz)	p	λ_{cool}	λ_{repump}	λ_{clock}	α_0	$\tau_{3/2}$ (s)
Ca^+	22.4 [166]	0.93565 [74]	397	866	732	-44.1(6) [139]	1.176(11) [167]
Sr^+	21.5 [168]	0.94498 [105]	422	1092	687	-26.9(1.1) [131]	0.435(4) [169]
Ba^+	20.3 [170]	0.73182 [170]	493	650	2052	-75.4(1.1) [131]	79.8(4.6) [171]
Yb^+	19.6 [172]	0.995 [153]	369.5	2438	435.5	-42(8) [46]	0.052(1) [173]
Ra^+	18.3 [79]	0.9104 [5]	468	1079	828	-20.8(1.7) [131]	0.638(10) [79]

Table 12.2: Candidate alkaline-earth-like isotopes and their relevant atomic properties are given, including the half-life, nuclear spin I, magic rf trap drive frequency Ω_{rf}, and hyperfine splittings, HF_n, of the $S_{1/2}$ and $P_{1/2}$ electronic states. Hyperfine splittings without a specified reference are from [3]. The evaluated $|S_{1/2}, F, m = 0\rangle \rightarrow |D_{3/2}, F', m = 0\rangle$ clock transition and quadratic Zeeman (QZ) shift at zero magnetic field are shown. ϵ_{bd} (ϵ_{db}) are probability for bright-to-dark (dark-to-bright) errors due to off-resonant scattering.

Species	Half-life	I	Ω_{rf}	HF_S (GHz)	HF_P (GHz)	Clock $F \rightarrow F'$	QZ (Hz/G^2)	ϵ_{bd}	ϵ_{db}
$^{43}\mathrm{Ca}^+$	stable	7/2	23.0	3.2	0.6	$3 \rightarrow 5$	-3732	8.2e-6	9.6e-3
$^{87}\mathrm{Sr}^+$	stable	9/2	15.0	5.0	0.9	$4 \rightarrow 6$	-3400	2.7e-6	1.0e-4
$^{133}\mathrm{Ba}^+$	10.5 y	1/2	3.4	9.9 [45]	1.8 [45]	$0 \rightarrow 2$	-532	8.6e-6	2.9e-7
$^{135}\mathrm{Ba}^+$	stable	3/2	3.3	7.2	1.3	$1 \rightarrow 3$	1321	5.1e-6	8.7e-5
$^{137}\mathrm{Ba}^+$	stable	3/2	3.3	8.0	1.5	$1 \rightarrow 3$	1162	4.0e-6	6.8e-5
$^{171}\mathrm{Yb}^+$	stable	1/2	7.7	12.6 [178]	2.1 [178]	$0 \rightarrow 2$	519	7.2e-6	2.9e-7
$^{173}\mathrm{Yb}^+$	stable	5/2	7.6	10.5 [178]	1.7 [178]	$2 \rightarrow 1$	1526	2.4e-8	4.7e-8
$^{223}\mathrm{Ra}^+$	11.4 d	3/2	6.1	6.8 [35]	1.3 [35]	$1 \rightarrow 3$	1205	1.8e-6	9.6e-6
$^{225}\mathrm{Ra}^+$	14.9 d	1/2	6.0	27.7 [35]	5.4 [35]	$0 \rightarrow 2$	-321	8.9e-7	4.3e-8

Chapter 13

Searches for New Physics with Atomic Clocks

Atomic clocks can constrain sources of new physics in tabletop or portable experiments operated by small teams [180, 181, 182, 2, 114]. Several options are present for improving the sensitivity and reach of these experiments, including ultra-high precision frequency comparisons [1], highly-charged ions [128], and a radioactive thorium nuclear clock [130]. In this chapter we describe these searches, and discuss the potential for radium ions to improve constraints.

13.1 Time Variation of Fundamental Constants

The idea that fundamental constants are space-time dependent is fundamentally unsettling. It defies the very meaning of the word constant. However, the idea is predicted by many theories beyond the standard model, and is directly related to one of largest mysteries in the known Universe, the nature of dark matter [183]. Atomic clocks are able to constrain potential time variation of fundamental constants through frequency

comparisons of sensitive optical or microwave transitions. To date, all of the tightest constraints on potential time variation of fundamental constants have been realized with atomic clocks [180, 2]. In the following subsections we describe the three fundamentals constants and ratios theorized to be space-time dependent.

13.1.1 Fine Structure Constant

A frequency comparison of two atomic clocks operating on different transitions can be used to constrain the potential time variation of the fine structure constant, α. An optical atomic clock based on a transition between electronic energy levels will have a frequency defined as

$$\nu \approx cR_\infty AF(\alpha) \tag{13.1a}$$

$$R_\infty = \frac{1}{hc}\frac{\alpha^2}{2}m_e c^2 \tag{13.1b}$$

where c is the speed of light, R_∞ is the Rydberg constant, A is an atom-dependent numerical factor, and $F(\alpha)$ is a transition-dependent factor [183]. The sensitivity of an optical clock transition to α can be estimated by calculating the shift in the energy given some finite deviation in α

$$\Delta E(\alpha) = \Delta E_0 + \Delta q\left[\left(\frac{\alpha}{\alpha_0}\right)^2 - 1\right] \tag{13.2a}$$

$$\Delta E = E_2 - E_1 \tag{13.2b}$$

$$\Delta q = q_2 - q_1 \tag{13.2c}$$

$$q = \frac{E(\delta) - E(-\delta)}{2\delta} \tag{13.2d}$$

where α_0 is the current value of α, E_0 is the corresponding clock transition energy, q is a coefficient that parameterizes the dependence of an electronic energy level on α, and δ is a deviation in α. A dimensionless enhancement factor

$$K_\alpha = \frac{2\Delta q}{\Delta E} \tag{13.3}$$

quantifies the sensitivity of a transition to α-variation. Table 13.1 shows the enhancement factor for demonstrated optical clocks.

Table 13.1: Sensitivity of the optical clock transition to potential time variation of the fine structure constant. Enhancement factors K are calculated from the values given in [134].

Species	Enhancement (K_α)
Ra^+	2.8
Yb^+ (E2)	1
Hg	0.8
Sr^+	0.4
Yb	0.3
Ca^+	0.1
Sr	0.06
Al^+	0.01
Hg^+	-2.9
Yb^+ (E3)	-6

A Ra^+ optical clock could be used to investigate potential time variation of the fine structure constant, $\dot{\alpha}/\alpha$. The current laboratory-based constraint on $\dot{\alpha}/\alpha$ is derived from a frequency comparison between an optical clock based on the Yb^+ (E3) transition and a second clock based on the Yb^+ (E2) transition [2]. The frequency ratio of the two clocks, $R = \nu_{E3}/\nu_{E2}$ is measured over time and then used to constrain the variation of α according to

$$\frac{\dot{R}}{R} = \Delta K_\alpha \frac{\dot{\alpha}}{\alpha} \tag{13.4}$$

where $\Delta K_\alpha = K_{\alpha E3} - K_{\alpha E2}$. The sensitivity of a frequency ratio measurement to $\dot{\alpha}/\alpha$ depends on both the difference in α-sensitivity factors ΔK_α of the clocks, as well as their overall performance. The Yb^+ (E3) clock's $K_{\alpha E3} \approx -6$ is the most negative of any demonstrated clock. It is desirable to compare this clock with a clock that has a large positive K_α (≈ 1 for the Yb^+ E2 transition) to enhance sensitivity to changes in α with a large ΔK_α factor. In a comparison with the Yb^+ (E3) clock, Ra^+ would have the advantage of the largest positive enhancement of any demonstrated clock, $K_\alpha = 2.8$ [134]. The single ion instability limit of Ra^+, 1.8×10^{-15}, is superior to Yb^+ E2, 2.6×10^{-15}, allowing the Ra^+ clock to achieve the same accuracy twice as fast. Further, of the key limiting systematics for the Yb^+ E2 clock Ra^+ has potential advantages of lower sensitivity to BBR as well as a higher mass which would likely lead to lower uncertainty in motional shifts. Given the potential to realize a high-performance Ra^+ clock, it would be appealing to compare a Ra^+ clock against a Yb^+ (E3) clock to further improve constraints on the time variation of the fine structure constant.

13.1.2 Ratio Between the Average Quark Mass and Quantum Chromodynamic Scale

An atom's hyperfine structure is also sensitive to the potential time variation of fundamental constants. The sensitivity of the hyperfine structure to variation in the

nuclear radius k_{hq} is

$$k_{hq} = 0.3k_{hr} \tag{13.5a}$$

$$k_{hr} = -\frac{(2\gamma - 1)\delta_h}{1 - \delta_h} \tag{13.5b}$$

$$\gamma = \sqrt{1 - Z^2\alpha^2} \tag{13.5c}$$

$$\delta_h = 1.995 \times (2.8 \times 10^{-5} Z^{4/3})^{2\gamma - 1}, \tag{13.5d}$$

where Z is the atom's atomic number and α is the fine structure constant [184]. For Ra^+, the calculated value is $k_{hq} = -0.039$, see Table 13.2. The sensitivity of the hyperfine structure to variation in the fine structure constant k_α is

$$k_\alpha \approx \frac{(Z\alpha)^2(12\gamma^2 - 1)}{\gamma^2(4\gamma^2 - 1)}. \tag{13.6}$$

The calculated value of k_α for Ra^+ is also shown in Table 13.2.

Table 13.2: The sensitivity of the hyperfine structure to variation in the nuclear radius k_{hq} and to variation of the fine structure constant k_α. With the exception of Ra^+, values are from [184].

Species	k_{hq}	k_α
Rb	-0.003	0.34
Cd^+	-0.005	0.6
Cs	-0.007	0.83
Yb^+	-0.014	1.5
Hg^+	-0.023	2.28
Ra^+	-0.039	3.2

The sensitivity of the nuclear magnetic moment to quark mass k_μ is

$$k_\mu = -0.117K_n - 0.100K_p - 0.11K_b, \tag{13.7}$$

where

$$K_p = \frac{g_p \langle s_p \rangle}{\mu} \tag{13.8a}$$

$$K_p = \frac{g_n \langle s_n \rangle}{\mu} \tag{13.8b}$$

$$K_{b_p} = \frac{(g_n - g_p + 1)\langle s_n \rangle}{\mu} \text{ (valence proton)} \tag{13.8c}$$

$$K_{b_n} = \frac{(g_p - g_n - 1)\langle s_p \rangle}{\mu} \text{ (valence neutron).} \tag{13.8d}$$

Here, $g_p = 5.586$ ($g_n = -3.826$) is the spin gyromagnetic factor for a proton (neutron) [129] and $\langle s_p \rangle$ ($\langle s_n \rangle$) is the expectation value for the total proton (neutron) spin, and μ is the nuclear magnetic moment [185]. The sensitivity of the hyperfine structure to variation in the quark mass to strong-interaction scale ratio m_q/Λ_{QCD} is $k_q = k_\mu + k_{hq}$. We present these values for radium isotopes with nuclear spin $I > 0$ that have suitably long lifetimes for measurements ($\tau > 1$ min) in Table 13.3.

Table 13.3: The $\langle s_n \rangle$ and $\langle s_p \rangle$ for radium isotopes are the recommended values from [185] Nuclear magnetic moments are in units of the nuclear magneton $\mu_N = e\hbar/2m_N$ from [186]. The sensitivity of the nuclear magnetic moment to quark mass k_μ and the sensitivity of the hyperfine structure to variation in the quark mass to strong-interaction scale ratio m_q/Λ_{QCD} (k_q) are shown.

Isotope	$\langle s_n \rangle$	$\langle s_p \rangle$	μ	k_μ	k_q
$^{223}Ra^+$	-0.196	-0.104	0.271	0.246	0.211
$^{225}Ra^+$	0.360	0.140	-0.7338	0.064	0.028
$^{227}Ra^+$	-0.116	-0.184	-0.404	-0.547	-0.582
$^{229}Ra^+$	0.213	0.287	0.503	-0.657	-0.692

Now that we have calculated values for k_α and k_μ we are ready to write an expression for the limit on the variation in the quark mass to strong-interaction scale ratio m_q/Λ_{QCD}. We consider the dependence of a hyperfine transition frequency V on the variation in the

fundamental constants:

$$V = \alpha^{2+k_\alpha} \left(\frac{m_q}{\Lambda_{QCD}} \right)^{k_q} \frac{m_e}{m_p} \tag{13.9}$$

where m_e is the mass of the electron and and m_p is the mass of the proton [184]. If we then compare the frequency of two hyperfine transitions V_a and V_b we find

$$\frac{V_a}{V_b} = \alpha^{k_{\alpha,a}-k_{\alpha,b}} \left(\frac{m_q}{\Lambda QCD} \right)^{k_{q,a}-k_{q,b}} \tag{13.10}$$

which, we can then express as a limit on the frequency ratio of V_a and V_b, that is

$$\frac{\delta}{\delta t}\ln\frac{V_a}{V_b} = (k_{\alpha,a} - k_{\alpha,b})\frac{\delta}{\delta t}\ln(\alpha) + (k_{q,a} - k_{q,b})\frac{\delta}{\delta t}\ln\left(\frac{m_q}{\Lambda_{QCD}}\right). \tag{13.11}$$

It becomes clear that to set stringent limits on the time variation of $X = m_q/\Lambda_{QCD}$ it is desirable to compare to hyperfine frequencies that not only can be measured to high precision, but also have a high sensitivity k_q. Because the limit on the time variation of the fine structure constant $\dot{\alpha}/\alpha$ is set with high-precision optical clocks, the uncertainty in that term does not contribute significantly to $\dot{X}/X$. Currently, the best limit on $\dot{X}/X = (-6.6 \pm 4.3) \times 10^{-15}\text{yr}^{-1}$ was made by comparing the microwave frequencies of a ^{87}Rb and ^{133}Cs fountain clock $\frac{\delta}{\delta t}\ln\frac{V_{\text{Rb}}}{V_{\text{Cs}}} = (-1.39 \pm 0.91) \times 10^{-16}\text{yr}^{-1}$ over a period of approximately 14 years [180]. The differential sensitivities for the Rb/Cs clock are $\Delta k_{\alpha,Rb/Cs} = -0.49$ and $\Delta k_{\text{q, Rb/Cs}} = -0.021$ [184].

A radium microwave clock could be used to improve these limits. The differential sensitivity between the two longer-lived isotopes, $^{223}\text{Ra}^+$ and $^{225}\text{Ra}^+$, is $\Delta k_{q,223/225} = 0.182 \approx 9\Delta k_{\text{Rb/Cs}}$, and the highest possible differential is $\Delta k_{q,223/229} = 0.903 \approx 43\Delta k_{\text{Rb/Cs}}$. To improve the current best constraint on $\dot{X}/X$ these systems would need to obtain a limit on their respective frequency ratios of $\frac{\delta}{\delta t}\ln\frac{V_{223}}{V_{225}} = (1.2 \pm 0.8) \times 10^{-15}\text{yr}^{-1}$ and $\frac{\delta}{\delta t}\ln\frac{V_{223}}{V_{229}} = (5.9 \pm 3.9) \times 10^{-15}\text{yr}^{-1}$. While these isotopes offer a substantial reduction in

the precision required for the frequency ratios, considerations would have to be made for working with the short-lived radioisotopes. One possible solution could be working with the isotopes in a neon gas environment, similar to the Hg^+ ion space clock [4], so that a large number of ions could be trapped with high efficiency. Alternatively, high performance could be realized by sympathetically cooling the radium ions [187].

13.1.3 Proton-to-Electron Mass Ratio

The limit on the time variation of the proton-to-electron mass ratio $\dot{\mu}/\mu$ can be calculated from the limits on $\dot{X}/X$ and $\dot{\alpha}/\alpha$. For any atomic transition frequency V, we know that any variation $\dot{V}$ can be expressed as

$$\dot{V}/V = \dot{\alpha}/\alpha + \dot{\mu}/\mu + \dot{X}/X \tag{13.12}$$

following equation 13.9 and [2]. Thus, any improvement in $\dot{\alpha}/\alpha$ or $\dot{X}/X$ will improve $\dot{\mu}/\mu$. Because all magnetic hyperfine splittings are equally sensitive to μ [2], it is not possible to improve $\dot{\mu}/\mu$ directly with a frequency comparison.

13.2 Transportable Clock Searches

13.2.1 Tests of the Gravitational Redshift

Transportable atomic clocks can test general relativity by measuring the gravitational redshift, the dilation of time in a deeper gravitational potential. If we consider two clocks, located at position 1 and 2, we can express the gravitation redshift between the

two positions $\Delta\nu = \nu_2 - \nu_1$ as

$$\frac{\Delta\nu}{\nu_1} = (1+\beta)\frac{\Delta U}{c^2} \tag{13.13}$$

where $\nu_{1(2)}$ is the clock frequency at location 1(2), $\Delta U = U_2 - U_1$ is the difference in gravitational potential, c is the speed of light, and β denotes any possible violation from general relativity [114]. Currently, the best constraint on β was made by two Galileo satellites that were mistakenly launched into elliptical orbits with $\Delta h = 8,500$ m [181, 182]. The best constraint of β on the ground was made by a pair of transportable optical lattice clocks at Tokyo Skytree [114].

The ideal way to improve constraints on β is to send high-precision optical clocks into space where Δh can be significantly larger than on the ground, and ΔU can be readily measured to high precision. A single satellite in earth-orbit equipped with an transportable optical clock could further constrain LPI through tests of the gravitational redshift to a part in 10^9 [188], three orders of magnitude more sensitive than current constraints [181, 182].

13.2.2 Gravitational Wave Detection

Gravitational waves, 'ripples' in space time caused by massive accelerating objects, were another phenomena predicted by Einstein's theory of general relativity over one century ago. However, it wasn't until 2016 at the Laser Interferometer Gravitational Wave Observatory that gravitational waves were directly detected [189, 190]. High-precision optical clocks onboard satellites could enable direct detection of that astrophysically interesting μHz-Hz band of gravitational waves [191, 192], bridging the gap between space-based and terrestrial gravitational wave detectors. With two synchronized optical clocks onboard spatially separated satellites that can share a beam of light over a single

baseline, the effective Doppler shifts induced by incident gravitational waves could be directly detected [192]. While optical lattice clocks would be ideal for this application because of their high SNRs and fast averaging time, their size and complexity may pose challenges for satellite deployment, making single ion clocks an appealing alternative [191].

Chapter 14

Trapped Ion Qubits

Trapped and laser cooled ions present a promising platform for realizing large-scale computing computing architectures. This chapter provides an overview of two different types of trapped ion qubits and their state preparation and measurement.

14.1 Optical Qubits

For optical qubits the ground $|0\rangle$ state is far removed from the excited $|1\rangle$ state. The separation between these states is in the optical frequency range, hence the name. In optical qubits, the excited state lifetime becomes the leading source of decoherence in the system. In alkaline-earth ions, the $S_{1/2}$ state is the $|0\rangle$ state and the $D_{5/2}$ state is the $|1\rangle$ state. As such, making optical qubits with strontium and radium ions, whose optical qubit $D_{5/2}$ state lifetime is < 1 s, challenging to realize. Another complication for optical qubits is the need for narrow-linewidth laser sources.

14.2 Hyperfine Qubits

For hyperfine qubits the ground $|0\rangle$ state is close to the excited $|1\rangle$ state. The separation between these states is in the microwave frequency range and sources that can access the GHz transitions are readily available. In alkaline-earth ions the two $m_F = 0$ magnetic sublevel in the $S_{1/2}$ state hyperfine levels serve as the $|0\rangle$ and $|1\rangle$ states. Off-resonant scattering during state detection could lead to error in the system.

14.3 State Preparation and Measurement

For quantum computation to be realized there must be robust state initialization and detection [193]. In the quantum information world, preparing to the $|0\rangle$ and $|1\rangle$ state, see Fig. 14.1, and the following readout of the state is typically referred to as state preparation and measurement (SPAM). SPAM errors are the first source of errors that will originate in a system before gate operations even begin.

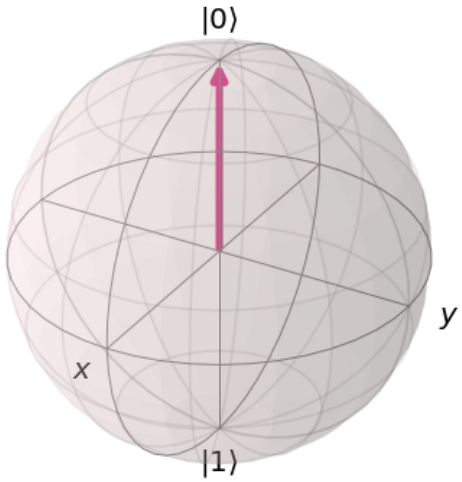

Figure 14.1: Bloch sphere visualization that is often used to help map out qubit gate operations. Figure made with Qiskit.

14.3.1 SPAM Fidelity

State preparation errors can be generalized for alkaline earth ion hyperfine qubits with nuclear spins $I \geq 1/2$. If we consider dipole cooling transitions from $S(F, F+1) \rightarrow P(F' + F' + 1)$, the state preparation infidelity is

$$\epsilon_{\text{prep}} = \frac{\Gamma^2}{2}\left[\frac{1}{\delta^2_{\text{HF, S}}} + \frac{\eta_{F',F+1}}{\eta_{F'+1,F+1}}\frac{1}{\delta^2_-}\right] \tag{14.1}$$

where Γ is the Doppler cooling transition linewidth, $\delta^2_{\text{HF, S}}$ is the ground state hyperfine splitting, $\eta_{i,j}$ denotes the branching from the excited hyperfine state to the ground hyperfine state, and δ_- is the hyperfine splitting difference between the ground and excited states [3].

Table 14.1: Predicted state preparation infidelities.

Species	I	$\eta_{F'+1,F+1}$	$\eta_{F',F+1}$	$\Gamma/2\pi$	HF_S (GHz)	HF_P (GHz)	ϵ_{prep}
$^{87}\text{Sr}^+$	9/2	2/5	11/15	21.5	5.0	0.89	3.4e-5
$^{171}\text{Yb}^+$	1/2	2/3	1	19.7	12.6	2.1	3.9e-6
$^{223}\text{Ra}^+$	3/2	1/2	5/6	18.3	6.8	1.3	1.3e-5
$^{225}\text{Ra}^+$	1/2	2/3	1	18.3	27.7	5.4	7.2e-7

We calculate the predicted state preparation infidelities for species discussed in this thesis in Table 14.1. Notably, $^{225}\text{Ra}^+$ has the lowest predicted state preparation infidelity. It is a factor of ≈ 5.4 lower than the predicted state preparation infidelity of $^{171}\text{Yb}^+$, and lower than all species with nuclear spin $I > 1/2$ predicted values in [3]. Currently, the $^{137}\text{Ba}^+$ qubit (ϵ_{prep}=1.1e-5) that has nuclear spin $I = 3/2$ has the highest demonstrated fidelity SPAM of $(9.0 \pm 1.3) \times 10^{-5}(-40.5 \pm 0.6\text{dB})$, due to the large $P_{1/2}$ state hyperfine splitting [3].

14.3.2 $^{87}Sr^{+}$

SPAM for $^{87}Sr^{+}$ will be similar to the polarization state preparation scheme presented in [3], and has been explained in depth in Chapter 11. The high nuclear spin of $^{87}Sr^{+}$ means that only a microwave assisted optical preparation (MAOP) scheme can be realized to further reduce errors beyond what is possible with the polarization state preparation alone [3]. In the MAOP scheme, see Fig. 14.2, errors in the $F = 4$ hyperfine level are cleaned out to the $F = 5$ state with microwaves that drive π transitions. Once the errors are driven to the $F = 5$ hyperfine level they can be driven to the $F = 4$ hyperfine level with light driving the $|S_{1/2}, F = 5\rangle \rightarrow |P_{1/2}, F = 5\rangle$ transition. Though this process is a factor of four slower than MAOP for a nuclear spin $I = 3/2$ qubit such as $^{137}Ba^{+}$, a strontium qubit has very nice wavelengths for integrated photonics [22] as well as a nice mass for dual-qubit, multi-species gates [194].

14.3.3 $^{225}Ra^{+}$

SPAM for $^{225}Ra^{+}$ will be identical to that of a typical nuclear spin $I = 1/2$ system such as $^{133}Ba^{+}$ [195] or $^{171}Yb^{+}$ [153]. The state preparation has been explained in Chapter 10. The large hyperfine splitting of the ground state of $^{225}Ra^{+}$ is promising for achieving high fidelity SPAM, see Table 14.1. While the high-fidelity and nice wavelengths are suitable for large-scale quantum information architecture, the radioactivity of radium may pose problems for scalability.

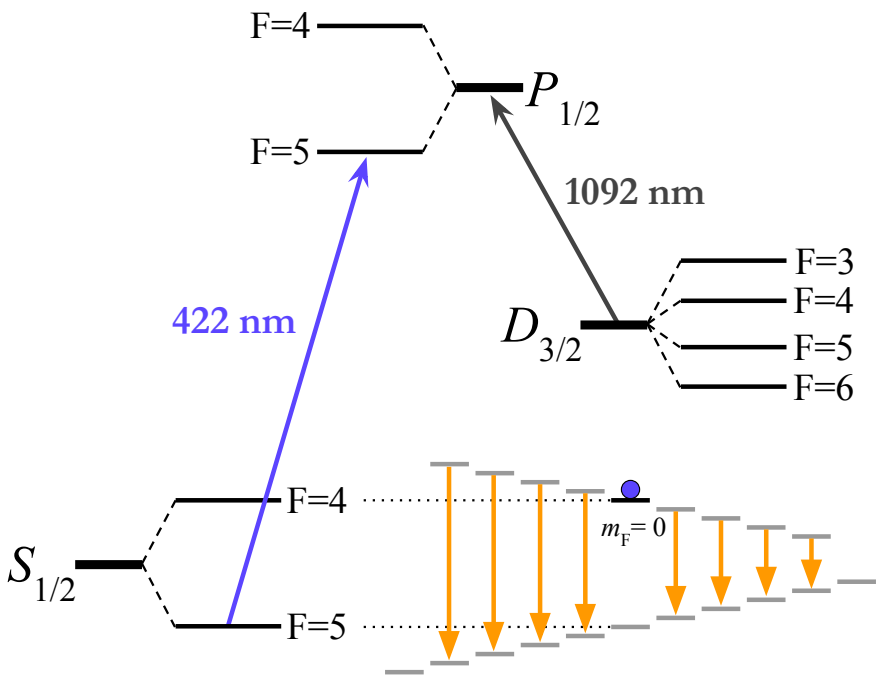

Figure 14.2: Microwave assisted optical preparation to improve the state preparation fidelity of $^{87}Sr^{+}$. Microwave π-pulses (orange) clear errors out of the $|S_{1/2}, F = 4\rangle$ hyperfine level. Then a flushing beam (blue) driving the $|S_{1/2}, F = 5\rangle \rightarrow |P_{1/2}, F = 5\rangle$ transition sends the population back to the $|S_{1/2}, F = 4\rangle$ hyperfine level where it has a probability of decaying to the $|S_{1/2}, F = 4, m = 0\rangle$ magnetic sublevel.

Appendix A

Appendix

A.1 Ablation Target and Mounting

This appendix contains the part files used to assemble the ablation target that contains the dried radium chloride sample. More information on the ablation target and mounting can be found in Chapter 4 and Chapter 7.

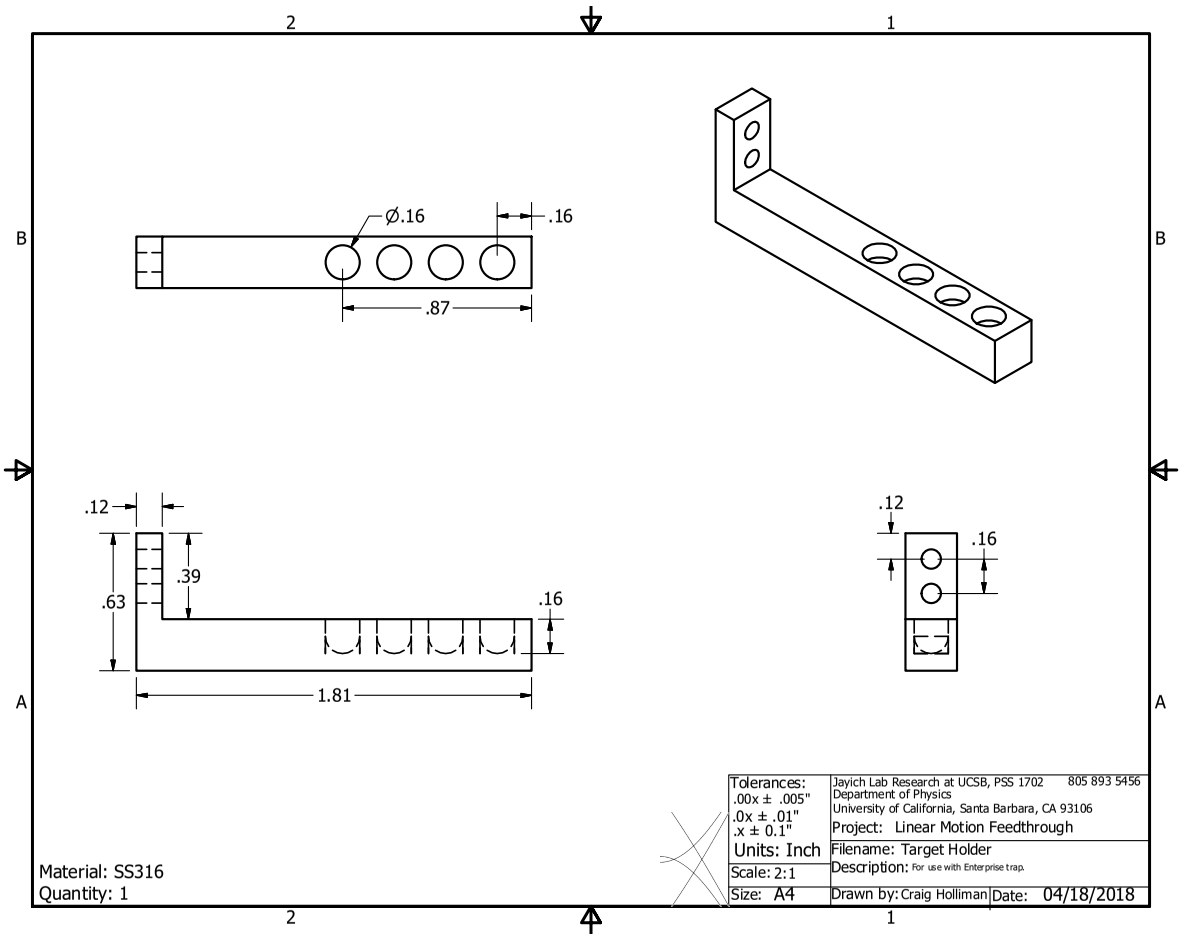
2
1
B
A
Ø.16
.16
.87
.12
.39
.63
.16
1.81
.12
.16
Material: SS316
Quantity: 1
Tolerances:
.00x ± .005"
.0x ± .01"
.x ± 0.1"
Units: Inch
Scale: 2:1
Size: A4
Jayich Lab Research at UCSB, PSS 1702 805 893 5456
Department of Physics
University of California, Santa Barbara, CA 93106
Project: Linear Motion Feedthrough
Filename: Target Holder
Description: For use with Enterprise trap.
Drawn by: Craig Holliman
Date: 04/18/2018

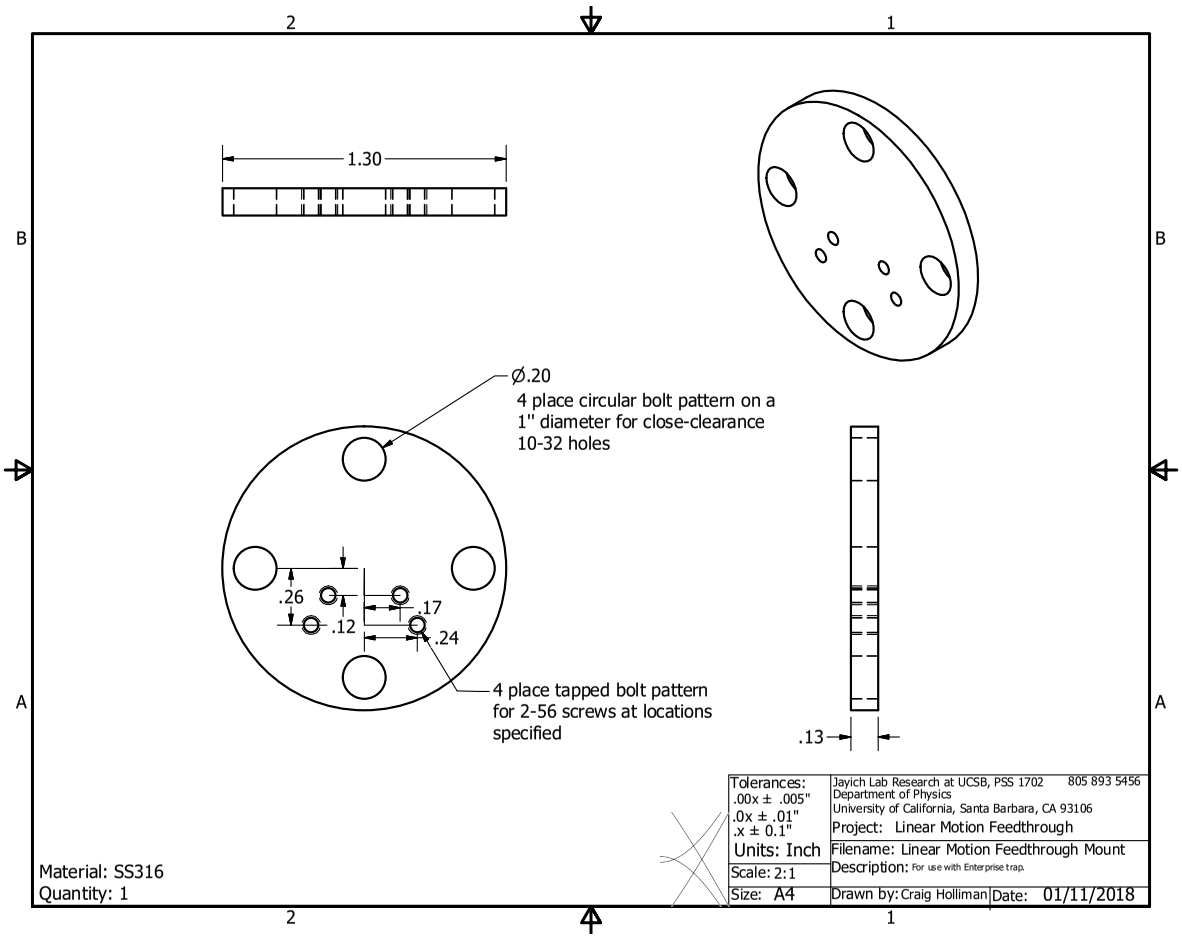
2
1
B
A
1.30
Ø.20
4 place circular bolt pattern on a
1" diameter for close-clearance
10-32 holes
.26
.12
.17
.24
4 place tapped bolt pattern
for 2-56 screws at locations
specified
.13
Material: SS316
Quantity: 1
Tolerances:
.00x ± .005"
.0x ± .01"
.x ± 0.1"
Units: Inch
Scale: 2:1
Size: A4
Jayich Lab Research at UCSB, PSS 1702 805 893 5456
Department of Physics
University of California, Santa Barbara, CA 93106
Project: Linear Motion Feedthrough
Filename: Linear Motion Feedthrough Mount
Description: For use with Enterprise trap.
Drawn by: Craig Holliman
Date: 01/11/2018

Bibliography

[1] **Boulder Atomic Clock Optical Network (BACON) Collaboration** Collaboration, K. Beloy *et. al.*, *Frequency ratio measurements at 18-digit accuracy using an optical clock network*, *Nature (London)* **591** (2021) 564.

[2] R. Lange, N. Huntemann, J. M. Rahm, C. Sanner, H. Shao, B. Lipphardt, C. Tamm, S. Weyers, and E. Peik, *Improved limits for violations of local position invariance from atomic clock comparisons*, *Phys. Rev. Lett.* **126** (Jan., 2021) 011102.

[3] F. A. An, A. Ransford, A. Schaffer, L. R. Sletten, J. Gaebler, J. Hostetter, and G. Vittorini, *High fidelity state preparation and measurement of ion hyperfine qubits with $I > 1/2$*, 2022.

[4] E. A. Burt, J. D. Prestage, R. L. Tjoelker, D. G. Enzer, D. Kuang, D. W. Murphy, D. E. Robison, J. M. Seubert, R. T. Wang, and T. A. Ely, *Demonstration of a trapped-ion atomic clock in space*, *Nature* **595** (June, 2021) 43–47.

[5] M. Fan, C. A. Holliman, A. L. Wang, and A. M. Jayich, *Laser cooling of radium ions*, *PRL* **122** (June, 2019) 223001.

[6] C. A. Holliman, M. Fan, and A. M. Jayich, *Measurements of electric quadrupole transition frequencies in* $^{226}Ra^{+}$, *PRA* **100** (Dec., 2019) 062512.

[7] C. A. Holliman, M. Fan, A. Contractor, S. M. Brewer, and A. M. Jayich, *Radium ion optical clock*, *PRL* **128** (Jan., 2022) 033202.

[8] D. J. Berkeland, J. D. Miller, J. C. Bergquist, W. M. Itano, and D. J. Wineland, *Minimization of ion micromotion in a paul trap*, *J. Appl. Phys.* **83** (1998), no. 10 5025–5033.

[9] A. Drakoudis, M. Söllner, and G. Werth, *Instabilities of ion motion in a linear paul trap*, *International Journal of Mass Spectrometry* **252** (2006), no. 1 61 – 68.

[10] W. Paul, *Electromagnetic traps for charged and neutral particles*, *RMP* **62** (July, 1990) 531–540.

[11] D. J. Berkeland and M. G. Boshier, *Destabilization of dark states and optical spectroscopy in zeeman-degenerate atomic systems*, *Phys. Rev. A* **65** (Feb., 2002) 033413.

[12] D. J. Wineland and W. M. Itano, *Laser cooling of atoms*, *Phys. Rev. A* **20** (Oct, 1979) 1521–1540.

[13] C. Foot, *Atomic Physics*. Oxford University Press, 2005.

[14] W. Neuhauser, M. Hohenstatt, P. Toschek, and H. Dehmelt, *Optical-sideband cooling of visible atom cloud confined in parabolic well*, *PRL* **41** (July, 1978) 233–236.

[15] D. J. Wineland, R. E. Drullinger, and F. L. Walls, *Radiation-pressure cooling of bound resonant absorbers*, *PRL* **40** (June, 1978) 1639–1642.

[16] Y. Huang, H. Zhang, B. Zhang, Y. Hao, H. Guan, M. Zeng, Q. Chen, Y. Lin, Y. Wang, S. Cao, K. Liang, F. Fang, Z. Fang, T. Li, and K. Gao, *Geopotential measurement with a robust, transportable* Ca^+ *optical clock*, *PRA* **102** (Nov., 2020) 050802.

[17] W. Loh, J. Stuart, D. Reens, C. D. Bruzewicz, D. Braje, J. Chiaverini, P. W. Juodawlkis, J. M. Sage, and R. McConnell, *Operation of an optical atomic clock with a brillouin laser subsystem*, *Nature* **588** (2020), no. 7837 244–249.

[18] T. Manovitz, R. Shaniv, Y. Shapira, R. Ozeri, and N. Akerman, *Precision measurement of atomic isotope shifts using a two-isotope entangled state*, *Phys. Rev. Lett.* **123** (Nov, 2019) 203001.

[19] C. Solaro, S. Meyer, K. Fisher, J. C. Berengut, E. Fuchs, and M. Drewsen, *Improved isotope-shift-based bounds on bosons beyond the standard model through measurements of the* $^2D_{3/2} \rightarrow {}^2D_{5/2}$ *interval in* Ca^+, *PRL* **125** (Sept., 2020) 123003.

[20] P. Dubé, A. A. Madej, and B. Jian, *Sr^+ single-ion clock*, *Journal of Physics: Conference Series* **723** (June, 2016) 012018.

[21] C. D. Bruzewicz, J. Chiaverini, R. McConnell, and J. M. Sage, *Trapped-ion quantum computing: Progress and challenges*, *Applied Physics Reviews* **6** (June, 2019) 021314.

[22] R. J. Niffenegger, J. Stuart, C. Sorace-Agaskar, D. Kharas, S. Bramhavar, C. D. Bruzewicz, W. Loh, R. T. Maxson, R. McConnell, D. Reens, G. N. West, J. M. Sage, and J. Chiaverini, *Integrated multi-wavelength control of an ion qubit*, *Nature* **586** (2020), no. 7830 538–542.

[23] G. N. West, W. Loh, D. Kharas, C. Sorace-Agaskar, K. K. Mehta, J. Sage, J. Chiaverini, and R. J. Ram, *Low-loss integrated photonics for the blue and ultraviolet regime*, *APL Photonics* **4** (Feb., 2019) 026101.

[24] H. Sunaoshi, Y. Fukashiro, M. Furukawa, M. Yamauchi, S. Hayashibe, T. Shinozuka, M. Fujioka, I. Satoh, M. Wada, and S. Matsuki, *A precision measurement of the hyperfine structure of* $^{87}Sr^{+}$, *Hyperfine Interactions* **78** (Mar., 1993) 241–245.

[25] M. K. Nayak and R. K. Chaudhuri, *Relativistic coupled cluster method*, *The European Physical Journal D - Atomic, Molecular, Optical and Plasma Physics* **37** (2006), no. 2 171–176.

[26] F. Buchinger, E. B. Ramsay, E. Arnold, W. Neu, R. Neugart, K. Wendt, R. E. Silverans, P. Lievens, L. Vermeeren, D. Berdichevsky, R. Fleming, D. W. Sprung, and G. Ulm, *Systematics of nuclear ground state properties in* $^{78-100}Sr$ *by laser spectroscopy.*, *Physical review. C, Nuclear physics* **41** (Jun, 1990) 2883–2897.

[27] W. Itano, *Quadrupole moments and hyperfine constants of metastable states of* Ca^{+}, Sr^{+}, Ba^{+}, Yb^{+}, Hg^{+}, *and* Au, *Physical Review A (Atomic, Molecular and Optical Physics)* (2006-02-01, 2006).

[28] G. P. Barwood, K. Gao, P. Gill, G. Huang, and H. A. Klein, *Observation of the hyperfine structure of the* $^2S_{1/2} \rightarrow ^2 D_{5/2}$ *transition in* $^{87}Sr^{+}$, *PRA* **67** (Jan., 2003) 013402.

[29] B. Graner, Y. Chen, E. G. Lindahl, and B. R. Heckel, *Reduced limit on the permanent electric dipole moment of* ^{199}Hg, *Phys. Rev. Lett.* **116** (Apr., 2016) 161601.

[30] I. Kozyryev and N. R. Hutzler, *Precision measurement of time-reversal symmetry violation with laser-cooled polyatomic molecules*, *Phys. Rev. Lett.* **119** (Sept., 2017) 133002.

[31] M. Fan, C. A. Holliman, X. Shi, H. Zhang, M. W. Straus, X. Li, S. W. Buechele, and A. M. Jayich, *Optical mass spectrometry of cold* $RaOH^{+}$ *and* $RaOCH_3{}^{+}$, *Phys. Rev. Lett.* **126** (Jan, 2021) 023002.

[32] O. O. Versolato, L. W. Wansbeek, K. Jungmann, R. G. E. Timmermans, L. Willmann, and H. W. Wilschut, *Potential of electric quadrupole transitions in radium isotopes for single-ion optical frequency standards*, *PRA* **83** (Apr., 2011) 043829.

[33] B. Santra, U. Dammalapati, A. Groot, K. Jungmann, and L. Willmann, *Absolute frequency measurement of the* $7s^2\ ^1S_0 \rightarrow 7s7p\ ^1P_1$ *transition in* ^{225}Ra, *Phys. Rev. A* **90** (Oct., 2014) 040501.

[34] O. O. Versolato, G. S. Giri, L. W. Wansbeek, J. E. van den Berg, D. J. van der Hoek, K. Jungmann, W. L. Kruithof, C. J. G. Onderwater, B. K. Sahoo, B. Santra, P. D. Shidling, R. G. E. Timmermans, L. Willmann, and H. W. Wilschut, *Laser spectroscopy of trapped short-lived* Ra^+ *ions*, *Phys. Rev. A* **82** (July, 2010) 010501.

[35] W. Neu, R. Neugart, E. W. Otten, G. Passler, K. Wendt, B. Fricke, E. Arnold, H. J. Kluge, and G. Ulm, *Quadrupole moments of radium isotopes from the* $7p^2P_{3/2}$ *hyperfine structure in ra ii*, *Zeitschrift für Physik D Atoms, Molecules and Clusters* **11** (June, 1989) 105–111.

[36] K. Wendt, S. A. Ahmad, W. Klempt, R. Neugart, E. W. Otten, and H. H. Stroke, *On the hyperfine structure and isotope shift of radium*, *Zeitschrift für Physik D Atoms, Molecules and Clusters* **4** (Sept., 1987) 227–241.

[37] B. K. Sahoo, B. P. Das, R. K. Chaudhuri, D. Mukherjee, R. G. E. Timmermans, and K. Jungmann, *Investigations of* Ra^+ *properties to test possibilities for new optical-frequency standards*, *Phys. Rev. A* **76** (Oct., 2007) 040504.

[38] M. Drewsen and A. Brøner, *Harmonic linear paul trap: Stability diagram and effective potentials*, *PRA* **62** (Sept., 2000) 045401.

[39] T. Dinneen, A. Ghiorso, and H. Gould, *An orthotropic source of thermal atoms*, *Review of Scientific Instruments* **67** (Mar., 1996) 752–755.

[40] M. J. Copley and T. E. Phipps, *The surface ionization of potassium on tungsten*, *PR* **48** (Dec., 1935) 960–968.

[41] J. R. Griswold, C. U. Jost, D. W. Stracener, S. H. Bruffey, D. Denton, M. Garland, L. Heilbronn, and S. Mirzadeh, *Production of* ^{229}Th *for medical applications: Excitation functions of low-energy protons on* ^{232}Th *targets*, *PRC* **98** (Oct., 2018) 044607.

[42] J. Cariou and P. Luc, *Atlas du spectre d'absorption de la molecule de tellure: 21100-23800 cm to the minus 1, temperature: 510 degrees C.* No. pt. 5. Laboratoire Aime-Cotton CNRS II, 1980.

[43] K. Zimmermann, M. V. Okhapkin, O. A. Herrera-Sancho, and E. Peik, *Laser ablation loading of a radiofrequency ion trap*, *Applied Physics B* **107** (June, 2012) 883–889.

[44] S. Olmschenk and P. Becker, *Laser ablation production of* Ba*,* Ca*,* Dy*,* Er*,* La*,* Lu*, and* Yb *ions*, *Applied Physics B* **123** (Mar., 2017) 99.

[45] D. Hucul, J. E. Christensen, E. R. Hudson, and W. C. Campbell, *Spectroscopy of a synthetic trapped ion qubit*, *Phys. Rev. Lett.* **119** (Sep, 2017) 100501.

[46] T. Schneider, E. Peik, and C. Tamm, *Sub-hertz optical frequency comparisons between two trapped $^{171}Yb^{+}$ ions*, *PRL* **94** (June, 2005) 230801.

[47] E. A. Donley, T. P. Heavner, F. Levi, M. O. Tataw, and S. R. Jefferts, *Double-pass acousto-optic modulator system*, *Review of Scientific Instruments* **76** (2005), no. 6 063112, [https://doi.org/10.1063/1.1930095].

[48] E. D. Black, *An introduction to pound-drever-hall laser frequency stabilization*, *American Journal of Physics* **69** (Jan., 2001) 79–87.

[49] M. Kumph, *2D arrays of ion traps for large scale integration of quantum information processors*. PhD thesis, University of Innsbruck, 2015.

[50] A. A. Madej, L. Marmet, and J. E. Bernard, *Rb atomic absorption line reference for single Sr^{+} laser cooling systems*, *Applied Physics B* **67** (1998), no. 2 229–234.

[51] C. Schneider, S. J. Schowalter, P. Yu, and E. R. Hudson, *Electronics of an ion trap with integrated time-of-flight mass spectrometer*, *Int. J. of Mass Spectrom.* **394** (Jan., 2016) 1–8.

[52] W. Alt, *An objective lens for efficient fluorescence detection of single atoms*, *Optik* **113** (2002), no. 3 142 – 144.

[53] G. Shu, M. R. Dietrich, N. Kurz, and B. B. Blinov, *Trapped ion imaging with a high numerical aperture spherical mirror*, *Journal of Physics B: Atomic, Molecular and Optical Physics* **42** (jul, 2009) 154005.

[54] Y. Glickman, *Ion-Ion and Ion-Photon Entanglement in Trapped Ions System*. PhD thesis, Weizmann Institute of Science, 2012.

[55] L. M. Bennie, P. T. Starkey, M. Jasperse, C. J. Billington, R. P. Anderson, and L. D. Turner, *A versatile high resolution objective for imaging quantum gases*, *Opt. Express* **21** (Apr, 2013) 9011–9016.

[56] J. D. Pritchard, J. A. Isaacs, and M. Saffman, *Long working distance objective lenses for single atom trapping and imaging*, *Review of Scientific Instruments* **87** (2016), no. 7 073107, [https://aip.scitation.org/doi/pdf/10.1063/1.4959775].

[57] T. Pruttivarasin and H. Katori, *Compact field programmable gate array-based pulse-sequencer and radio-frequency generator for experiments with trapped atoms*, *Rev. Sci. Instrum.* **86** (Nov., 2015) 115106.

[58] M.-A. Bouchiat and C. Bouchiat, *Parity violation in atoms*, *Rep. Prog. Phys.* **60** (1997), no. 11 1351.

[59] E. D. Commins, J. D. Jackson, and D. P. DeMille, *The electric dipole moment of the electron: An intuitive explanation for the evasion of schiff's theorem*, *Am. J. Phys.* **75** (June, 2007) 532–536.

[60] N. Auerbach, V. V. Flambaum, and V. Spevak, *Collective t- and p-odd electromagnetic moments in nuclei with octupole deformations*, *PRL* **76** (June, 1996) 4316–4319.

[61] M. S. Safronova, D. Budker, D. DeMille, D. F. J. Kimball, A. Derevianko, and C. W. Clark, *Search for new physics with atoms and molecules*, *Rev. Mod. Phys.* **90** (June, 2018) 025008.

[62] M. Dine and A. Kusenko, *Origin of the matter-antimatter asymmetry*, *Rev. Mod. Phys.* **76** (Dec., 2003) 1–30.

[63] W. B. Cairncross, D. N. Gresh, M. Grau, K. C. Cossel, T. S. Roussy, Y. Ni, Y. Zhou, J. Ye, and E. A. Cornell, *Precision measurement of the electron's electric dipole moment using trapped molecular ions*, *Phys. Rev. Lett.* **119** (Oct., 2017) 153001.

[64] J. Dobaczewski and J. Engel, *Nuclear time-reversal violation and the schiff moment of* ^{225}Ra, *Phys. Rev. Lett.* **94** (June, 2005) 232502.

[65] R. H. Parker, M. R. Dietrich, M. R. Kalita, N. D. Lemke, K. G. Bailey, M. Bishof, J. P. Greene, R. J. Holt, W. Korsch, Z.-T. Lu, P. Mueller, T. P. O'Connor, and J. T. Singh, *First measurement of the atomic electric dipole moment of* ^{225}Ra, *Phys. Rev. Lett.* **114** (June, 2015) 233002.

[66] K. Okada, M. Wada, L. Boesten, T. Nakamura, I. Katayama, and S. Ohtani, *Acceleration of the chemical reaction of trapped* Ca^+ *ions with* H_2O *molecules by laser excitation*, *J. Phys. B* **36** (2003), no. 1 33.

[67] T. Yang, A. Li, G. K. Chen, C. Xie, A. G. Suits, W. C. Campbell, H. Guo, and E. R. Hudson, *Optical control of reactions between water and laser-cooled* Be^+ *ions*, *J. Phys. Chem. Lett.* **9** (July, 2018) 3555–3560.

[68] R. Noek, G. Vrijsen, D. Gaultney, E. Mount, T. Kim, P. Maunz, and J. Kim, *High speed, high fidelity detection of an atomic hyperfine qubit*, *Opt. Lett.* **38** (Nov., 2013) 4735–4738.

[69] C. Senko, P. Richerme, J. Smith, A. Lee, I. Cohen, A. Retzker, and C. Monroe, *Realization of a quantum integer-spin chain with controllable interactions*, *Phys. Rev. X* **5** (June, 2015) 021026.

[70] N. Fortson, *Possibility of measuring parity nonconservation with a single trapped atomic ion*, *Phys. Rev. Lett.* **70** (Apr., 1993) 2383–2386.

[71] C. Wieman and A. Derevianko, "Atomic parity violation and the standard model."

[72] E. Traykov, U. Dammalapati, S. De, O. C. Dermois, L. Huisman, K. Jungmann, W. Kruithof, A. J. Mol, C. J. G. Onderwater, A. Rogachevskiy, M. da Silva e Silva, M. Sohani, O. Versolato, L. Willmann, and H. W. Wilschut, *Production and trapping of radioactive atoms at the triup facility*, *Nucl. Instrum. Methods Phys. Res., Sec. B* **266** (Oct., 2008) 4532–4536.

[73] M. Nuñez Portela, E. A. Dijck, A. Mohanty, H. Bekker, J. E. van den Berg, G. S. Giri, S. Hoekstra, C. J. G. Onderwater, S. Schlesser, R. G. E. Timmermans, O. O. Versolato, L. Willmann, H. W. Wilschut, and K. Jungmann, Ra^+ *ion trapping: toward an atomic parity violation measurement and an optical clock*, *Applied Physics B* **114** (Jan., 2014) 173–182.

[74] M. Ramm, T. Pruttivarasin, M. Kokish, I. Talukdar, and H. Häffner, *Precision measurement method for branching fractions of excited $P_{1/2}$ states applied to $^{40}Ca^+$*, *Phys. Rev. Lett.* **111** (July, 2013) 023004.

[75] T. Pruttivarasin, M. Ramm, and H. Häffner, *Direct spectroscopy of the $^2S_{1/2} \rightarrow {}^2P_{1/2}$ and $^2D_{3/2} \rightarrow {}^2P_{1/2}$ transitions and observation of micromotion modulated spectra in trapped $^{40}Ca^+$*, *J. Phys. B* **47** (2014), no. 13 135002.

[76] A. Gallagher and A. Lurio, *Optical detection of level crossing in a $j = \frac{1}{2}$ state*, *Phys. Rev. Lett.* **10** (Jan, 1963) 25–26.

[77] D. Zimmermann, *Determination of the lifetime of the $4P_{1/2}$ state of potassium by hanle-effect*, *Z. Phys. A* **275** (Mar, 1975) 5–10.

[78] See Supplemental Material for further discussion of branching fraction systematic effects and micromotion broadening of the $S_{1/2} \rightarrow P_{1/2}$ linescan.

[79] R. Pal, D. Jiang, M. S. Safronova, and U. I. Safronova, *Calculation of parity-nonconserving amplitude and other properties of* Ra^+, *Phys. Rev. A* **79** (June, 2009) 062505.

[80] B. K. Sahoo, L. W. Wansbeek, K. Jungmann, and R. G. E. Timmermans, *Light shifts and electric dipole matrix elements in* Ba^+ *and* Ra^+, *Phys. Rev. A* **79** (May, 2009) 052512.

[81] V. A. Dzuba and V. V. Flambaum, *Calculation of nuclear-spin-dependent parity nonconservation in $S \rightarrow D$ transitions of* Ba^+, Yb^+, *and* Ra^+ *ions*, *Phys. Rev. A* **83** (May, 2011) 052513.

[82] L. W. Wansbeek, B. K. Sahoo, R. G. E. Timmermans, K. Jungmann, B. P. Das, and D. Mukherjee, *Atomic parity nonconservation in* Ra^+, *Phys. Rev. A* **78** (Nov., 2008) 050501.

[83] C.-w. Chou, C. Kurz, D. B. Hume, P. N. Plessow, D. R. Leibrandt, and D. Leibfried, *Preparation and coherent manipulation of pure quantum states of a single molecular ion*, *Nature (London)* **545** (May, 2017) 203–207.

[84] E. Rasmussen, *Serien im funkenspektrum des radiums. ra ii*, *Zeitschrift für Physik* **86** (Jan, 1933) 24–32.

[85] K. Heilig and A. Steudel, *Changes in mean-square nuclear charge radii from optical isotope shifts*, *Atomic Data and Nuclear Data Tables* **14** (Nov., 1974) 613–638.

[86] P. G. Reinhard, W. Nazarewicz, and R. F. G. Ruiz, 2019.

[87] J. C. Berengut, D. Budker, C. Delaunay, V. V. Flambaum, C. Frugiuele, E. Fuchs, C. Grojean, R. Harnik, R. Ozeri, G. Perez, and Y. Soreq, *Probing new long-range interactions by isotope shift spectroscopy*, *Phys. Rev. Lett.* **120** (Feb., 2018) 091801.

[88] J. Bieroń, P. Indelicato, and P. Jönsson, *Multiconfiguration dirac-hartree-fock calculations oftransition rates and lifetimes of the eight lowest excited levels of radium*, *The European Physical Journal Special Topics* **144** (May, 2007) 75–84.

[89] D. F. V. James, *Quantum dynamics of cold trapped ions with application to quantum computation*, *Applied Physics B* **66** (Feb., 1998) 181–190.

[90] C. Roos, *Controlling the quantum state of trapped ions*. PhD thesis, University of Innsbruck, 2000.

[91] S. Gerstenkorn, J. Verges, and J. Chevillard, *Atlas du spectre d'absorption de la molecule d'iode: 11000-14000 cm to the minus 1*. Laboratoire Aime-Cotton CNRS II, Paris, 1982.

[92] S. Gerstenkorn and P. Luc, *Atlas du spectre d'absorption de la molecule d'iode: 14000-15600 cm to the minus 1*. Laboratoire Aime-Cotton CNRS II, Paris, 1982.

[93] M. Fan, C. A. Holliman, A. Contractor, C. Zhang, S. F. Gebretsadken, and A. M. Jayich, *Measurement of the* Ra^+ $7p\,^2P_{3/2}$ *state lifetime*, *PRA* **105** (Apr., 2022) 042801.

[94] H. Knöckel and E. Tiemann, IodineSpec5 (2011) (Universität Hannover, Hannover, 2011).

[95] H. Knöckel, B. Bodermann, and E. Tiemann, *High precision description of the rovibronic structure of the i2 b-x spectrum**, *Eur. Phys. J. D* **28** (Feb., 2004) 199–209.

[96] G. S. Giri, O. O. Versolato, J. E. van den Berg, O. Böll, U. Dammalapati, D. J. van der Hoek, K. Jungmann, W. L. Kruithof, S. Müller, M. Nuñez Portela, C. J. G. Onderwater, B. Santra, R. G. E. Timmermans, L. W. Wansbeek, L. Willmann, and H. W. Wilschut, *Isotope shifts of the* $6d^2D_{3/2} \to 7p^2P_{1/2}$ *transition in trapped short-lived* $^{209-214}$Ra$^+$, *PRA* **84** (Aug., 2011) 020503(R).

[97] W. H. King, *Comments on the article "peculiarities of the isotope shift in the samarium spectrum"*, *J. Opt. Soc. Am.* **53** (May, 1963) 638–639.

[98] L. W. Wansbeek, S. Schlesser, B. K. Sahoo, A. E. L. Dieperink, C. J. G. Onderwater, and R. G. E. Timmermans, *Charge radii of radium isotopes*, *Phys. Rev. C* **86** (July, 2012) 015503.

[99] K. M. Lynch, S. G. Wilkins, J. Billowes, C. L. Binnersley, M. L. Bissell, K. Chrysalidis, T. E. Cocolios, T. D. Goodacre, R. P. de Groote, G. J. Farooq-Smith, D. V. Fedorov, V. N. Fedosseev, K. T. Flanagan, S. Franchoo, R. F. Garcia Ruiz, W. Gins, B. A. Marsh, P. L. Molkanov, P. Naubereit, G. Neyens, C. M. Ricketts, S. Rothe, C. Seiffert, M. D. Seliverstov, H. H. Stroke, D. Studer, A. R. Vernon, K. D. A. Wendt, and X. F. Yang, *Laser-spectroscopy studies of the nuclear structure of neutron-rich radium*, *Phys. Rev. C* **97** (Feb., 2018) 024309.

[100] V. V. Flambaum, A. J. Geddes, and A. V. Viatkina, *Isotope shift, nonlinearity of king plots, and the search for new particles*, *PRA* **97** (Mar., 2018) 032510.

[101] C. A. Holliman, M. Fan, A. Contractor, M. W. Straus, and A. M. Jayich, *Direct measurement of the* $7s\,^2S_{1/2} \to 7p\,^2P_{3/2}$ *transition frequency in* ^{226}Ra$^+$, *PRA* **102** (Oct., 2020) 042822.

[102] P. Dubé, A. A. Madej, Z. Zhou, and J. E. Bernard, *Evaluation of systematic shifts of the* ^{88}Sr$^+$ *single-ion optical frequency standard at the* 10^{-17} *level*, *Phys. Rev. A* **87** (Feb., 2013) 023806.

[103] M. Fan, C. A. Holliman, S. G. Porsev, M. S. Safronova, and A. M. Jayich, *Measurement of the* $7p\,^2P_{3/2}$ *state branching fractions in* Ra$^+$, *PRA* **100** (Dec., 2019) 062504.

[104] R. Gerritsma, G. Kirchmair, F. Zähringer, J. Benhelm, R. Blatt, and C. F. Roos, *Precision measurement of the branching fractions of the* $4p^2P_{3/2}$ *decay of* Ca$^+$, *The European Physical Journal D* **50** (Nov, 2008) 13–19.

[105] H. Zhang, M. Gutierrez, G. H. Low, R. Rines, J. Stuart, T. Wu, and I. Chuang, *Iterative precision measurement of branching ratios applied to* $5P$ *states in* ^{88}Sr$^+$, *New Journal of Physics* **18** (2016), no. 12 123021.

[106] T. Dutta, D. De Munshi, D. Yum, R. Rebhi, and M. Mukherjee, *An exacting transition probability measurement - a direct test of atomic many-body theories*, *Scientific Reports* **6** (July, 2016) 29772.

[107] M. Hettrich, T. Ruster, H. Kaufmann, C. F. Roos, C. T. Schmiegelow, F. Schmidt-Kaler, and U. G. Poschinger, *Measurement of dipole matrix elements with a single trapped ion*, *PRL* **115** (Oct., 2015) 143003.

[108] Z. Meir, M. Sinhal, M. S. Safronova, and S. Willitsch, *Combining experiments and relativistic theory for establishing accurate radiative quantities in atoms: The lifetime of the* $^2P_{3/2}$ *state in* $^{40}Ca^+$, *PRA* **101** (Jan., 2020) 012509.

[109] K. J. Arnold, R. Kaewuam, T. R. Tan, S. G. Porsev, M. S. Safronova, and M. D. Barrett, *Dynamic polarizability measurements with* $^{176}Lu^+$, *Phys. Rev. A* **99** (Jan, 2019) 012510.

[110] P.-L. Liu, Y. Huang, W. Bian, H. Shao, H. Guan, Y.-B. Tang, C.-B. Li, J. Mitroy, and K.-L. Gao, *Measurement of magic wavelengths for the* $^{40}Ca^+$ *clock transition*, *Phys. Rev. Lett.* **114** (Jun, 2015) 223001.

[111] S. R. Chanu, V. P. W. Koh, K. J. Arnold, R. Kaewuam, T. R. Tan, Z. Zhang, M. S. Safronova, and M. D. Barrett, *Magic wavelength of the* $^{138}Ba^+$ $6s$ $^2S_{1/2} \rightarrow 5d\ ^2D_{5/2}$ *clock transition*, *PRA* **101** (Apr., 2020) 042507.

[112] X.-M. Wu, C.-B. Li, Y.-B. Tang, and T.-Y. Shi, *Magic wavelengths for the* $7S_{1/2} \rightarrow 6D_{3/2,5/2}$ *transitions in* Ra^+, *Chinese Physics B* **25** (aug, 2016) 093101.

[113] A. D. Ludlow, M. M. Boyd, J. Ye, E. Peik, and P. O. Schmidt, *Optical atomic clocks*, *Rev. Mod. Phys.* **87** (June, 2015) 637–701.

[114] M. Takamoto, I. Ushijima, N. Ohmae, T. Yahagi, K. Kokado, H. Shinkai, and H. Katori, *Test of general relativity by a pair of transportable optical lattice clocks*, *Nature Photonics* **14** (2020), no. 7 411–415.

[115] J. Grotti, S. Koller, S. Vogt, S. Häfner, U. Sterr, C. Lisdat, H. Denker, C. Voigt, L. Timmen, A. Rolland, F. N. Baynes, H. S. Margolis, M. Zampaolo, P. Thoumany, M. Pizzocaro, B. Rauf, F. Bregolin, A. Tampellini, P. Barbieri, M. Zucco, G. A. Costanzo, C. Clivati, F. Levi, and D. Calonico, *Geodesy and metrology with a transportable optical clock*, *Nature Physics* (Feb., 2018).

[116] X. Liu, A. W. Bruch, Z. Gong, J. Lu, J. B. Surya, L. Zhang, J. Wang, J. Yan, and H. X. Tang, *Ultra-high-q uv microring resonators based on a single-crystalline aln platform*, *Optica* **5** (Oct., 2018) 1279–1282.

[117] S. M. Brewer, J.-S. Chen, A. M. Hankin, E. R. Clements, C. W. Chou, D. J. Wineland, D. B. Hume, and D. R. Leibrandt, $^{27}Al^+$ *quantum-logic clock with a systematic uncertainty below* 10^{-18}, *Phys. Rev. Lett.* **123** (July, 2019) 033201.

[118] N. Huntemann, C. Sanner, B. Lipphardt, C. Tamm, and E. Peik, *Single-ion atomic clock with* 3×10^{-18} *systematic uncertainty*, *Phys. Rev. Lett.* **116** (Feb., 2016) 063001.

[119] T. L. Nicholson, S. L. Campbell, R. B. Hutson, G. E. Marti, B. J. Bloom, R. L. McNally, W. Zhang, M. D. Barrett, M. S. Safronova, G. F. Strouse, W. L. Tew, and J. Ye, *Systematic evaluation of an atomic clock at* 2×10^{18} *total uncertainty*, *Nat. Communications* **6** (Apr., 2015) 6896.

[120] W. F. McGrew, X. Zhang, R. J. Fasano, S. A. Schäffer, K. Beloy, D. Nicolodi, R. C. Brown, N. Hinkley, G. Milani, M. Schioppo, T. H. Yoon, and A. D. Ludlow, *Atomic clock performance enabling geodesy below the centimetre level*, *Nature (London)* **564** (Dec., 2018) 87–90.

[121] F. Riehle, *Towards a redefinition of the second based on optical atomic clocks*, *C. R. Phys.* **16** (2015), no. 5 506–515.

[122] M. Long-Sheng, B. Zhiyi, B. Albrecht, R. Lennart, Z. Massimo, S. Windeler Robert, W. Guido, O. Chris, H. Leo, and A. Diddams Scott, *Optical frequency synthesis and comparison with uncertainty at the* 10^{-19} *level*, *Science* **303** (Mar., 2004) 1843–1845.

[123] P. Gill, *Is the time right for a redefinition of the second by optical atomic clocks?*, *Journal of Physics: Conference Series* **723** (2016) 012053.

[124] A. Derevianko and M. Pospelov, *Hunting for topological dark matter with atomic clocks*, *Nat. Phys.* **10** (2014), no. 12 933–936.

[125] M. S. Safronova, D. Budker, D. DeMille, D. F. J. Kimball, A. Derevianko, and C. W. Clark, *Search for new physics with atoms and molecules*, *Rev. Mod. Phys.* **90** (Jun, 2018) 025008.

[126] K. J. Arnold, R. Kaewuam, A. Roy, T. R. Tan, and M. D. Barrett, *Blackbody radiation shift assessment for a lutetium ion clock*, *Nat. Commun.* **9** (2018), no. 1 1650.

[127] K. Beloy, V. A. Dzuba, and S. M. Brewer, *Quadruply ionized barium as a candidate for a high-accuracy optical clock*, *Phys. Rev. Lett.* **125** (Oct., 2020) 173002.

[128] M. G. Kozlov, M. S. Safronova, J. R. Crespo López-Urrutia, and P. O. Schmidt, *Highly charged ions: Optical clocks and applications in fundamental physics*, *RMP* **90** (Dec., 2018) 045005.

[129] V. V. Flambaum and A. F. Tedesco, *Dependence of nuclear magnetic moments on quark masses and limits on temporal variation of fundamental constants from atomic clock experiments*, *PRC* **73** (May, 2006) 055501.

[130] B. Seiferle, L. von der Wense, P. V. Bilous, I. Amersdorffer, C. Lemell, F. Libisch, S. Stellmer, T. Schumm, C. E. Düllmann, A. Pálffy, and P. G. Thirolf, *Energy of the 229th nuclear clock transition*, *Nature (London)* **573** (2019), no. 7773 243–246.

[131] B. K. Sahoo, R. G. E. Timmermans, B. P. Das, and D. Mukherjee, *Comparative studies of dipole polarizabilities in* Sr^+*,* Ba^+*, and* Ra^+ *and their applications to optical clocks*, *Phys. Rev. A* **80** (Dec., 2009) 062506.

[132] P. Dubé, A. A. Madej, M. Tibbo, and J. E. Bernard, *High-accuracy measurement of the differential scalar polarizability of a* $^{88}Sr^+$ *clock using the time-dilation effect*, *Phys. Rev. Lett.* **112** (Apr., 2014) 173002.

[133] Y. Huang, H. Guan, M. Zeng, L. Tang, and K. Gao, $^{40}Ca^+$ *ion optical clock with micromotion-induced shifts below* 1×10^{-18}, *Phys. Rev. A* **99** (Jan, 2019) 011401(R).

[134] V. V. Flambaum and V. A. Dzuba, *Search for variation of the fundamental constants in atomic, molecular, and nuclear spectra*, *Can. J. Phys.* **87** (Jan., 2009) 25–33.

[135] P. Dubé, A. A. Madej, A. Shiner, and B. Jian, $^{88}Sr^+$ *single-ion optical clock with a stability approaching the quantum projection noise limit*, *PRA* **92** (Oct., 2015) 042119.

[136] See Supplemental Material for further discussion of systematic shifts and uncertainties, which includes Refs. [102, 6, 131, 144, 152, 145].

[137] V. I. Yudin, A. V. Taichenachev, C. W. Oates, Z. W. Barber, N. D. Lemke, A. D. Ludlow, U. Sterr, C. Lisdat, and F. Riehle, *Hyper-ramsey spectroscopy of optical clock transitions*, *Phys. Rev. A* **82** (July, 2010) 011804(R).

[138] A. V. Taichenachev, V. I. Yudin, C. W. Oates, Z. W. Barber, N. D. Lemke, A. D. Ludlow, U. Sterr, C. Lisdat, and F. Riehle, *Compensation of field-induced frequency shifts in ramsey spectroscopy of optical clock transitions*, *JETP Lett.* **90** (2010), no. 11 713–717.

[139] M. S. Safronova and U. I. Safronova, *Blackbody radiation shift, multipole polarizabilities, oscillator strengths, lifetimes, hyperfine constants, and excitation energies in* Ca^+, *Phys. Rev. A* **83** (Jan., 2011) 012503.

[140] M. S. Safronova, M. G. Kozlov, and C. W. Clark, *Blackbody radiation shifts in optical atomic clocks*, *Trans. Ultrason. Ferroelectr. Freq. Control* **59** (2012), no. 3 439–447.

[141] M. Chwalla, J. Benhelm, K. Kim, G. Kirchmair, T. Monz, M. Riebe, P. Schindler, A. S. Villar, W. Hänsel, C. F. Roos, R. Blatt, M. Abgrall, G. Santarelli, G. D. Rovera, and P. Laurent, *Absolute frequency measurement of the* $^{40}Ca^{+}$ $4s\ ^2S_{1/2} \rightarrow 3d\ ^2D_{5/2}$ *clock transition*, *Phys. Rev. Lett.* **102** (Jan., 2009) 023002.

[142] Y. Huang, J. Cao, P. Liu, K. Liang, B. Ou, H. Guan, X. Huang, T. Li, and K. Gao, *Hertz-level measurement of the* $^{40}Ca^{+}$ $4s\ ^2S_{1/2}$–$3d\ ^2D_{5/2}$ *clock transition frequency with respect to the si second through the global positioning system*, *Phys. Rev. A* **85** (Mar., 2012) 030503(R).

[143] T. Rosenband, D. B. Hume, P. O. Schmidt, C. W. Chou, A. Brusch, L. Lorini, W. H. Oskay, R. E. Drullinger, T. M. Fortier, J. E. Stalnaker, S. A. Diddams, W. C. Swann, N. R. Newbury, W. M. Itano, D. J. Wineland, and J. C. Bergquist, *Frequency ratio of* Al^{+} *and* Hg+ *single-ion optical clocks; metrology at the 17th decimal place*, *Science* **319** (Mar., 2008) 1808.

[144] D. J. Berkeland, J. D. Miller, J. C. Bergquist, W. M. Itano, and D. J. Wineland, *Minimization of ion micromotion in a paul trap*, *J. Appl. Phys.* **83** (1998), no. 10 5025–5033.

[145] K. J. Arnold, R. Kaewuam, S. R. Chanu, T. R. Tan, Z. Zhang, and M. D. Barrett, *Precision measurements of the* $^{138}Ba^{+}$ $6s^2S_{1/2} - 5d^2D_{5/2}$ *clock transition*, *Phys. Rev. Lett.* **124** (May, 2020) 193001.

[146] H. C. J. Gan, G. Maslennikov, K.-W. Tseng, T. R. Tan, R. Kaewuam, K. J. Arnold, D. Matsukevich, and M. D. Barrett, *Oscillating-magnetic-field effects in high-precision metrology*, *Phys. Rev. A* **98** (Sept., 2018) 032514.

[147] G. Marx, G. Tommaseo, and G. Werth, *Precise and factor measurements of* Ba^{+} *isotopes*, *Eur. Phys. J. D* **4** (Dec., 1998) 279–284.

[148] T. Rosenband, P. O. Schmidt, D. B. Hume, W. M. Itano, T. M. Fortier, J. E. Stalnaker, K. Kim, S. A. Diddams, J. C. J. Koelemeij, J. C. Bergquist, and D. J. Wineland, *Observation of the* $^1S_0 \rightarrow^3 P_0$ *clock transition in* $^{27}Al^{+}$, *Phys. Rev. Lett.* **98** (May, 2007) 220801.

[149] E. R. Clements, M. E. Kim, K. Cui, A. M. Hankin, S. M. Brewer, J. Valencia, J.-S. Chen, C.-W. Chou, D. R. Leibrandt, and D. B. Hume, *Lifetime-limited interrogation of two independent* $^{27}Al^{+}$ *clocks using correlation spectroscopy*, *Phys. Rev. Lett.* **125** (Dec, 2020) 243602.

[150] W. M. Haynes, *Crc handbook of chemistry and physics 96th edition*, *CRC Press, Boca Raton, FL,* (2015).

[151] B. Santra, *Precision spectroscopy of neutral radium: towards searches for permanent electric dipole Electric.* PhD thesis, University of Groningen,, 2013.

[152] J. Keller, H. L. Partner, T. Burgermeister, and T. E. Mehlstäubler, *Precise determination of micromotion for trapped-ion optical clocks*, *J. Appl. Phys.* **118** (Aug., 2015) 104501.

[153] S. Olmschenk, K. C. Younge, D. L. Moehring, D. N. Matsukevich, P. Maunz, and C. Monroe, *Manipulation and detection of a trapped* Yb^+ *hyperfine qubit*, *PRA* **76** (Nov., 2007) 052314.

[154] W. M. Itano, *External-field shifts of the* $^{199}Hg^+$ *optical frequency standard*, *Journal of research of the National Institute of Standards and Technology* **105** (Dec., 2000) 829–837.

[155] W. H. Oskay, W. M. Itano, and J. C. Bergquist, *Measurement of the* $^{199}Hg^+$ *electric quadrupole moment and a constraint on the quadrupole shift*, *PRL* **94** (Apr., 2005) 163001.

[156] J. Leute, N. Huntemann, B. Lipphardt, C. Tamm, P. B. R. Nisbet-Jones, S. A. King, R. M. Godun, J. M. Jones, H. S. Margolis, P. B. Whibberley, A. Wallin, M. Merimaa, P. Gill, and E. Peik, *Frequency comparison of* $^{171}Yb^+$ *ion optical clocks at ptb and npl via gps ppp*, *IEEE Transactions on Ultrasonics, Ferroelectrics, and Frequency Control* **63** (2016), no. 7 981–985.

[157] K. Beloy, D. R. Leibrandt, and W. M. Itano, *Hyperfine-mediated electric quadrupole shifts in* Al^+ *and* In^+ *ion clocks*, *PRA* **95** (Apr., 2017) 043405.

[158] R. Lange, N. Huntemann, C. Sanner, H. Shao, B. Lipphardt, C. Tamm, and E. Peik, *Coherent suppression of tensor frequency shifts through magnetic field rotation*, *PRL* **125** (Sept., 2020) 143201.

[159] M. G. Boshier, G. P. Barwood, G. Huang, and H. A. Klein, *Polarisation-dependent optical pumping for interrogation of a magnetic-field-independent "clock" transition in laser-cooled trapped* $^{87}Sr^+$, *Applied Physics B* **71** (July, 2000) 51–56.

[160] C. Champenois, M. Houssin, C. Lisowski, M. Knoop, G. Hagel, M. Vedel, and F. Vedel, *Evaluation of the ultimate performances of a* Ca^+ *single-ion frequency standard*, *Physics Letters A* **331** (Oct., 2004) 298–311.

[161] J. Benhelm, G. Kirchmair, U. Rapol, T. Körber, C. F. Roos, and R. Blatt, *Measurement of the hyperfine structure of the* $S_{1/2} \rightarrow D_{5/2}$ *transition in* $^{43}Ca^+$, *PRA* **75** (Mar., 2007) 032506.

[162] J. Benhelm, *Precision spectroscopy and quantum information processing with trapped calcium Fractions*. PhD thesis, University of Innsbruck, 2008.

[163] R. M. Godun, P. B. R. Nisbet-Jones, J. M. Jones, S. A. King, L. A. M. Johnson, H. S. Margolis, K. Szymaniec, S. N. Lea, K. Bongs, and P. Gill, *Frequency ratio of two optical clock transitions in* $^{171}Yb^{+}$ *and constraints on the time variation of fundamental constants*, *PRL* **113** (Nov., 2014) 210801.

[164] C. Tamm, N. Huntemann, B. Lipphardt, V. Gerginov, N. Nemitz, M. Kazda, S. Weyers, and E. Peik, *Cs-based optical frequency measurement using cross-linked optical and microwave oscillators*, *PRA* **89** (Feb., 2014) 023820.

[165] A. A. Madej, J. E. Bernard, P. Dubé, L. Marmet, and R. S. Windeler, *Absolute frequency of the* $^{88}Sr^{+}$ $5s\,^2S_{1/2} \rightarrow 4d\,^2D_{5/2}$ *reference transition at* 445 THz *and evaluation of systematic shifts*, *Phys. Rev. A* **70** (Jul, 2004) 012507.

[166] J. Jin and D. A. Church, *Precision lifetimes for the* $^{40}Ca^{+}$ $4p^2P$ *levels, experiment challenges theory at the 1% level*, *Phys. Rev. Lett.* **70** (May, 1993) 3213–3216.

[167] A. Kreuter, C. Becher, G. P. T. Lancaster, A. B. Mundt, C. Russo, H. Häffner, C. Roos, W. Hänsel, F. Schmidt-Kaler, R. Blatt, and M. S. Safronova, *Experimental and theoretical study of the* $3d^2d$*-level lifetimes of* $^{40}Ca^{+}$, *PRA* **71** (Mar., 2005) 032504.

[168] C. Guet and W. R. Johnson, *Relativistic many-body calculations of transition rates for* Ca^{+}, Sr^{+}, *and* Ba^{+}, *Phys. Rev. A* **44** (Aug, 1991) 1531–1535.

[169] S. Mannervik, J. Lidberg, L.-O. Norlin, P. Royen, A. Schmitt, W. Shi, and X. Tordoir, *Lifetime measurement of the metastable* $4d^2D_{3/2}$ *level in* Sr^{+} *by optical pumping of a stored ion beam*, *Phys. Rev. Lett.* **83** (Jul, 1999) 698–701.

[170] K. J. Arnold, S. R. Chanu, R. Kaewuam, T. R. Tan, L. Yeo, Z. Zhang, M. S. Safronova, and M. D. Barrett, *Measurements of the branching ratios for* $6P_{1/2}$ *decays in* $^{138}Ba^{+}$, *PRA* **100** (Sept., 2019) 032503.

[171] N. Yu, W. Nagourney, and H. Dehmelt, *Radiative lifetime measurement of the* Ba^{+} *metastable* $D_{3/2}$ *state*, *Phys. Rev. Lett.* **78** (Jun, 1997) 4898–4901.

[172] S. Olmschenk, D. Hayes, D. N. Matsukevich, P. Maunz, D. L. Moehring, K. C. Younge, and C. Monroe, *Measurement of the lifetime of the* $6p\,^2P^o_{1/2}$ *level of* Yb^{+}, *PRA* **80** (Aug., 2009) 022502.

[173] C. Gerz, J. Roths, F. Vedel, and G. Werth, *Lifetime and collisional depopulation of the metastable* $5D_{3/2}$ *state of* Yb^{+}, *Zeitschrift für Physik D Atoms, Molecules and Clusters* **8** (1988), no. 3 235–237.

[174] J. Stenger, C. Tamm, N. Haverkamp, S. Weyers, and H. R. Telle, *Absolute frequency measurement of the 435.5-nm* $^{171}Yb^{+}$ *clock transition with a kerr-lens mode-locked femtosecond laser*, *Opt. Lett.* **26** (2001), no. 20 1589–1591.

[175] R. J. Rafac, B. C. Young, J. A. Beall, W. M. Itano, D. J. Wineland, and J. C. Bergquist, *Sub-dekahertz ultraviolet spectroscopy of* $^{199}Hg^{+}$, *Phys. Rev. Lett.* **85** (Sep, 2000) 2462–2465.

[176] M. R. Dietrich, N. Kurz, T. Noel, G. Shu, and B. B. Blinov, *Hyperfine and optical barium ion qubits*, *PRA* **81** (May, 2010) 052328.

[177] V. Letchumanan, P. Gill, E. Riis, and A. G. Sinclair, *Optical ramsey spectroscopy of a single trapped* $^{88}Sr^{+}$ *ion*, *PRA* **70** (Sept., 2004) 033419.

[178] A.-M. Mårtensson-Pendrill, D. S. Gough, and P. Hannaford, *Isotope shifts and hyperfine structure in the 369.4-nm resonance line of singly ionized ytterbium*, *PRA* **49** (May, 1994) 3351–3365.

[179] R. J. Hendricks, J. L. Sørensen, C. Champenois, M. Knoop, and M. Drewsen, *Doppler cooling of calcium ions using a dipole-forbidden transition*, *PRA* **77** (Feb., 2008) 021401.

[180] J. Guéna, M. Abgrall, D. Rovera, P. Rosenbusch, M. E. Tobar, P. Laurent, A. Clairon, and S. Bize, *Improved tests of local position invariance using* ^{87}Rb *and* ^{133}Cs *fountains*, *PRL* **109** (Aug., 2012) 080801.

[181] P. Delva, N. Puchades, E. Schönemann, F. Dilssner, C. Courde, S. Bertone, F. Gonzalez, A. Hees, C. Le Poncin-Lafitte, F. Meynadier, R. Prieto-Cerdeira, B. Sohet, J. Ventura-Traveset, and P. Wolf, *Gravitational redshift test using eccentric galileo satellites*, *PRL* **121** (Dec., 2018) 231101.

[182] S. Herrmann, F. Finke, M. Lülf, O. Kichakova, D. Puetzfeld, D. Knickmann, M. List, B. Rievers, G. Giorgi, C. Günther, H. Dittus, R. Prieto-Cerdeira, F. Dilssner, F. Gonzalez, E. Schönemann, J. Ventura-Traveset, and C. Lämmerzahl, *Test of the gravitational redshift with galileo satellites in an eccentric orbit*, *PRL* **121** (Dec., 2018) 231102.

[183] M. S. Safronova, *The search for variation of fundamental constants with clocks*, *ANNALEN DER PHYSIK* **531** (May, 2019) 1800364.

[184] T. H. Dinh, A. Dunning, V. A. Dzuba, and V. V. Flambaum, *Sensitivity of hyperfine structure to nuclear radius and quark mass variation*, *PRA* **79** (May, 2009) 054102.

[185] J. C. Berengut, V. V. Flambaum, and E. M. Kava, *Search for variation of fundamental constants and violations of fundamental symmetries using isotope comparisons*, *PRA* **84** (Oct., 2011) 042510.

[186] N. J. Stone, *Table of nuclear magnetic dipole and electric quadrupole moments*, *Atomic Data and Nuclear Data Tables* **90** (2005), no. 1 75–176.

[187] H.-R. Qin, S.-N. Miao, J.-Z. Han, N.-C. Xin, Y.-T. Chen, J. W. Zhang, and L. J. Wang, *High-performance microwave frequency standard based on sympathetically cooled ions*, 2022.

[188] S. Schiller, A. Görlitz, A. Nevsky, J. C. J. Koelemeij, A. Wicht, P. Gill, H. A. Klein, H. S. Margolis, G. Mileti, U. Sterr, F. Riehle, E. Peik, C. Tamm, W. Ertmer, E. Rasel, V. Klein, C. Salomon, G. M. Tino, P. Lemonde, R. Holzwarth, and T. W. Hänsch, *Optical clocks in space*, *Nuclear Physics B - Proceedings Supplements* **166** (Apr., 2007) 300–302.

[189] Collaboration, *Observation of gravitational waves from a binary black hole merger*, *PRL* **116** (Feb., 2016) 061102.

[190] Collaboration, *Gw170817: Observation of gravitational waves from a binary neutron star inspiral*, *Phys. Rev. Lett.* **119** (Oct., 2017) 161101.

[191] A. Vutha, *Optical frequency standards for gravitational wave detection using satellite doppler velocimetry*, *New Journal of Physics* **17** (2015), no. 6 063030.

[192] S. Kolkowitz, I. Pikovski, N. Langellier, M. D. Lukin, R. L. Walsworth, and J. Ye, *Gravitational wave detection with optical lattice atomic clocks*, *PRD* **94** (Dec., 2016) 124043.

[193] D. P. DiVincenzo, *The physical implementation of quantum computation*, *Fortschr. Phys.* **48** (Sept., 2000) 771–783.

[194] C. D. Bruzewicz, R. McConnell, J. Stuart, J. M. Sage, and J. Chiaverini, *Dual-species, multi-qubit logic primitives for* Ca^+/Sr^+ *trapped-ion crystals*, *npj Quantum Information* **5** (Nov., 2019) 102.

[195] J. E. Christensen, D. Hucul, W. C. Campbell, and E. R. Hudson, *High-fidelity manipulation of a qubit enabled by a manufactured nucleus*, *npj Quantum Information* **6** (2020), no. 1 35.